

ON THE EFFECTIVE PROPERTIES OF NEMATIC POLYMER
NANO-COMPOSITES

Xiaoyu Zheng

A dissertation submitted to the faculty of the University of North Carolina at Chapel Hill in partial fulfillment of the requirements for the degree of Doctor of Philosophy in the Department of Mathematics.

Chapel Hill
2006

Approved by:

Advisor: Professor M. Gregory Forest
Reader: Professor David Adalsteinsson
Reader: Professor Roberto Camassa
Reader: Professor Timothy C. Elston
Reader: Professor Jingfang Huang

© 2006
Xiaoyu Zheng
ALL RIGHTS RESERVED

ABSTRACT

XIAOYU ZHENG: On the Effective Properties of Nematic Polymer Nano-Composites

(Under the direction of Professor M. Gregory Forest)

Many nano-composites consist of rod-like or platelet macromolecules in a solvent matrix, which are observed to yield large property enhancements at very low volume fraction. These particle suspensions are called liquid crystal polymers because they order at a critical volume fraction. In this dissertation, we study the role of the orientational distribution function of liquid crystal polymers and high aspect ratio particle dispersions in composite properties. Chapter I provides a review of the kinetic theory of flowing rod dispersions. In Chapters II and III, we use homogenization theory to predict volume-averaged effective properties (specifically thermal conductivity and mechanical properties) versus particle volume fraction, aspect ratio and shear rate. The formulas we derive are in terms of second and fourth moments of the orientational distribution function of the inclusions. We close with recent progress on percolation in rod dispersions.

To my parents

ACKNOWLEDGEMENTS

I am deeply indebt to Dr. M. Gregory Forest, my advisor, for his guidance and consistent support through all my time at Chapel Hill. He has given me his time and expertise unselfishly. His dedication and encouragement have made this research a rewarding experience.

I would also like to express my gratitude to my committee members: Dr. Roberto Camassa, Dr. Tim Elston, Dr. Jingfang Huang, Dr. David Adalsteinsson, as well as to Dr. Robert Lipton at Louisianan State University and Dr. Qi Wang at Florida State University, for their help and valuable suggestions on my research. Their insightful feedback has greatly improved the quality of the dissertation. They have always been generous with their time and experience, and steered me to a much productive path that I might not have taken otherwise.

During my first couple of years at Chapel Hill, I had received generous help from people in NC. I cordially thank all of them. I also would like to extend my appreciation to our former postdoc Dr. Ruhai Zhou. I am very grateful for his help on my research. My special thanks go to the departmental staff: Brenda Beathea, Jean Foushee-Tyson, and Janet Farrell. Their assistance has made my study at UNC-Chapel Hill quite pleasant.

Finally, I would like to thank my parents, my big brother, and my boyfriend for their love, support, and understanding over the years, without whom this dissertation could not have been completed.

CONTENTS

LIST OF TABLES		ix
LIST OF FIGURES		x
1 Kinetic Theory and Mesoscopic Models for Nematic Fluids Monodomain		1
1.1 Introduction		1
1.2 Kinetic equation for the orientational distribution function		1
1.2.1 Dilute suspensions		2
1.2.2 Semi-dilute solutions		3
1.3 Stress tensor		5
1.4 Mesoscopic theory of orientational distribution function		6
1.5 Flow-phase diagrams of monodomain attractors		8
1.6 Likelihood and expected time statistics of monodomain attractors		15
1.6.1 Motivation		15
1.6.2 Parametrization of the experimental initial data set		16
1.6.3 Local and global measures of attractor “strength”		18
1.6.4 Domains of attraction in bi-stable and tri-stable regions		37
1.6.5 Conclusion		41
2 Effective Conductivity Properties of Nematic Polymer Nano-Composites		44
2.1 Introduction		44
2.2 Formulation of the nano-composite effective conductivity problem		46

2.2.1	Nano-composite microstructure	47
2.2.2	The effective conductivity tensor $\Sigma_{\theta_2}^e$ for isotropic ellipsoids	47
2.2.3	The effective conductivity tensor $\Sigma_{\theta_2}^e$ for anisotropic ellipsoids	48
2.2.4	The effective conductivity tensors $\Sigma_{\theta_2}^e$ for isotropic coated ellipsoids	49
2.3	Nano-composite properties of nematic polymer monodomains	50
2.4	Finer estimates for high contrast conductivity and extreme aspect ratio	53
2.5	Applications I: Effective conductivity tensors for quiescent and shear-induced mesophases	55
2.5.1	Dilute isotropic concentrations $f_0(\mathbf{m}) = \frac{1}{4\pi}$	55
2.5.2	Shear-induced monodomains at dilute concentrations	57
2.5.3	Quiescent nematic phases and mesoscopic approximations	61
2.5.4	Shear perturbed, flow-aligned monodomains at nematic concentrations	63
2.5.5	Illustrations	70
2.5.6	Conclusion	71
2.6	Applications II: Anisotropy and dynamic ranges in effective properties of sheared nematic polymer nano-composites	73
2.6.1	Conductivity enhancement of NPNCs at steady state	73
2.6.2	Dynamic and anisotropy of property enhancement for periodic attractors	77
2.6.3	Conclusion	83
3	Anisotropic Elastic Moduli of Quiescent and Sheared NPNCs	84
3.1	Introduction	84
3.1.1	Stress-strain relations	85
3.1.2	Stiffness tensor and elastic moduli	86
3.2	Effective stiffness tensors	90
3.2.1	Low volume fraction expansion vs. Mori-Tanaka theory	90
3.2.2	Eshelby tensor S	91
3.2.3	Tensor computations	92

3.2.4	Orientational averages	94
3.2.5	A hierarchy of symmetries of the effective elasticity tensor of nano-spheroid composites	95
3.3	Mechanical property predictions of rod nano-composites	97
3.3.1	Effective properties vs. volume fraction for quiescent mesophases	98
3.3.2	Effective moduli of sheared nano-rod composites	101
3.4	Conclusions	104
4	Future Work	106
4.1	Percolation-dominated properties	106
4.2	Elastic wave propagation through nano-composites	107
	BIBLIOGRAPHY	107

LIST OF TABLES

1.1	The set of stable bulk monodomain responses in the regions depicted in Figure 1.5.	14
1.2	Stable solutions of the Doi model versus Peclet number, for a fixed nematic concentration $N = 3.5$, and for a 1:3 discotic or 3:1 rod-like nematic polymer aspect ratio. On the left are in-plane confined dynamics, on the right is the full tensor result.	21
1.3	Stable solutions of the Doi tensor model versus Peclet number, for a fixed nematic concentration $N=6$, and for 1 : 3 discotic or 3 : 1 rod-like nematic polymer aspect ratio. The top row is for in-plane confined dynamics, Figure 1.3; the bottom two rows are the full tensor result, Figure 1.4.	27
1.4	Statistical distribution of attractors in the FA and LR bi-stable regime for $N = 4$ and three different Pe	38
1.5	Statistical distribution of attractors in the T/W and LR bi-stable regime, for $N = 6.66$ and five different Pe	38
1.6	Likelihood statistics for $N = 6, Pe = 2.3$, in the W and LR bi-stable regime, with different initial polar angles. The degree of out-of-plane tilt is seen to control the likelihood of W vs LR attractors.	39
1.7	Statistical distribution of bi-stable attractors for $N = 6$, with different Pe in the W and K₁ bi-stable regime.	40
1.8	Attractor likelihood distribution for $N = 6, Pe = 2.5$, which is in the K₁ and K₂^{+,−} tri-stable regime, with different initial polar angles.	41
1.9	Likelihood statistics for $N = 6$ and different Pe in the K₁ and K₂^{+,−} tri-stable regime .	41
2.1	Data for the range of typical aspect ratios r and electrical conductivity contrasts σ_1/σ_2 of rod-like nematic polymer nano-composites.	54
3.1	Properties of matrix and nano-rod inclusion (GPa)	98

LIST OF FIGURES

1.1	The parallel-plate shear cell with homogeneous plate anchoring conditions . . .	9
1.2	The diagram of flow, flow-gradient, and vorticity direction in cartesian coordinates.	9
1.3	The monolayer flow-phase diagram of the Doi closure model with constant rotary diffusivity, for confined <i>in-plane orientation tensors</i> and molecule aspect ratio $r = 3$ or $\frac{1}{3}$. The diagram depicts all stable monodomain states versus nematic concentration (N) and normalized shear rate (Pe). The bifurcation curves bound regions of fixed number and type of attracting states, corresponding to flow and concentration-induced phase transitions among confined in-plane attractors.	12
1.4	The full tensor flow-phase diagram of the Doi mesoscopic closure model, for aspect ratio $r = 3$ or $\frac{1}{3}$, constant rotary diffusivity, variable concentration (N) and normalized shear rate (Pe). The details of the “complex dynamics region” are discussed in Forest and Wang (2003), see also Rienacker and Hess (2002).	12
1.5	Kinetic monodomain flow phase diagram versus concentration N and Peclet number Pe , for aspect ratio $a = 1$. Forest <i>et al.</i> (2004b))	13
1.6	Order parameter versus concentration. The solid line is stable equilibrium, the dashed lines are unstable solution. There is a first order transition, which is discontinuous, hysteresis. The bistable region is between $N = 8/3$ and $N = 3$. .	17
1.7	In-plane statistics versus that of the full tensor space for the expected time to converge to FA , with nematic concentration $N = 3.5$, aspect ratio $r = \frac{1}{3}$ and distance function $D_2 < 10^{-3}$. Left: Local measure; right: Global measure.	22
1.8	Sample orbits to FA attractors for $Pe = 1$ (top row) and $Pe = 10$ (bottom row). Column 1: the components of Q vs time. Column 2: path of the major director for discotic nematic polymers from initial condition $\phi_0 = 93.6^\circ, \theta_0 = 45^\circ$. Column 3: path of the major director for rod-like nematic polymers from initial condition $\phi_0 = 3.6^\circ, \theta_0 = 45^\circ$. The concentration $N = 3.5$, which is in the quiescent nematic range, but below the tumbling transition at onset of shear.	23
1.9	First and second normal stress differences N_1, N_2 (left axis scale), and apparent viscosity η (right axis scale) versus time, in transient approach to FA attractor of Table 1.2, with $N = 3.5, a = 0.8$. Top row is for $Pe = 1$, bottom row is for $Pe = 10$. In each case, the initial director is tilted out-of-plane with polar coordinates $\phi_0 = 3.6^\circ, \theta_0 = 45^\circ$	25
1.10	Mesoscopic predictions for the start-up of shear flow of the relative Leslie alignment angle Φ with $\phi_0 = 3.6^\circ, \phi_L = 7.91$, and initial out-of-plane tilt angles $\theta_0 = 9^\circ, 45^\circ, 81^\circ$, respectively. $Pe = 1, N = 3.5, a = 0.8$	26

1.11	In-plane statistics versus that of the full tensor space for the expected time to converge to FA , fixed nematic concentration $N = 6$, aspect ratio $a = -0.8$ and distance function $D_2 < 10^{-3}$. Left: local measure; Right: global measure.	28
1.12	Sample paths for FA attractors in the high concentration ($N = 6$), strong shear ($Pe = 4, 10$) regime. Column 1: the components of Q vs time. Column 2: path of the major director for discotic nematic polymers from initial condition $\phi_0 = 93.6^\circ$, $\theta_0 = 45^\circ$. Column 3: path of the major director for rod-like nematic polymers from initial condition $\phi_0 = 3.6^\circ$, $\theta_0 = 45^\circ$. Top row $Pe = 4$; bottom row $Pe = 10$	29
1.13	In-plane statistics for the expected time to converge to T/W attractors of Table 1.3, for confined in-plane dynamics, with nematic concentration $N = 6$	30
1.14	First normal stress difference N_1 (left), apparent viscosity η (right) versus time, for a randomly chosen orbit converging to a T attractor of Table 1.3, with Peclet number $Pe = 1, N = 6$. The averages over one period are $\langle N_1 \rangle \approx 1.5 \times 10^{-2}$, $\langle N_2 \rangle \approx -10^{-3}$, $\langle \eta \rangle \approx 7 \times 10^{-2}$, with large deviations by factors of 10 for N_1 and 2 for η	31
1.15	Full tensor model statistics for the expected time to converge to the K₁ attractor of Table 1.3, with $N = 6$	32
1.16	Comparison of the limit cycle periods for W & K₁	33
1.17	First normal stress difference N_1 (top left), apparent viscosity η (top right) versus time, for a randomly chosen orbit that converges to the W attractor of Table 1.3, with Peclet number $Pe = 2.3$, nematic concentration $N = 6$, rodlike aspect ratio $r = 3$ ($a = 0.8$). $\langle N_1 \rangle \approx -1.1 \times 10^{-1}$, $\langle N_2 \rangle \approx 3.5 \times 10^{-2}$ (not shown), $\langle \eta \rangle \approx 4 \times 10^{-2}$ over the period of W , with strong fluctuations by factors of 3 for N_1 and 3 for η . The corresponding order parameter and in-plane director dynamics are shown bottom left and right. For discotic aspect ratio $r = \frac{1}{3}$ ($a = -0.8$) with all other parameters held constant, $\langle N_1 \rangle$ and $\langle \eta \rangle$ are nearly identical, while $\langle N_2 \rangle$ increases by a factor of about 2.	35
1.18	First normal stress difference N_1 (top left), apparent viscosity η (top right) versus time, for a randomly chosen orbit that converges to the K₁ attractor of Table 1.3, with Peclet number $Pe = 2.3$, nematic concentration $N = 6$, rodlike aspect ratio $r = 3$ ($a = 0.8$). $\langle N_1 \rangle \approx 4 \times 10^{-2}$, $\langle N_2 \rangle \approx -3 \times 10^{-2}$ (not shown), $\langle \eta \rangle \approx 5 \times 10^{-2}$ over the period of K₁ , with strong fluctuations by factors of 5 for N_1 and 2 for η . For discotic aspect ratio $r = \frac{1}{3}$ ($a = -0.8$), $\langle N_1 \rangle$ and $\langle \eta \rangle$ are nearly the same, while $\langle N_2 \rangle$ decreases by a factor of 10.	36
1.19	Statistics of the likelihood of convergence to attractors from the nematic rest state at a fixed concentration $N = 6$, for the K₁ and W bi-stable region with $Pe = 2.3$. The lighter points represent initial director configuration that will converge to K₁ , whereas the black points converge to W	39

1.20	First normal stress difference N_1 (top), apparent viscosity η (bottom) versus time, averaged over 1000 sample orbits in the bi-stable region of Table 1.3, with Peclet number $Pe = 2.3$, nematic concentration $N = 6$, rodlike aspect ratio $r = 3$ ($a = 0.8$). $\langle N_1 \rangle \approx -7 \times 10^{-3}$, $\langle N_2 \rangle \approx 1.5 \times 10^{-2}$ (not shown), $\langle \eta \rangle \approx 5 \times 10^{-2}$, with strong fluctuations by factors of 6 for N_1 and 1.3 for η . The results for platelets ($a = -0.8$) are nearly identical for $\langle N_1 \rangle$ and $\langle \eta \rangle$, whereas $\langle N_2 \rangle$ is nearly zero, but negative.	42
1.21	Statistics in tri-stable ($\mathbf{K}_1, \mathbf{K}_2^{+, -}$) region with $Pe=2.5$. The lighter gray points on the sphere are the initial director orientations that converge to \mathbf{K}_1 , the black points converge to $\mathbf{K}_2^{+, -}$	43
1.22	Statistics in $\mathbf{K}_2^{+, -}$ bi-stable region with $Pe=3.5$. The light gray points are the initial director orientations that converge to \mathbf{K}_2^+ , the black points converge to \mathbf{K}_2^- . Note this view is looking down from the vorticity axis at the center.	43
2.1	The illustration of spheroidal rods with semi-axes lengths $a > b = c$, with respect to axes \mathbf{m} , \mathbf{n} , \mathbf{k} , respectively.	47
2.2	Depolarization factor L_a versus aspect ratio r	51
2.3	The scaling factor $\chi(a, \theta_2)$ vs. θ_2 , for $r = 100$	65
2.4	Quiescent orientation-conductivity enhancement correlations versus volume fraction for two model nano-composites. Hysteresis associated with the quiescent I-N phase transition is duplicated in the effective conductivity property enhancement for two model systems. Left column: Order parameter S versus volume fraction θ_2 . Right column: Corresponding relative conductivity enhancement \mathcal{E}_{max} . Model system aspect ratio and conductivity contrasts are given for each row. The two vertical lines mark the critical concentration, θ_2^* and θ_2^{**} , of each model system; θ_2^* is the onset of the nematic phase, while θ_2^{**} is the instability transition of the isotropic phase.	67
2.5	Comparison between shear-induced and quiescent orientation order parameter versus volume fraction, and the corresponding effective conductivity enhancements for the two model systems of Figure 2.4. Left column: Order parameter S versus volume fraction θ_2 (dark color is for $Pe=0$, light color is for weak shear rate $Pe = 0.1$). Right column: Corresponding relative conductivity enhancements.	68
2.6	Left column: The flow-induced contribution to \mathcal{E}_{max} , defined by $\mathcal{E}_{max} - \mathcal{E}_{max}^{Pe=0}$, where $\mathcal{E}_{max}^{Pe=0}$ depends on the volume fraction (Figure 2.4). In the bistable region, we show the flow contribution for both stable phases at $Pe = 0$. Right column: The fraction of the total enhancement, \mathcal{E}_{max} , contributed by the flow-induced values \mathcal{E}_{Pe}^{iso} , \mathcal{E}_{Pe}^{nema} , respectively.	69

2.7	Peak alignment angle (figure a) and maximum scalar conductivity enhancement (b,c) for families of flow-aligned steady states at normalized concentrations for $N = 4.7, 5.5, 6$, respectively, volume fractions $\theta_2 = 0.92\%, 1.08\%, 1.26\%$ corresponding to $r = 200$ (figure b) and $\theta_2 = 3.69\%, 4.32\%, 5.03\%$ for $r = 50$ (figure c). These states exist and are stable over the indicated ranges of normalized shear rate (Pe).	75
2.8	Maximum scalar conductivity enhancements for steady logrolling states at concentrations $N = 5.5, 5.75, 6$, respectively, volume fractions $\theta_2 = 1.08\%, 1.13\%, 1.18\%$ with aspect ratio $r = 200$ over the range of normalized shear rates (Pe) where these states are stable.	76
2.9	Dynamic ranges at low volume fraction $\theta_2 = 1.08\%$ ($N = 5.5, r = 200$) of the peak alignment direction for tumbling (top left, $Pe = 3.4$) and wagging (top right, $Pe = 4$) sheared monodomains; and (bottom) corresponding <i>maximum scalar effective conductivity enhancement</i> \mathcal{E} , and <i>effective conductivity anisotropy measure</i> $\mathcal{E}_1 - \mathcal{E}_2$, where tumbling values are solid and wagging values are dotted.	78
2.10	(Left) Dynamics of the peak orientation of the PDF around the vorticity axis (the dot in the middle), and (right) the dynamic ranges of \mathcal{E}_1 and $\mathcal{E}_1 - \mathcal{E}_2$, for a typical kayaking limit cycle (K_1) at normalized shear rate $Pe = 3$, and normalized rod concentration $N = 5.2$, achieved for volume fraction $\theta_2 = 1.02\%$ with $r = 200$	79
2.11	(Left) Dynamics of the peak orientation axis of the PDF around the vorticity axis (the dot in the middle), and (right) the dynamic ranges of \mathcal{E}_1 and $\mathcal{E}_1 - \mathcal{E}_2$ for a typical tilted kayaking state (K_2) at higher shear rate $Pe = 6$, normalized concentration $N = 5.5$, achieved by volume fraction $\theta_2 = 1.08\%$ with nano-rod aspect ratio $r = 200$	80
2.12	(Left) Chaotic orbit of the peak orientation axis of PDF at moderate shear rate $Pe = 4.044$ and normalized concentration $N = 5.2$ ($\theta_2 = 1.02\%$ for $r = 200$). (Right) The dynamics ranges of \mathcal{E}_1 and $\mathcal{E}_1 - \mathcal{E}_2$ for the chaotic monodomain PDF attractor on the left.	81
2.13	“Property bifurcation diagram” of maximum conductivity enhancement \mathcal{E}_{max} versus normalized shear rate Pe at fixed normalized concentration $N = 5.5$, achieved by $\theta_2 = 1.02\%$ for $r = 200$. The vertical axis is the time-averaged, maximum principal value, \mathcal{E}_{max} , of the effective conductivity tensor Σ^e , for each stable (solid curves) and unstable (dashed) sheared monodomain response over this entire range of shear rates (Pe).	82
3.1	a. Order parameter s vs. volume fraction θ_2 ; b. corresponding relative enhancement of Young’s moduli E^e ; c. corresponding relative enhancement of shear moduli G^e ; d. Corresponding relative enhancement of transverse bulk moduli k_T^e . The solid lines are the relative longitudinal moduli, the dashed lines are the relative transverse moduli.	99

3.2	Sheared PDFs and effective moduli for 1% volume fraction nano-rods of aspect ratio 100, with particle-matrix properties of Table 3.1 (Odegard <i>et al.</i> (2003)). a. Eigenvalues ($d_1 > d_2 > d_3$) of \mathbf{M}_2 vs. normalized shear rate (Peclet number Pe); b. corresponding relative enhancement of Young's moduli; c. corresponding relative enhancement of shear moduli.	102
3.3	Sheared PDFs and effective moduli for 2.3% volume fraction nano-rods of aspect ratio 100, arising from vorticity-aligned (logrolling) steady states. a. eigenvalues ($d_1 > d_2 > d_3$) of \mathbf{M}_2 vs. normalized shear rate (Peclet number Pe); b. relative enhancement of Young's moduli; c. relative enhancement of shear moduli. . .	104

Chapter 1

Kinetic Theory and Mesoscopic Models for Nematic Fluids Monodomain

1.1 Introduction

The rheological properties of solutions of a rodlike or platelet polymer change dramatically with concentration. At very low concentration, the solution is nearly a Newtonian fluid with weak elastic properties. As the concentration increases, the viscosity increases rapidly, and there appears marked nonlinear viscoelasticity. With further increase in concentration, the solution transitions to a liquid-crystalline phase, and its rheological properties become even more complicated.

The macromolecules or particles we consider are rigid spheroids with length L and diameter d , with $L/d \gg 1$ for rods and $L/d \ll 1$ for platelets. As Onsager and Flory showed, a solution of such molecule forms liquid crystals of nematic structure above a certain critical concentration $c^* \approx 1/dL^2$, where c^* denotes the number of rods per unit volume.

Through out this dissertation, we only consider the orientational space of the molecule, without physical spatial distortions, on micron scales which correspond to homogeneous phases, so-called monodomains.

1.2 Kinetic equation for the orientational distribution function

Let \mathbf{m} denote a unit vector parallel to the symmetry axis of such a molecule, and $f(\mathbf{m}, t)$ its distribution function.

1.2.1 Dilute suspensions

First, consider dilute concentrations, $c \ll 1/L^3$, the rotational motion of the rods is independent and is described by the theory of Kirkwood and Auer (1951), neglecting translational diffusion:

$$\frac{\partial f}{\partial t} = D_r^0 \frac{\partial^2 f}{\partial \mathbf{m}^2} - \frac{\partial}{\partial \mathbf{m}} \cdot \dot{\mathbf{m}} f, \quad (1.1)$$

where $\frac{\partial}{\partial \mathbf{m}}$ is the gradient operator on the sphere $\mathbf{m} \in S^2$. Here $\dot{\mathbf{m}}$ is the rate of change of \mathbf{m} due to the macroscopic flow, known as a Jeffery orbit:

$$\dot{\mathbf{m}} = \Omega \cdot \mathbf{m} + a(\mathbf{m} \cdot \mathbf{D} - \mathbf{m}\mathbf{m} : \mathbf{D}), \quad (1.2)$$

\mathbf{D} and Ω are the rate of strain and vorticity tensors, defined by

$$\mathbf{D} = \frac{1}{2}(\nabla \mathbf{v} + \nabla \mathbf{v}^T), \quad \Omega = \frac{1}{2}(\nabla \mathbf{v} - \nabla \mathbf{v}^T), \quad (1.3)$$

and $-1 \leq a \leq 1$ is the molecular shape parameter related to the molecular aspect ratio $r = L/d$ by

$$a = \frac{r^2 - 1}{r^2 + 1}. \quad (1.4)$$

Note that $a \approx 1$ corresponds to a thin rod limit; $a = 0$ corresponds to spherical molecules; and $a \approx -1$ corresponds to the thin disk limit.

D_r^0 is the dilute-solution rotational diffusivity, that is, the rate at which a particle reorients by Brownian motion.

For a particle of nearly spherical shape and diameter d , we have

$$D_r^0 = \frac{kT}{\pi \eta_s d^3}, \quad (1.5)$$

where k is the Boltzmann constant and T is the absolute temperature.

For a circular disk-like particle of diameter d , we get

$$D_r^0 = \frac{3kT}{4\eta_s d^3}, \quad (1.6)$$

For rods of length L , diameter d , D_r^0 becomes

$$D_r^0 = \frac{3kT(\ln(L/d) - 0.8)}{\pi\eta_s L^3}, \quad (1.7)$$

(η_s being the solvent viscosity).

The crossover from Brownian to non-Brownian behavior in a flowing suspension is controlled by a rotatory Peclet number

$$Pe \equiv \frac{\dot{\gamma}}{D_r^0}. \quad (1.8)$$

Since typical shear rate are in the range $10^{-3} \leq \dot{\gamma} \leq 10^3 \text{ sec}^{-1}$, and $D_r^0 \sim 1/L^3$ for rod, thus if the aspect ratio of the particle exceeds 10, and the largest dimension is greater than a micron, the particle is usually non-Brownian.

1.2.2 Semi-dilute solutions

With increasing concentration $c \gg 1/L^3$, the rod begin to collide, the rotational motion of an individual rod becomes severely restricted by the surrounding rods. Consequently, the rotational diffusion constant becomes very small. Each rod is confined within a tubelike region of radius a , which depends on the distance between the test rod and its neighbors:

$$a(\mathbf{m}, f(\mathbf{m}, t)) \approx (cL^2 \int d^2\mathbf{m}' f(\mathbf{m}'; t) \sin(\mathbf{m}, \mathbf{m}'))^{-1}, \quad (1.9)$$

where $(\mathbf{m}, \mathbf{m}')$ denotes the angle between \mathbf{m} and \mathbf{m}' , and $d^2\mathbf{m}$ means the integral over the surface of the sphere $|\mathbf{m}| = 1$. And its rotational diffusivity becomes

$$D_r(\mathbf{m}) = \nu_1 D_r^0 (cL^3)^{-2} \left(\frac{4}{\pi} \int d^2\mathbf{m}' f(\mathbf{m}'; t) \sin(\mathbf{m}, \mathbf{m}') \right)^{-1}. \quad (1.10)$$

Hence the kinetic theory now becomes

$$\frac{\partial f}{\partial t} = \nabla_{\mathbf{m}} \cdot D_r(\mathbf{m}) \nabla_{\mathbf{m}} f + \frac{\partial}{\partial \mathbf{m}} \cdot \dot{\mathbf{m}} f. \quad (1.11)$$

However, this equation is only valid for the low concentration region for $1/L^3 \ll c \ll 1/dL^2$. It can't describe the nematic phase since the only solution in equilibrium is the isotropic solution, $f = 1/4\pi$.

To generalize the above equation, we need to consider the free energy per unit volume of the solution (Doi (1975) and Doi and Edwards (1978)):

$$\mathcal{A} = ckT \left(\int d^2\mathbf{m} f(\mathbf{m}) \ln f(\mathbf{m}) + cdL^2 \int d^2\mathbf{m} d^2\mathbf{m}' f(\mathbf{m}) f(\mathbf{m}') \sin(\mathbf{m}, \mathbf{m}') \right). \quad (1.12)$$

The equilibrium distribution function $f(\mathbf{m})$ is determined by the condition that \mathcal{A} should be a minimum for all variations of f , i.e., $\frac{\delta \mathcal{A}}{\delta f} = 0$, the distribution function $f(\mathbf{m})$ is related to the potential by Boltzmann's equation:

$$f(\mathbf{m}) = C \exp(-V(\mathbf{m})/kT), \quad (1.13)$$

where

$$V(\mathbf{m}) = 2cdL^2kT \int d^2\mathbf{m}' f(\mathbf{m}') \sin(\mathbf{m}, \mathbf{m}') \quad (1.14)$$

is the mean-field potential by Onsager, which is supposed to act on the test rod by the surrounding rods, where C is a normalized constant, $C^{-1} = \int \exp(-V(\mathbf{m})/kT)$. The self-consistent equations (1.13)-(1.14) describe the isotropic-nematic phase transition.

To simplify the analysis, a more convenient form for the mean field potential is considered, which may more appropriate for thermotropic nematics, known as Maier-Saupe potential:

$$V_{MS}(\mathbf{m}) = -\frac{3}{2}NkT \mathbf{m} \mathbf{m} : \langle \mathbf{m} \mathbf{m} \rangle. \quad (1.15)$$

Maier-Saupe potential is got by expanding $\sin(\mathbf{m}, \mathbf{m}')$ in terms of irreducible tensors equivalent to spherical harmonics, as

$$\sin(\mathbf{m}, \mathbf{m}') = \frac{\pi}{4} \left[1 - \frac{15}{16} \left(m_i m_j - \frac{\delta_{ij}}{3} \right) \left(m'_i m'_j - \frac{\delta_{ij}}{3} \right) + \left(\begin{array}{c} \text{products of fourth-rank} \\ \text{irreducible tensors} \end{array} \right) + \dots \right], \quad (1.16)$$

(Through the dissertation, summation is implied over the repeated indices) substitute (1.16) in

equation (1.14) and ignore the higher order tensors and drop the first term, which is irrelevant for the orientational ordering.

In (1.15), $N = 2cdL^2$ is a dimensionless parameter proportional to concentration for prolate. It relates the volume fraction θ by $\theta = \frac{N\pi d}{8L}$. While for oblate particles or disks of high aspect ratio, N is redefined as $4\pi cd^3$, where d is the disk diameter.

Now in the process of Brownian motion, the test rod will feel the same potential $V(\mathbf{m})$. Therefore, the generalized Smoluchowski equation of Doi-Hess kinetic equation which can describe the dynamics of rodlike polymers in the region $c \geq 1/L^3$ is:

$$\frac{\partial f}{\partial t} = \nabla_{\mathbf{m}} \cdot D_r(\mathbf{m}) \left(\nabla_{\mathbf{m}} f + \frac{f}{kT} \nabla_{\mathbf{m}} V(\mathbf{m}) \right) + \frac{\partial}{\partial \mathbf{m}} \cdot \dot{\mathbf{m}} f. \quad (1.17)$$

In the dilute concentration $1/L^3 \ll c \ll 1/dL^2$, it reduces to (1.1).

If an external magnetic field presents, an extra potential V_H has to be added to the equation (1.17).

1.3 Stress tensor

For monitoring the first and second normal stress differences and shear stress, we record the homogeneous stress tensor (apart from an isotropic pressure) (Forest and Wang (2003)): The stress tensor contains an elastic term from Brownian motion and excluded volume: Doi (1981)

$$\tau^e = 3ackT[\mathbf{Q} - N(\mathbf{Q} + I/3)\mathbf{Q} + N\mathbf{Q} : \langle \mathbf{m m m m} \rangle]. \quad (1.18)$$

The viscous stress has been given by Hinch and Leal (1973):

$$\tau^v = 3ckT[\zeta_1(a)(\mathbf{D}\mathbf{M} + \mathbf{M}\mathbf{D}) + \zeta_2(a)\mathbf{D} : \langle \mathbf{m m m m} \rangle + \zeta_3(a)\mathbf{D}]. \quad (1.19)$$

The viscous stress arises from drag produced by the solvent as it flows past the ellipsoid. It goes to zero immediately when flow ceases, while the elastic, or Brownian, term relaxes gradually, as flow-induced orientation disappears by Brownian motion. The total stress is the sum of the

elastic and viscous contributions, as well as that from the Newtonian solvent, $\tau^s = 2\eta\mathbf{D}$.

$$\tau = \tau^e + \tau^v + \tau^s, \quad (1.20)$$

where η is the solvent viscosity, $\zeta_{1,2,3}$ are three shape-dependent friction coefficients:

$$\begin{aligned} \zeta_3 &= \frac{\zeta^{(0)}}{I_1}, \quad \zeta_1 = \zeta^{(0)}\left(\frac{1}{I_3} - \frac{1}{I_1}\right), \quad \zeta_2 = \zeta^{(0)}\left[\frac{J_1}{I_1 J_3} + \frac{1}{I_1} - \frac{2}{I_3}\right], \\ I_1 &= 2r \int_0^\infty \frac{dx}{\sqrt{(r^2+x)}(1+x)^3}, \quad I_3 = r(r^2+1) \int_0^\infty \frac{dx}{\sqrt{(r^2+x)^3}(1+x)^2}, \\ J_1 &= r \int_0^\infty \frac{xdx}{\sqrt{(r^2+x)}(1+x)^3}, \quad J_3 = r \int_0^\infty \frac{xdx}{\sqrt{(r^2+x)^3}(1+x)^2} \end{aligned} \quad (1.21)$$

We remark that although the dynamics and stability properties of \mathbf{Q} are trivially related by a rotation of axes for rods ($a > 0$) vs. platelets ($a < 0$), the stresses are strongly dependent on the sign of a and the differences in friction coefficients.

1.4 Mesoscopic theory of orientational distribution function

Equations (1.17) and (1.20) can be regarded as a rheological constitutive equation. However numerical analysis for such an equations are complicated. In order to advance the discussion in feasible form, some mathematics approximations is needed. Our goal is to derive a closed equation for the order parameter tensor $\mathbf{Q} = \mathbf{M} - \mathbf{I}/3$. A dynamics equation for the orientation tensor \mathbf{Q} is derived by taking the second moment of \mathbf{m} with respect to the pdf f , then using the kinetic equation (1.17) and Jeffery molecule dynamics (1.2):

$$\begin{aligned} \frac{D\mathbf{Q}}{Dt} &= \Omega \cdot \mathbf{Q} - \mathbf{Q} \cdot \Omega + a[\mathbf{D} \cdot \mathbf{Q} + \mathbf{Q} \cdot \mathbf{D}] + \frac{2a}{3}\mathbf{D} - 2a\mathbf{D} : \langle \mathbf{m}\mathbf{m}\mathbf{m}\mathbf{m} \rangle \\ &\quad - 6\tilde{D}_r^0[\mathbf{Q} - N(\mathbf{Q} + \frac{\mathbf{I}}{3}) \cdot \mathbf{Q} + N\mathbf{Q} : \langle \mathbf{m}\mathbf{m}\mathbf{m}\mathbf{m} \rangle], \end{aligned} \quad (1.22)$$

where \tilde{D}_r^0 is a constant averaged rotary diffusivity that results from the averaging process.

$$\mathbf{M} = \langle \mathbf{m}\mathbf{m} \rangle = \int \mathbf{m} \times \mathbf{m} f(\mathbf{m}) d\mathbf{m} \quad (1.23)$$

is the second moment of PDF, which is symmetric second order tensor, with trace 1. \mathbf{Q} is the traceless part of \mathbf{M} . \mathbf{M} and \mathbf{Q} share an orthonormal frame of eigenvectors, called the directors or optical axes, with corresponding eigenvalues $d_i, i = 1, 2, 3$ of \mathbf{M} or $d_i - 1/3$ of \mathbf{Q} , called the order parameters ordered by $0 \leq d_3 \leq d_2 \leq d_1 \leq 1$ where

$$\begin{aligned} d_1 + d_2 + d_3 &= 1, \\ \mathbf{Q} &= \sum (d_i - 1/3) \mathbf{n}_i \mathbf{n}_i. \end{aligned} \tag{1.24}$$

Each d_i conveys the degree to which the mesoscale ensemble of molecules \mathbf{m} is aligned with respect to the primary direction \mathbf{n}_i . Geometrically \mathbf{M} or \mathbf{Q} uniquely defines an orientational ellipsoid whose semi-axes are prescribed by the directors \mathbf{n}_i and whose axis lengths are the respective degrees of orientation d_i . The maximum normalized birefringence is the maximum of $|d_i - d_j|$, occurring in the plane of $\mathbf{n}_i, \mathbf{n}_j$.

The nematic is: biaxial if d_i are distinct; uniaxial if $d_1 > d_2 = d_3$, in which case the director \mathbf{n}_1 is “the” director; the major director is defined as \mathbf{n}_k for which d_k is the unique maximum. Otherwise, if $d_1 = d_2$, such \mathbf{Q} tensors are labelled as defects, corresponding to orientation states for which the peak orientation direction is degenerate. If $d_1 = d_2 \neq d_3$, then the eigenspace of the major director is the unit circle in the plane orthogonal to \mathbf{n}_3 , isotropic if all $d_i = \frac{1}{3}$, i.e. $\mathbf{Q} = 0$. By comparison, the Leslie-Eriksen continuum theory

$$0 = \mathbf{n} \times \left[\gamma \left(\frac{d\mathbf{n}}{dt} + \boldsymbol{\Omega} \cdot \mathbf{n} \right) + \gamma_2 \mathbf{D} \cdot \mathbf{n} \right] \tag{1.25}$$

corresponds to two restrictions on the tensor \mathbf{Q} ; uniaxiality and the molecule axis is identical with the director. These translate to fixing the d_j at values 1, 0, 0 which removes two degrees of freedom, and losing one director degree of freedom in the isotropic plane transverse to the director.

The presence of fourth-order tensor and the extra stress couples the second-moment evolution equation to fourth moments, requiring one either continue to generate higher moment equations and truncate at some finite order. Many authors have introduced closure approximations, and a general conclusion on the choice of closure would be there is no clear best

closure for all flows and flow rates. For example, the quadratic Doi closure

$$(\cdot) : \langle \mathbf{m m m m} \rangle = (\cdot) : \mathbf{M M} \quad (1.26)$$

gives reasonable predictions in strong flows.

1.5 Flow-phase diagrams of monodomain attractors

We recall and extend results of Forest and Wang (2003) for the particular mesoscopic tensor model that derives from the Doi kinetic theory with quadratic closure. We begin with the solution space of this model, i.e., the flow-phase diagrams of monodomain attractors versus 2 dimensionless parameters: a concentration parameter N , which controls the strength of the excluded volume potential; the Peclet number $Pe = \frac{\dot{\gamma}}{6D_r^0}$, where $\dot{\gamma}$ is the imposed shear rate and $6D_r^0$ is the average rotational relaxation rate. The remaining model parameter is a molecule aspect ratio parameter a . We choose a 3 : 1 or 1 : 3 aspect ratio ($r = 3, \frac{1}{3}$) of spheroidal molecules, for which $a = \pm 0.8$, since the resulting dynamical system qualitatively captures representative features of the kinetic phase diagram (Faraoni *et al.* (1999), Forest *et al.* (2003), Forest *et al.* (2004a) Forest *et al.* (2004b), and Grosso *et al.* (2001)). Mesoscopic models of Beris and Edwards (1994) and Rienacker and Hess (1999) share a similar phase diagram.

The kinetic and mesoscopic equations have a symmetry which implies monodomain responses of rods and platelets are equivalent up to a pure rotation of the pdf or the \mathbf{Q} tensor (Forest *et al.* (2002b), Forest and Wang (2003)). Therefore, results presented here for monodomain responses to pure shear may be applied to rod-like or discotic nematic polymers. Although the second-moment tensors of rod-like and discotic liquids are simply related, their stresses are not; we illustrate the difference below.

These tensor models are equivalent to a 5-dimensional ordinary differential equation (ODE) for the components

$$\vec{Q} = (Q_{xx}, Q_{xy}, Q_{yy}, Q_{xz}, Q_{yz}) \quad (1.27)$$

of the symmetric, trace zero, second-moment tensor \mathbf{Q} . All closures of the Doi kinetic theory

for monodomain response to imposed linear flow take the form (Forest and Wang (2003)):

$$\dot{\mathbf{Q}} = \mathbf{F}(\mathbf{Q}; N, a) + Pe \mathbf{G}(\mathbf{Q}; \nabla \mathbf{v}; a), \quad (1.28)$$

where time is normalized by the nematic timescale $(6D_r^0)^{-1}$, and Pe and N are defined earlier, and for pure shear flow in dimensional coordinates,

$$\mathbf{v}_{shear} = \dot{\gamma}(y, 0, 0), \quad \nabla \mathbf{v} = \Omega + D = \dot{\gamma} \begin{pmatrix} 0 & 1 & 0 \\ 0 & 0 & 0 \\ 0 & 0 & 0 \end{pmatrix}. \quad (1.29)$$

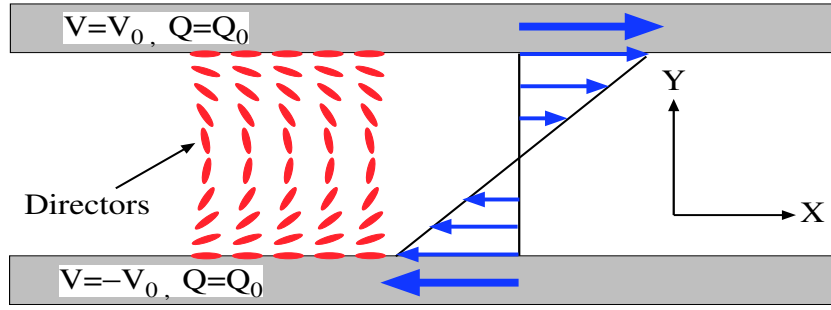


Figure 1.1: The parallel-plate shear cell with homogeneous plate anchoring conditions

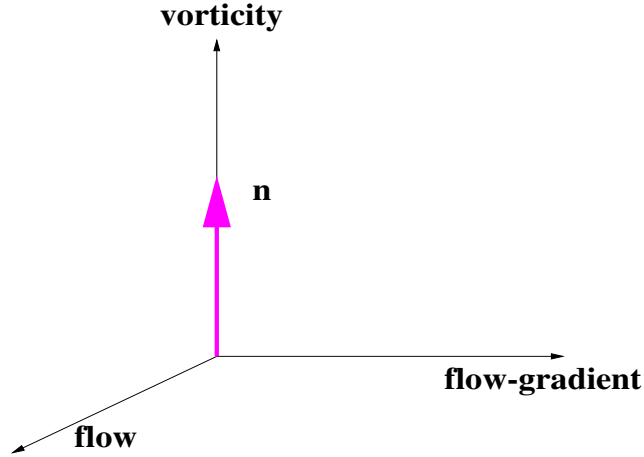


Figure 1.2: The diagram of flow, flow-gradient, and vorticity direction in cartesian coordinates.

The precise form of \mathbf{F}, \mathbf{G} for the Doi closure model are (Forest and Wang (2003)):

$$\begin{aligned}\mathbf{F} &= \mathbf{Q} - N(\mathbf{Q} + \frac{\mathbf{I}}{3}) \cdot \mathbf{Q} + N\mathbf{Q} : (\mathbf{Q} + \frac{\mathbf{I}}{3})(\mathbf{Q} + \frac{\mathbf{I}}{3}), \\ \mathbf{G} &= \boldsymbol{\Omega} \cdot \mathbf{Q} - \mathbf{Q} \cdot \boldsymbol{\Omega} + a(\mathbf{D} \cdot \mathbf{Q} + \mathbf{Q} \cdot \mathbf{D}) + (\frac{2a}{3}\mathbf{D} - 2a\mathbf{D} : (\mathbf{Q} + \frac{\mathbf{I}}{3})(\mathbf{Q} + \frac{\mathbf{I}}{3})).\end{aligned}\tag{1.30}$$

Physically, \mathbf{F} captures the mesoscopic approximation of the Maier-Saupe intermolecular potential, while \mathbf{G} represents the flow-induced orientational response for linear velocity fields.

By a combination of theory and experiment, many steady and transient shear-induced, monodomain modes have been catalogued and named primarily *on the basis of director response*: steady alignment with primary director either in the shear plane (flow aligning (**FA**)) or along the vorticity axis (logrolling (**LR**)); in-plane transient oscillatory (wagging (**W**)) or rotating (tumbling (**T**)) director modes; and out-of-plane transient director modes (kayaking (**K**)). Complicated dynamics is also possible.

In-plane and logrolling states fall into a special subspace of orientation tensors in planar shear flow, called **in-plane tensors** by a slight abuse of terminology, for which one direction is fixed parallel to the vorticity axis. Since \mathbf{Q} is symmetric, the remaining orthogonal eigenvectors lie in the flow deformation plane (x, y) , which we call the shear plane.

The space of in-plane (i-p) symmetric, traceless tensors, \mathbf{Q}^{i-p} , is 3-dimensional, obeying two constraints,

$$Q_{xz} = Q_{yz} = 0.$$

All mesoscopic tensor models in simple shear preserve \mathbf{Q}^{i-p} as a 3-dimensional invariant subspace, so the orientation dynamics can be studied distilled from the two out-of-plane degrees of freedom. By extension of the analysis and computations in Forest and Wang (2003) and Forest *et al.* (2003), from the fixed nematic concentration $N = 6$ to *all* N , we construct the flow-phase diagram of all attractors and phase-transition boundaries of the Doi model (1.28)-(1.30) with bifurcation software AUTO Doedel *et al.* (1997). Figure 1.3 gives the phase diagram for dynamics of the in-plane space \mathbf{Q}^{i-p} , then Figure 1.4 gives the phase diagram for the full tensor space. The three bifurcation curves emanating from the $Pe = 0$ axis are explained below. We shall employ this in-plane system for several purposes:

- As a model for monolayers in which molecular orientations are confined to the shear plane, see Fuller (1995), Marrucci and Maffettone (1989), Maffettone *et al.* (1996), Maruyama *et al.* (1998).
- As a model for dynamics of defect sets, and their role in the transient approach to attractors. This study will appear elsewhere (Yao *et al.* (2006)).
- As a simpler dynamical system in which we can develop statistical diagnostics for attractor properties.
- When compared with the full tensor model (Figure 2), the results of Figure 1 and the diagnostics developed in this chapter provide a means to determine: (i) which monodomain solutions are stable in \mathbf{Q}^{i-p} , yet unstable to out-of-plane perturbations, and how strong the out-of-plane instabilities are; and (ii) for in-plane solutions (**FA**, **T** or **W**, **LR**) stable in the full tensor space, whether the slowest modes of decay to the attractor are in-plane or out-of-plane.

For the purpose of comparison, we also give the full kinetic flow phase diagram, Figure 1.5 from (Forest *et al.* (2004b)). The entire monodomain phase diagram of a finite-aspect-ratio nematic fluid in a linear flow field is equivalent to the phase diagram of an infinite-aspect-ratio fluid (thin rods or disc) in a related linear velocity field.

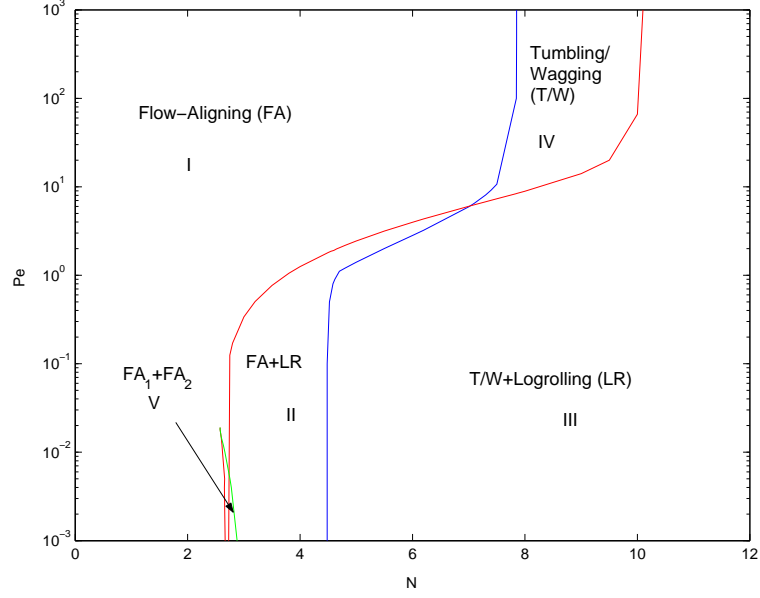


Figure 1.3: The monolayer flow-phase diagram of the Doi closure model with constant rotary diffusivity, for confined *in-plane orientation tensors* and molecule aspect ratio $r = 3$ or $\frac{1}{3}$. The diagram depicts all stable monodomain states versus nematic concentration (N) and normalized shear rate (Pe). The bifurcation curves bound regions of fixed number and type of attracting states, corresponding to flow and concentration-induced phase transitions among confined in-plane attractors.

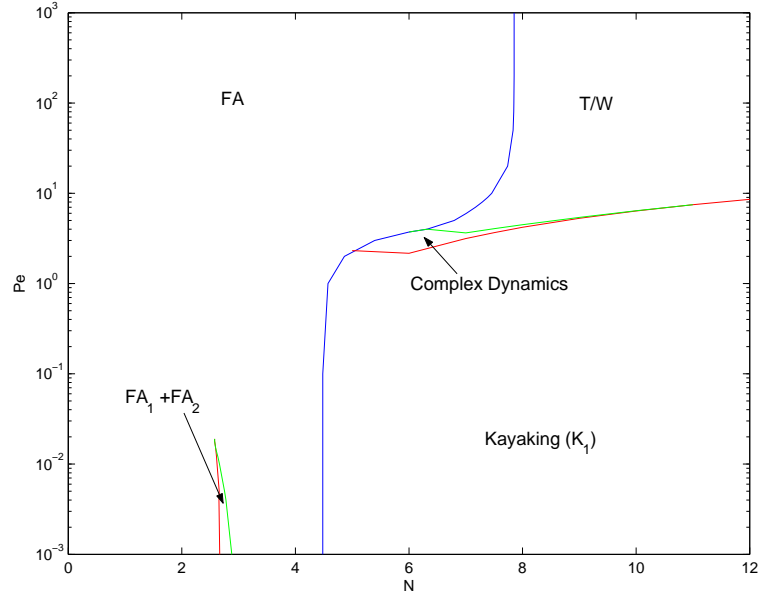


Figure 1.4: The full tensor flow-phase diagram of the Doi mesoscopic closure model, for aspect ratio $r = 3$ or $\frac{1}{3}$, constant rotary diffusivity, variable concentration (N) and normalized shear rate (Pe). The details of the “complex dynamics region” are discussed in Forest and Wang (2003), see also Rienacker and Hess (2002).

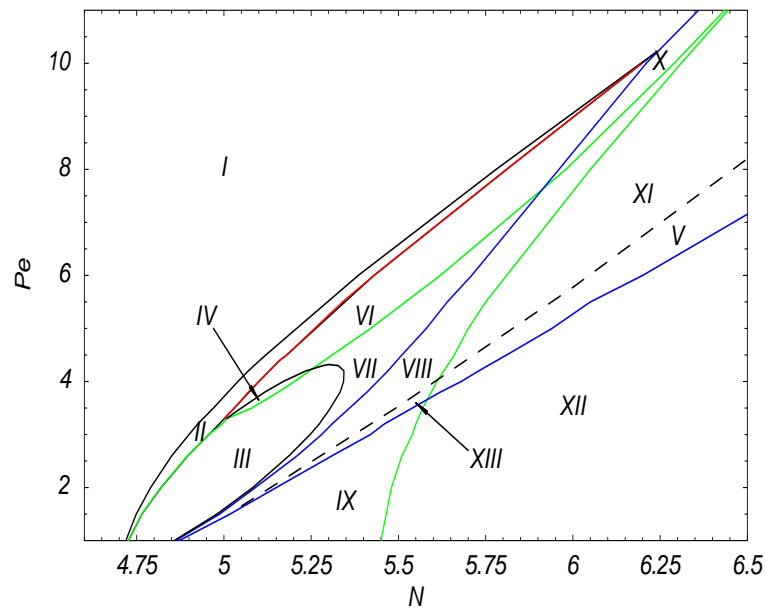


Figure 1.5: Kinetic monodomain flow phase diagram versus concentration N and Peclet number Pe , for aspect ratio $a = 1$. Forest *et al.* (2004b))

Region	Attractor type	Attractor multiplicity
I	Flow-aligning (FA)	1
II	Out-of-plane (OS)	2
III	Kayaking 1/Chaos (K_1 /CH)	2
IV	Chaos (CH)	1
V	Tumbling 1/Log-rolling (T/LR)	2
VI	Kayaking 2 (K_2)	2
VII	Kayaking 1/Kayaking 2 (K_1/K_2)	3
VIII	Kayaking 1/Wagging (K_1 /W)	2
IX	Kayaking 1 (K_1)	1
X	Wagging (W)	1
XI	Wagging/Log-rolling (W/LR)	2
XII	Log-rolling (LR)	1
XIII	Kayaking 1-Tumbling (K_1 /T)	2

Table 1.1: The set of stable bulk monodomain responses in the regions depicted in Figure 1.5.

1.6 Likelihood and expected time statistics of monodomain attractors

1.6.1 Motivation

In confined flows of initially homogenous nematic polymers, a key factor in the evolution of mesostructure is the likely timescale, denoted by $\langle t \rangle_{\mathbf{A}}$, on which monodomain mesophase attracting states, denoted by \mathbf{A} , are resonated by the imposed flow. These monodomain modes (flow-aligning (**FA**), logrolling (**LR**), tumbling (**T**), wagging (**W**), kayaking (**K**), chaotic (**CH**)) are important precursors to onset and generation of structure *if* they have time to set up in the interior of the flow sample. Flow-induced monodomain attractors are expected in experiments if the following all hold: (1) the experiment is longer than $\langle t \rangle_{\mathbf{A}}$ for the relevant attractor(s) \mathbf{A} ; (2) the initial sample is not riddled with defects; (3) $\langle t \rangle_{\mathbf{A}} < t_{\partial}$, where t_{∂} is the timescale on which boundary layers induced by anchoring conditions (at plates, solid boundaries, or even pinned defects) propagate to the interior and alter the pure shear response of local monodomains. When $\langle t \rangle_{\mathbf{A}} > t_{\partial}$, nonhomogeneities generate a more complex evolution, and the monodomain restriction is not valid due to strong spatial mode coupling. For small molecule nematic polymers in plane Couette cells, this condition ($\langle t \rangle_{\mathbf{A}} < t_{\partial}$) is typically satisfied and MD modes are well documented on experimental timescales. Several authors (Larson (1999), Larson and Ottinger (1991), Van Horn *et al.* (2003), Rey and Tsuji (1998)) have studied the transients from initial quiescent nematic liquids to monodomain attractors. *The purpose of this study is to provide statistical diagnostics for the expected time, $\langle t \rangle_{\mathbf{A}}$, to resonate MD attractor \mathbf{A} in sheared nematic polymers, for all attractor types **FA**, **LR**, **T**, **W**, **K**, **CH**.* We perform statistical averaging over typical experimental initial conditions: the set of quiescent nematic equilibria when the experiment begins at rest.

We develop these diagnostics using a standard mesoscopic tensor model. In particular, we overlay the expected time, $\langle t \rangle_{\mathbf{A}}$, with flow phase diagram of MD attractors to converge to attractors from the orientationally degenerate nematic rest state. We study dynamics of confined in-plane versus full orientation tensors, which allows us to easily flag the slowest decaying tensor modes for in-plane attractors (**FA**, **T**, **W**, **LR**) across the phase diagram, and

to flag which in-plane solutions are unstable to out-of-plane perturbations. Finally, for bi-stable and tri-stable parameter regimes, we determine which pre-aligned quiescent equilibria go to which attractor, i.e., their respective domains of attraction, and monitor rheological properties of the transient orbits during their evolution, following Van Horn *et al.* (2003).

Our primary goal here is to determine the “*strength*” and “*likelihood*” of attractors. A secondary goal is to clarify the timescale on which in-plane stable response will build up out-of-plane instabilities and depart from the shearing plane. There are several ways we might quantify “*strength*”, where strong versus weak is based on the rapid versus slow rate of approach to an attractor. We first consider the in-plane attractors from Figure 1, with $Q_{xz} = Q_{yz} = 0$, to develop the statistical tools.

1.6.2 Parametrization of the experimental initial data set

We study experimental systems beginning from rest. Thus *the set of admissible data is given by the stable quiescent equilibria of the Doi model* (1.27)-(1.30), which consist of the isotropic phase $\mathbf{Q} \equiv 0$ for $N < 3$, a bi-stable region for $\frac{8}{3} < N < 3$, and the nematic region $N > 3$, where the nematic phase is given by:

$$\begin{aligned} \mathbf{Q}(0) &= \mathbf{Q}_{eq} = s(N)(\mathbf{n}^t \mathbf{n} - \mathbf{I}/3), \\ \mathbf{n} &= (\cos \phi_0 \sin \theta_0, \sin \phi_0 \sin \theta_0, \cos \theta_0)^T, \quad \phi_0 \in [0, 2\pi], \quad \theta_0 \in [0, \frac{\pi}{2}), \\ s(N) &= \frac{1 + 3\sqrt{1 - \frac{8}{3N}}}{4} \in [1/4, 1], \text{ if } N > \frac{8}{3}; \quad s(N) = 0, \text{ if } N < 3. \end{aligned} \tag{1.31}$$

The bifurcations at $N = \frac{8}{3}$ and $N = 3$ persist for $Pe > 0$, and have been explained in detail by several authors (Doi (1981), Larson (1990), Forest and Wang (2003), Forest *et al.* (2003)). The third bifurcation curve in Figure 1.3 and 1.4 which emanates from $Pe = 0$ at $N \approx 4.5$ is more subtle, in that it is created by the flow perturbation. As detailed in Forest and Wang (2003), Forest *et al.* (2003), this bifurcation corresponds to a steady-unsteady transition. Tumbling (**T**) emerges as the shear response for confined in-plane tensors (Figure 1.3) called the **FA-T** transition; as seen from Figure 1.4, however, out-of-plane kayaking \mathbf{K}_1 states also arise simultaneously with **T** states, and the **T** states are unstable to director tipping

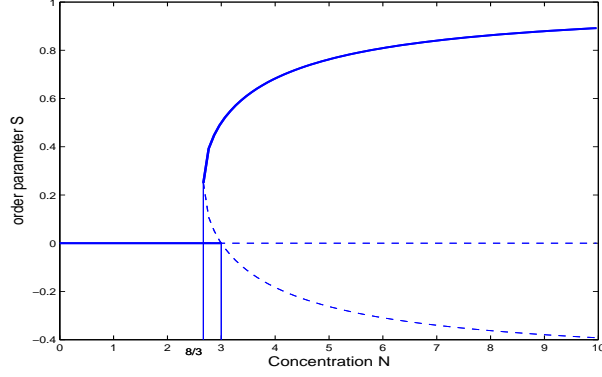


Figure 1.6: Order parameter versus concentration. The solid line is stable equilibrium, the dashed lines are unstable solution. There is a first order transition, which is discontinuous, hysteresis. The bistable region is between $N = 8/3$ and $N = 3$.

until much higher shear rates. To characterize the steady-unsteady transition curve of both phase diagrams, one considers the weak flow limit, from which a Leslie tumbling parameter λ_{Leslie} is derived, and the unsteady transition occurs when $\lambda_{\text{Leslie}} = \pm 1$. For the Doi closure one finds $\lambda_{\text{Leslie}}^{\text{Doi}} = \frac{a(2+s)}{3s}$. For $a = \pm 0.8$, and the equilibrium order parameter value $s = s(N) = \frac{1 + 3\sqrt{1 - \frac{8}{3N}}}{4}$, one finds $N \approx 4.5$, as the numerical diagrams of Figure 1.3,1.4 confirm.

Note that all nematic equilibria are orientationally degenerate, parametrized by $\mathbf{n} \in S^2$, with \mathbf{n} and $-\mathbf{n}$ identified. The degree of nematic ordering, $s(N)$, is uniquely prescribed by the nematic concentration N . As explained in Van Horn *et al.* (2003), Tan and Berry (2003), for example, various techniques are utilized to control plate anchoring of \mathbf{n} , which then sets the monodomain equilibrium value for $\mathbf{Q}(0)$, at least nearby the plates. In typical samples there are many monodomains, corresponding to a distribution of $\mathbf{n}(0)$, which is why this statistical study is relevant.

We also investigate the dynamics for special experimental major director data (θ_0, ϕ_0) from Van Horn and Winter (2000), to compare the behavior of their data set and predictions of the Leslie-Ericksen continuum model with our mesoscopic model statistics. Note in our choice of spherical coordinates, $\theta_0 = 0$ corresponds to vorticity-alignment and $\theta_0 = \frac{\pi}{2}$ corresponds to in-plane alignment with in-plane angle ϕ_0 . Only when $\theta_0 = \frac{\pi}{2}$ is the range of ϕ_0 restricted from $[0, 2\pi)$ to $[0, \pi)$.

1.6.3 Local and global measures of attractor “strength”

Local measure of strength for steady attractors

The traditional measure of stability of a **steady** solution is its linearized eigenvalues, which give all local decay rates for initial data that are sufficiently nearby the attractor. For this section we employ the vector form, (1.27), of the dynamical system, and by slight abuse of notation, continue to use F and G for the corresponding vector fields.

Let \bar{Q} be a steady solution from Figure 1, either **FA** or **LR**. If we expand Q in a neighborhood of \bar{Q} , $Q = \bar{Q} + \tilde{Q}$, insert the expansion into (1.30), and retain terms linear in the perturbation \tilde{Q} , then

$$\begin{aligned}\dot{\tilde{Q}} &= \mathbf{L}\tilde{Q}, \\ \mathbf{L} &= \mathbf{L}(\bar{Q}; N, a, Pe) = DF(\bar{Q}; N, a) + PeDG(\bar{Q}, \nabla \mathbf{v}; a),\end{aligned}\tag{1.32}$$

where DF and DG are the first variations of F and G , evaluated at the equilibrium \bar{Q} .

For any steady state \bar{Q} , the linearized operator \mathbf{L} is a constant, and all linearized solutions \tilde{Q} are constructed from the eigenvalues and eigenvectors of \mathbf{L} . We let $\{\tilde{Q}^{(1)}, \dots, \tilde{Q}^{(5)}\}$ denote a basis of eigenvectors of \mathbf{L} , and let $\{\lambda_1, \dots, \lambda_5\}$ denote the corresponding eigenvalues, ordered by

$$Re(\lambda_5) \leq Re(\lambda_4) \leq Re(\lambda_3) \leq Re(\lambda_2) \leq Re(\lambda_1).\tag{1.33}$$

The steady state \bar{Q} will be stable if $Re(\lambda_i) \leq 0$ for all i ; and asymptotically stable if $Re(\lambda_i) < 0$ for all i . Except possibly at the bifurcation curves of Figures 1.3, 1.4 all steady attractors have $Re(\lambda_1) < 0$, and λ_1 is simple.

Consider any data $Q(0)$ in a small neighborhood of \bar{Q} of size δ ,

$$\|Q(0) - \bar{Q}\| = \|\tilde{Q}(0)\| = \delta, \quad 0 < \delta \ll 1.$$

Then the slowest decaying mode is either 1-dimensional (if $\lambda_1 < 0$) or 2-dimensional (if $\lambda_1 = \lambda_2^*$). In either case the dominant term in the linearized solution $\tilde{Q}(t)$ for $t \gg 1$ is proportional to $e^{Re(\lambda_1)t}\tilde{Q}^{(1)}$. This allows one to infer a *local linearized timescale*, $t_{\text{local}} = -\frac{1}{Re(\lambda_1)}$, on which

the initial data Q_0 contracts from a δ -radius ball around \bar{Q} to a δ/e -radius ball. This picture of linearized flow nearby an attractor leads us to define a *local expected time of convergence to a steady stable state \mathbf{A}* ,

$$\langle t_{\text{local}} \rangle_{\mathbf{A}} = -\frac{1}{\text{Re}(\lambda_1)}. \quad (1.34)$$

The local strength of \mathbf{A} is then measured by how rapidly data converge to the attractor, so that

$$'local\ strength\ of\ attractor\ \mathbf{A}' \propto \langle t_{\text{local}} \rangle_{\mathbf{A}}^{-1} \propto |\text{Re}(\lambda_1)|.$$

For example if $\text{Re}(\lambda_1) \sim -10^{-3}$, then \bar{Q} is a very weak attractor, requiring $\langle t_{\text{local}} \rangle_{\mathbf{A}} \sim 10^3$ dimensionless time units for nearby initial data to decay by a factor of e^{-1} . Recall we have normalized time by the average molecular relaxation time, which is on the order of $10^{-1} - 10^2$ seconds for nematic polymers.

Local measure of strength for periodic attractors

We now consider the linearized stability of periodic solutions, which we denote $\bar{Q}(t)$, with

$$\bar{Q}(t+T) = \bar{Q}(t), \quad T = \text{period}.$$

If we expand Q in a neighborhood of $\bar{Q}(t)$, $Q(t) = \bar{Q}(t) + \tilde{Q}(t)$, then the linearized equation for $\tilde{Q}(t)$ has periodic coefficients given by \bar{Q} :

$$\dot{\tilde{Q}}(t) = \mathbf{L}(\bar{Q}(t); N, a, Pe)\tilde{Q}. \quad (1.35)$$

We summarize the basic elements of linear systems of the form (1.35), so-called Floquet theory. If $\tilde{Q}(t) = [\tilde{Q}^{(1)}, \dots, \tilde{Q}^{(5)}]$ is a fundamental matrix solution of (1.35), then $\tilde{Q}(t+T)$ is also a fundamental matrix solution since $\mathbf{L}(\bar{Q}(t))$ is periodic of period T . Therefore there is a nonsingular matrix $C = \tilde{Q}(T)\tilde{Q}^{-1}(0)$ such that

$$\tilde{Q}(t+T) = \tilde{Q}(t)C, \quad \tilde{Q}(t+nT) = \tilde{Q}(t)C^n.$$

The matrix C , called the transfer matrix, therefore characterizes asymptotic behavior of all

solutions of (1.35); the eigenvalues ρ of C are the characteristic multipliers of (1.35) and any λ such that $\rho = e^{\lambda T}$ is a characteristic exponent of (1.35). The system (1.35) will be stable if all multipliers satisfy $|\rho_i| \leq 1$ (the characteristic exponents satisfy $\text{Re}(\lambda_i) \leq 0$). In our system, we always have a simple multiplier 1 corresponding to an arbitrary phase shift of the periodic solution, *so we use the second largest multiplier ρ_2 to measure the slowest decay timescale, which gives the estimate, $\langle t_{\text{local}} \rangle_{\mathbf{A}} \sim O(-T/\log(|\rho_2|)) = O(-1/\text{Re}(\lambda_2))$.*

These local diagnostics do not apply to the experimental initial data set (1.31), which is generally far away from the steady or periodic attractors. The linearized diagnostics are however, predictors of expected-time to converge to attractors, and are accessible from numerical dynamical systems software AUTO (Doedel *et al.* (1997)).

‘Global’ measure of strength of a steady attractor

From arbitrary initial data, the relevant questions are: which attractor does the data converge to?; and, how long does it take to reach a prescribed neighborhood of that attractor? For nonlinear systems, except in rare exactly solvable systems, these questions can only be answered by statistics of numerical solutions for arbitrary initial data. We now develop the statistics.

At selected locations (N, Pe) inside the regions of Figure 1.3, i.e., the in-plane subspace Q^{i-p} , we monitor the eigenvalues $\lambda_j(t_n)$ of the local Jacobian, $\mathbf{L}(Q(t_n))$, which we then average over the attracting set for each steady attractor to construct $\langle \text{Re}(\lambda_j)(t_n) \rangle, j = 1, 2, 3$. We restrict to attractors away from the phase transition curves, since these bifurcations are often infinite-period, which will distort the statistics.

Statistics for low concentration, $N = 3.5$

To illustrate these ideas, we begin with the vertical slice, $N = 3.5$, of Figure 1.3, whose attractors versus Pe are given in Table 1.2 below. Let $\bar{Q}^{\mathbf{A}}$ denote the steady attractor, where $\mathbf{A} = \mathbf{FA}$ or \mathbf{LR} for the in-plane subspace, whereas $\mathbf{A} \equiv \mathbf{FA}$ for the full tensor space. Note this information from Figure 1.3, 1.4 already conveys that the \mathbf{LR} states of this model are all unstable to out-of-plane (i.e. director tipping) perturbations (Forest and Wang (2003)).

Indeed, **LR** stability is very sensitive to closure rule (Forest *et al.* (2003)). Appealing to the Doi kinetic theory to resolve this issue, one finds a significant parameter regime of stable logrolling states for large N , and low Pe , see (Forest *et al.* (2004a), Forest *et al.* (2004b)), including bi-stable **T** and **W** states. Thus, Figures 1.3 and 1.4 show the Q^{i-p} model is more faithful to kinetic theory than the full tensor model in regard to preservation of **LR** attractors! We return to this topic in section 1.6.4.

Table 1.2: Stable solutions of the Doi model versus Peclet number, for a fixed nematic concentration $N = 3.5$, and for a 1:3 discotic or 3:1 rod-like nematic polymer aspect ratio. On the left are in-plane confined dynamics, on the right is the full tensor result.

In-plane Attractors	FA+LR	FA	Full tensor Attractors	FA
Range of Pe	(0, 0.77)	(0.77, 10)	Range of Pe	(0, 10)

We numerically solve both ODE systems (Q^{i-p} and full Q) and monitor two measures of “Distance between the orbit at time t and the attractor”,

$$D_1 = \left\| \frac{Q(t) - Q^{\mathbf{A}}}{Q^{\mathbf{A}}} \right\|, \quad D_2 = \left\| \frac{Re(\lambda_1(t_n)) - Re(\lambda_1)}{Re(\lambda_1)} \right\|.$$

The first distance function $D_1(t)$ keeps track of the closeness of the tensors along the orbit $Q(t)$ to the respective attractor $Q^{\mathbf{A}}$, while the second distance function $D_2(t)$ monitors closeness of the maximum eigenvalues (i.e. slowest decay rate) of the linearized vector field along the orbit and at the steady state. We compute a family of orbits through the initial data set (1.31), by taking 100 choices for $\phi(0) \in [0, \pi)$ for the Q^{i-p} system, and 500 random choices, $(\phi(0), \theta(0)) \in [0, 2\pi) \times [0, \frac{\pi}{2}]$ for the full tensor system. In regions with multiple attractors, we first compute which subsets of each data set ($\phi(0) \in S^1$ or $(\phi(0), \theta(0)) \in S^2$) converge to each attractor, and then sample from these attracting sets. We stop each orbit at $t_{\text{stop}}(\phi(0))$, or, $t_{\text{stop}}(\phi(0), \theta(0))$, respectively, when $D_1(t)$ or $D_2(t)$ lies within a prescribed neighborhood.

Figure 1.7 compares the confined in-plane attractors and properties with the full tensor results. From Figure 1.4 and Table 1.2, we fix $N = 3.5$ and $r = \frac{1}{3}$ ($a = -0.8$) to compare with the in-plane results. The only full tensor attractor is **FA**, the **LR** states are therefore unstable to out-of-plane (director tipping) instabilities. For this reason, we don’t give statistics of the **LR** state. *The key issue now is whether the slowest decaying mode to the **FA** state is in-plane,*

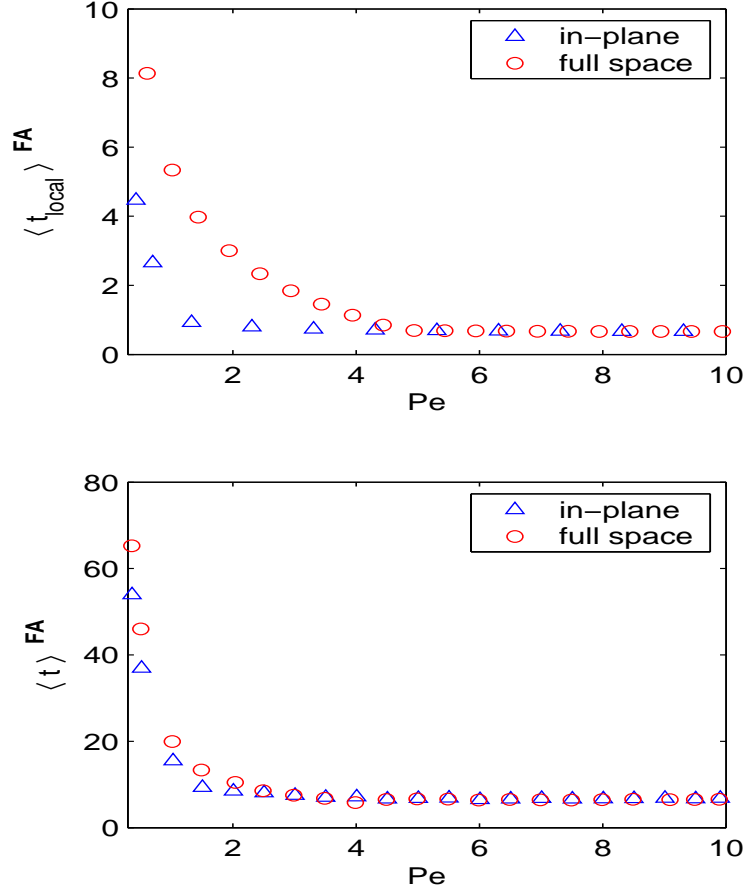


Figure 1.7: In-plane statistics versus that of the full tensor space for the expected time to converge to \mathbf{FA} , with nematic concentration $N = 3.5$, aspect ratio $r = \frac{1}{3}$ and distance function $D_2 < 10^{-3}$. Left: Local measure; right: Global measure.

or out-of-plane.

Conclusions from Figure 1.7:

- Figure 1.7a: At low $Pe < 4.8$, the slowest decaying modes are out-of-plane, whereas for $Pe > 4.8$ the out-of-plane linearized components decay on the same timescale (or even faster for higher Pe).
- Figure 1.7b: A similar qualitative behavior as Figure 1.7a emerges for the global statistic, $\langle t \rangle_{\mathbf{FA}}$, though less significant differences are seen at low Pe . Taken together, these statistics imply that the transient dynamics dominates Figure 1.7b at low Pe . Approximately 80% of the global statistic $\langle t \rangle_{\mathbf{A}}$ is spent getting to a neighborhood of the attractor.

To illustrate the statistics of Figure 1.7, we give details of selected sample orbits. For

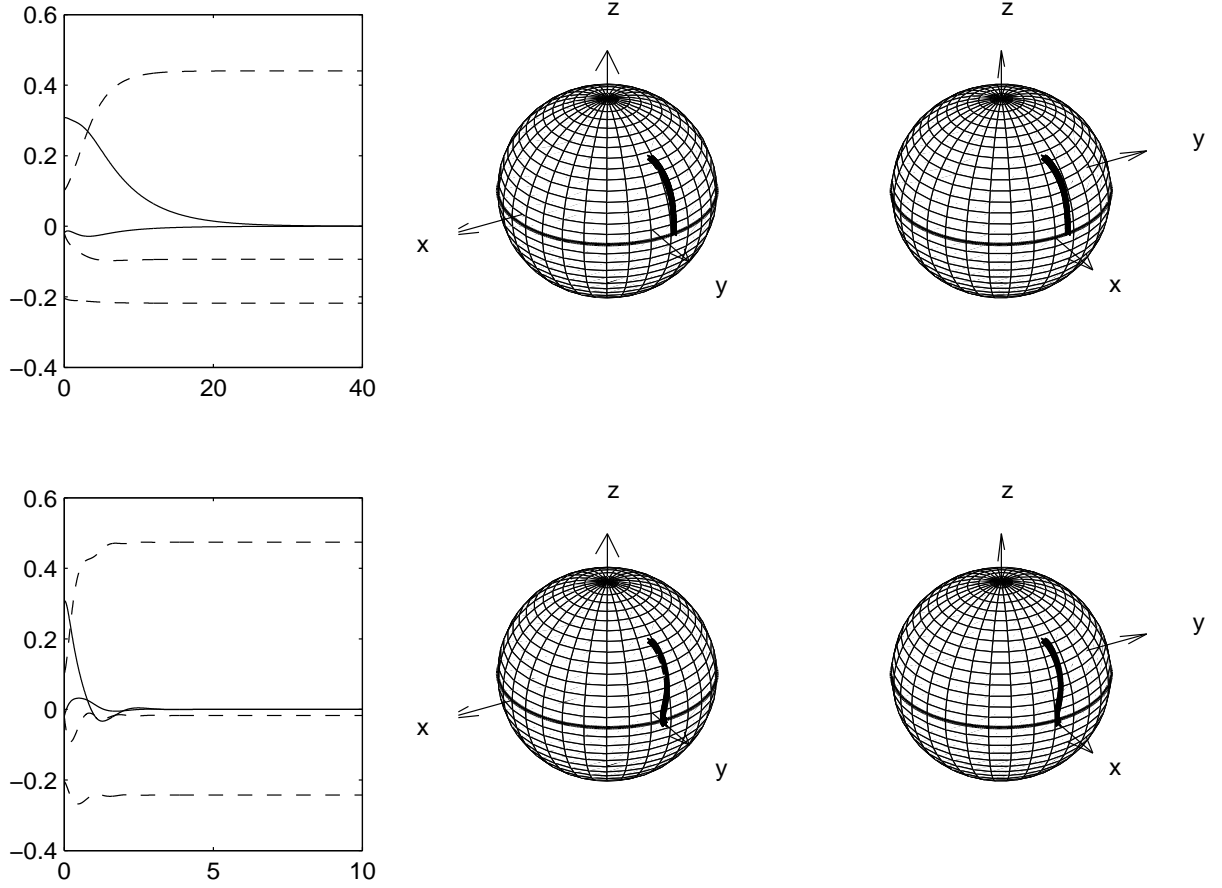


Figure 1.8: Sample orbits to **FA** attractors for $Pe = 1$ (top row) and $Pe = 10$ (bottom row). Column 1: the components of \mathbf{Q} vs time. Column 2: path of the major director for discotic nematic polymers from initial condition $\phi_0 = 93.6^\circ, \theta_0 = 45^\circ$. Column 3: path of the major director for rod-like nematic polymers from initial condition $\phi_0 = 3.6^\circ, \theta_0 = 45^\circ$. The concentration $N = 3.5$, which is in the quiescent nematic range, but below the tumbling transition at onset of shear.

$Pe = 1$, from Figure 1.8a (top left), clearly the out-of-plane components (solid lines) converge to equilibrium values slower than the in-plane components (dashed lines); Figure 1.8b (top middle) illustrates this behavior in terms of the path of the major director \mathbf{n} on the sphere for discotic nematic polymers with $a = -0.8$. We choose $\mathbf{n}(0)$ with $\theta_0 = 45^\circ$ and $\phi_0 = 93.6^\circ$ as initial condition. The major director converges in-plane, close to the flow-gradient (y) axis, with $\phi_L^{\text{disc}} = 97.91^\circ$. For platelets, this means the plane of the molecule is nearly aligned in the $x-z$, or flow-vorticity plane. Figure 1.8c (top right) conveys the path of the major director for rod-like nematic polymers with $a = 0.8$.

Comments: Out-of-plane behavior is observed by the major director wandering across latitudes, while the in-plane behavior corresponds to the major director wandering across

longitudes.

We use this opportunity to illustrate the symmetry between rods and platelets in shear (Forest *et al.* (2002b)), $(a, \mathbf{n}) \rightarrow (-a, R \cdot \mathbf{n})$, where R is a pure clockwise rotation by $\pi/2$ radians, in the shearing plane that fixes the vorticity axis,

$$R = \begin{pmatrix} 0 & 1 & 0 \\ -1 & 0 & 0 \\ 0 & 0 & 1 \end{pmatrix}. \quad (1.36)$$

Instead of $\mathbf{n}(0)$ above for platelets, we choose $R \cdot \mathbf{n}(0)$, i.e. $\theta_0 = 45^\circ, \phi_0 \approx 3.6^\circ$ as initial data for rods. Both theoretically and by numerical confirmation, the path of the major director remains identical up to an in-plane rotation of 90° , converges in-plane, nearby the flow direction, with the in-plane Leslie alignment angle $\phi_L^{\text{rod}} \approx 7.91^\circ$, i.e., $\phi_L^{\text{rod}} = (\phi_L^{\text{disc}} + 90^\circ) \bmod \pi$.

For $Pe = 10$, Figure 1.8d (bottom left) shows the out-of-plane components converge at approximately the same rate as in-plane components. Figure 1.8e (bottom middle) shows the path of the major director for discotic polymers with $a = -0.8$, from initial condition $\mathbf{n}(0)$, the orbits converge to $\phi_L^{\text{disc}} \approx 92.38^\circ$. Figure 1.8f shows the major director orbit for rod-like polymers with $R \cdot \mathbf{n}(0)$, and the in-plane Leslie alignment angles are $\phi_L^{\text{rod}} \approx 2.38^\circ$. For higher shear rates, the Leslie angle for rod-like polymers approaches the flow axis, whereas the Leslie angle for platelets approaches the flow gradient axis.

Figures 1.9a,b indicate the rheological properties during the transient approach to the **FA** attractors depicted in Figure 1.8. Recall that the first and second normal stress differences are $N_1 = \tau_{xx} - \tau_{yy}$, $N_2 = \tau_{yy} - \tau_{zz}$, and the apparent shear viscosity is $\eta = \tau_{xy}/Pe$. The transient rheology is surprisingly different at low and high shear rates: the high shear rate, strong attractor with short convergence time, has stress oscillations in N_1 and η that do not show up in the low shear rate case. Furthermore, the shear stress (apparent viscosity) drops approximately 40%, while the first normal stress differences increase by similar amounts, as Pe increases from 1 to 10. For the discotic aspect ratio $r = \frac{1}{3}$, the steady state values and transient features of N_1 and η are similar for typical **FA** parameter regimes, while N_2 experiences a factor of 4 reduction in magnitude. In general, independent of the attracting state, $\langle N_1 \rangle$ and $\langle \eta \rangle$ are

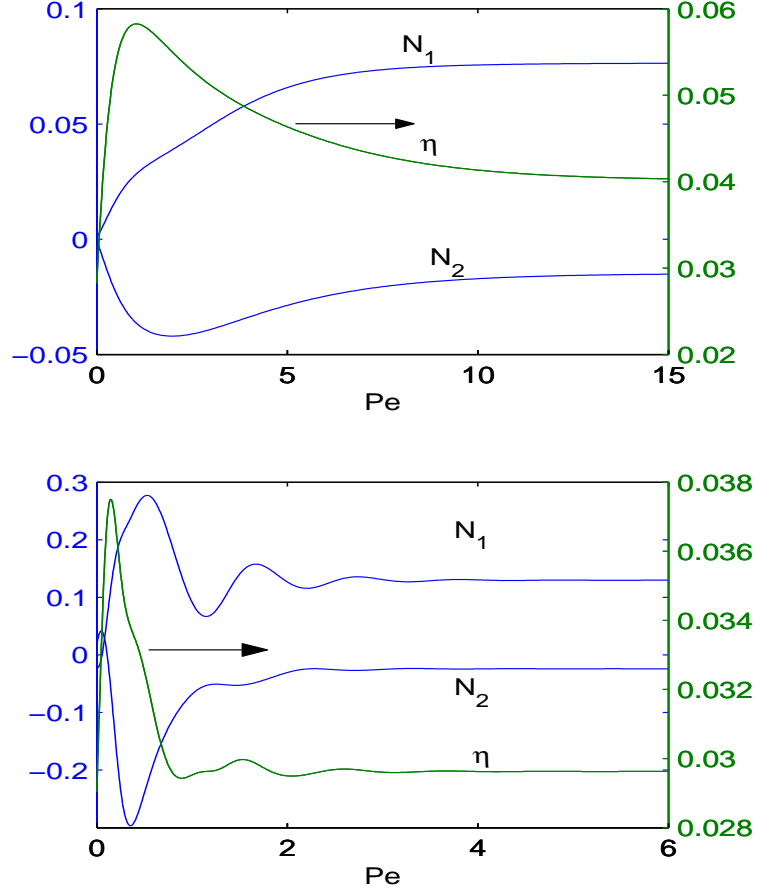


Figure 1.9: First and second normal stress differences N_1 , N_2 (left axis scale), and apparent viscosity η (right axis scale) versus time, in transient approach to **FA** attractor of Table 1.2, with $N = 3.5$, $a = 0.8$. Top row is for $Pe = 1$, bottom row is for $Pe = 10$. In each case, the initial director is tilted out-of-plane with polar coordinates $\phi_0 = 3.6^\circ$, $\theta_0 = 45^\circ$.

insensitive to rod versus platelet aspect ratio, whereas $\langle N_2 \rangle$ can either be larger or smaller in magnitude, as shown in Figures to follow.

We now make comparisons of the Doi model with recent experiments and Leslie-Ericksen model predictions of Van Horn *et al.* (2003) for **FA** nematic liquids. Figure 1.10 depicts the normalized Leslie alignment angle $\Phi = \frac{\phi - \phi_0}{\phi_L - \phi_0}$ as in Van Horn *et al.* (2003). To compare with their experimental data, we choose $N = 3.5$, $Pe = 1$ for rod-like nematic polymers with $a = 0.8$, which yields ϕ_L close to the equilibrium Leslie angle $\phi_L = 8.5^\circ$ of the Leslie-Ericksen model. As the out-of-plane tilt angle θ_0 ranges from $\theta_0 = 9^\circ$ (near the vorticity axis) to $\theta_0 = 81^\circ$ (near the shearing plane), Figure 1.10a shows the transient director goes from a strong overshoot to monotone convergence to the equilibrium ϕ_L . The out-of-plane polar angle θ , however,

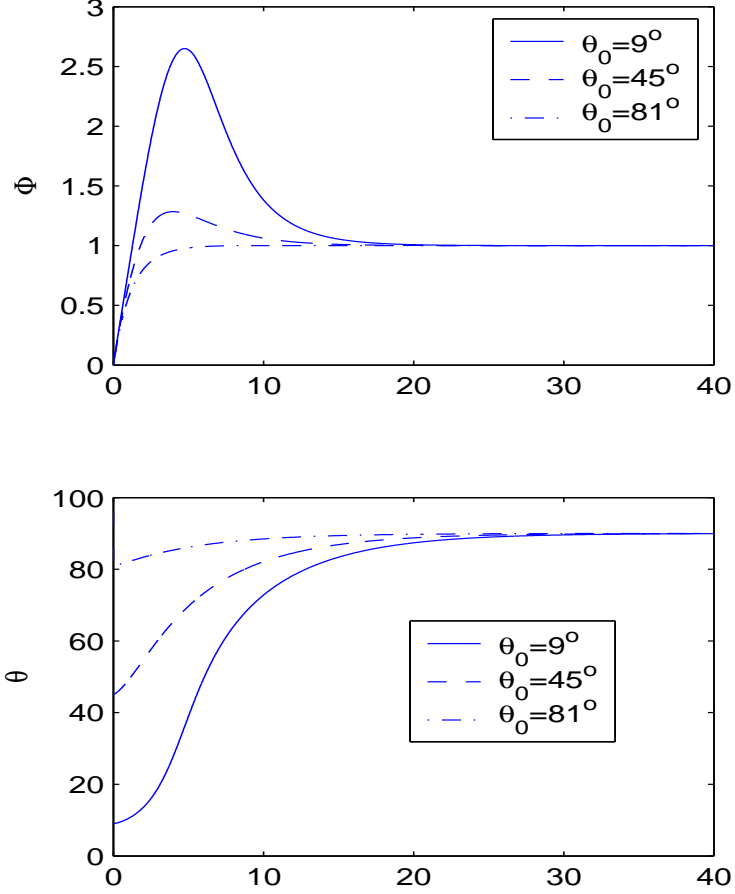


Figure 1.10: Mesoscopic predictions for the start-up of shear flow of the relative Leslie alignment angle Φ with $\phi_0 = 3.6^\circ$, $\phi_L = 7.91$, and initial out-of-plane tilt angles $\theta_0 = 9^\circ, 45^\circ, 81^\circ$, respectively. $Pe = 1$, $N = 3.5$, $a = 0.8$.

increases monotonically to 90° for all θ_0 , Figure 1.10b. These data show the mesoscopic tensor model reproduces Leslie-Ericksen behavior of the director only when the initial director is close to the shearing plane. The overshoot behavior for out-of-plane initial directors does not occur in the Leslie-Ericksen model (Van Horn *et al.* (2003)). The stress signature of the director overshoot of Figure 1.10a is seen from the $\theta_0 = 45^\circ$ plots of N_2 and η Figure 1.9 (top row).

Statistics for high concentration, $N=6$

We next increase the concentration to $N = 6$ in Figures 1.3, 1.4, which accesses complex out-of-plane dynamics. For this subsection, we will focus on the **FA** states to distinguish high concentration from low concentration **FA** states analyzed above.

Consider the **FA** states in Table 1.3. Figure 1.11 gives the expected time for convergence,

Table 1.3: Stable solutions of the Doi tensor model versus Peclet number, for a fixed nematic concentration $N=6$, and for 1 : 3 discotic or 3 : 1 rod-like nematic polymer aspect ratio. The top row is for in-plane confined dynamics, Figure 1.3; the bottom two rows are the full tensor result, Figure 1.4.

In-plane Attractors	LR+T/W	FA+LR	FA	
Range of Pe	(0, 2.819)	(2.819, 3.979)	(3.979, 10)	
Full-tensor Attractors	K₁	K₁+W	K₂^{+,−} + K₁	
Range of Pe	(0, 2.162)	(2.162, 2.405)	(2.405, 2.536)	
Full-tensor Attractors	K₁+CH	CH	K₂^{+,−}	FA
Range of Pe	(2.536, 2.923)	(2.923, 3.245)	(3.245, 3.717)	(3.717, 10)

which is very similar to the low concentration statistics of Figure 1.7. When $3.717 < Pe < 5.1$, out-of-plane modes dominate the expected time, whereas for $Pe > 5.1$, the out-of-plane modes do not slow the convergence of purely in-plane dynamics.

Figure 1.12 illustrates the statistical averages of Figure 1.11 with sample orbits. From Figure 1.12a, the out-of-plane components (solid lines) converge to 0 slower than in-plane components (dashed lines) when $Pe = 4$; and Figure 1.12b illustrates this behavior through the major director for discotic nematic polymers with aspect ratio $a = -0.8$ from initial condition $\phi_0 = 93.6^\circ, \theta_0 = 45^\circ$. Figure 1.12c shows the path of the major director for rod-like nematic polymers with symmetric initial condition, $\phi_0 = 3.6^\circ, \theta_0 = 45^\circ$. By contrast, Figure 1.12d shows the out-of-plane components damp prior to convergence of in-plane components when $Pe = 10$; Figures 1.12e,f show the corresponding path of the major director for discotic and rod-like polymers, respectively.

‘Global’ measure of strength of a periodic attractor

Now we proceed to discuss expected-time statistics for convergence to periodic solutions for $N=6$, Table 1.3. The components of \mathbf{Q} trace out closed trajectories, and a different measure of distance from the attractor is required. We use the classic distance (D_3) from a point \vec{Q} of the form of (1.27) to a bounded set of points $\{\vec{Q}(j)\}_{j=1}^M$ for 5-dimensional vectors

$$D_3 = \min\left\{\sum_{i=1}^5 |\vec{Q}_i - \vec{Q}_i(j)|\right\}. \quad (1.37)$$

First we compute the limit cycle numerically, and then represent the orbit in terms of a set of M points, $\{\vec{Q}(j)\}_{j=1}^M$, uniformly distributed in Q -component space as opposed to distributed

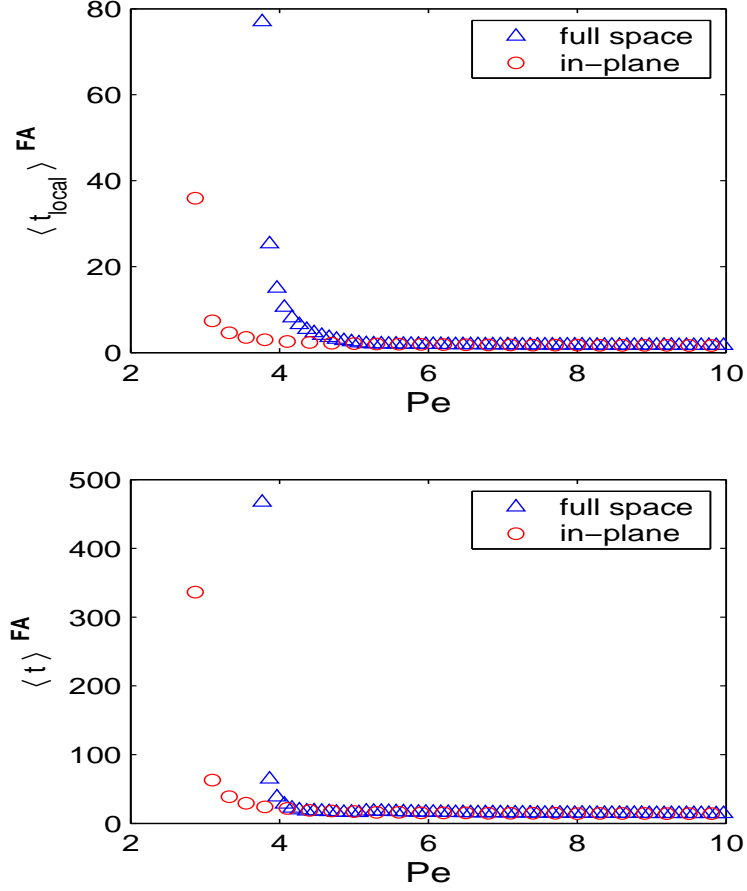


Figure 1.11: In-plane statistics versus that of the full tensor space for the expected time to converge to \mathbf{FA} , fixed nematic concentration $N = 6$, aspect ratio $a = -0.8$ and distance function $D_2 < 10^{-3}$. Left: local measure; Right: global measure.

in time along the periodic orbit. The distance $\|\vec{Q}(j+1) - \vec{Q}(j)\|$ between two neighboring points on the orbit is set at 10^{-3} , which has been chosen such that robust statistics are achieved.

Next, we compute a family of orbits for random data chosen from the initial data set (1.31), and keep track of the distance between the trajectories and the attractor. We stop each orbit at t_{stop} when the distance lies within a prescribed neighborhood (10^{-3}) of the numerically resolved exact solution. We then confirm in selected cases that the trajectory stays in the small tubelike neighborhood of the periodic solution after t_{stop} .

To make things simpler, we consider the in-plane case first: Table 1.3 shows that \mathbf{T}/\mathbf{W} occurs for $Pe < 2.819$ for confined in-plane dynamics when $N = 6$. (Note these orbits are stable for $2.162 < Pe < 2.405$, but unstable in the $0 < Pe < 2.162$ full-tensor space to director tipping, but we suppress these degrees of freedom for Figures 2.9, 1.14.)

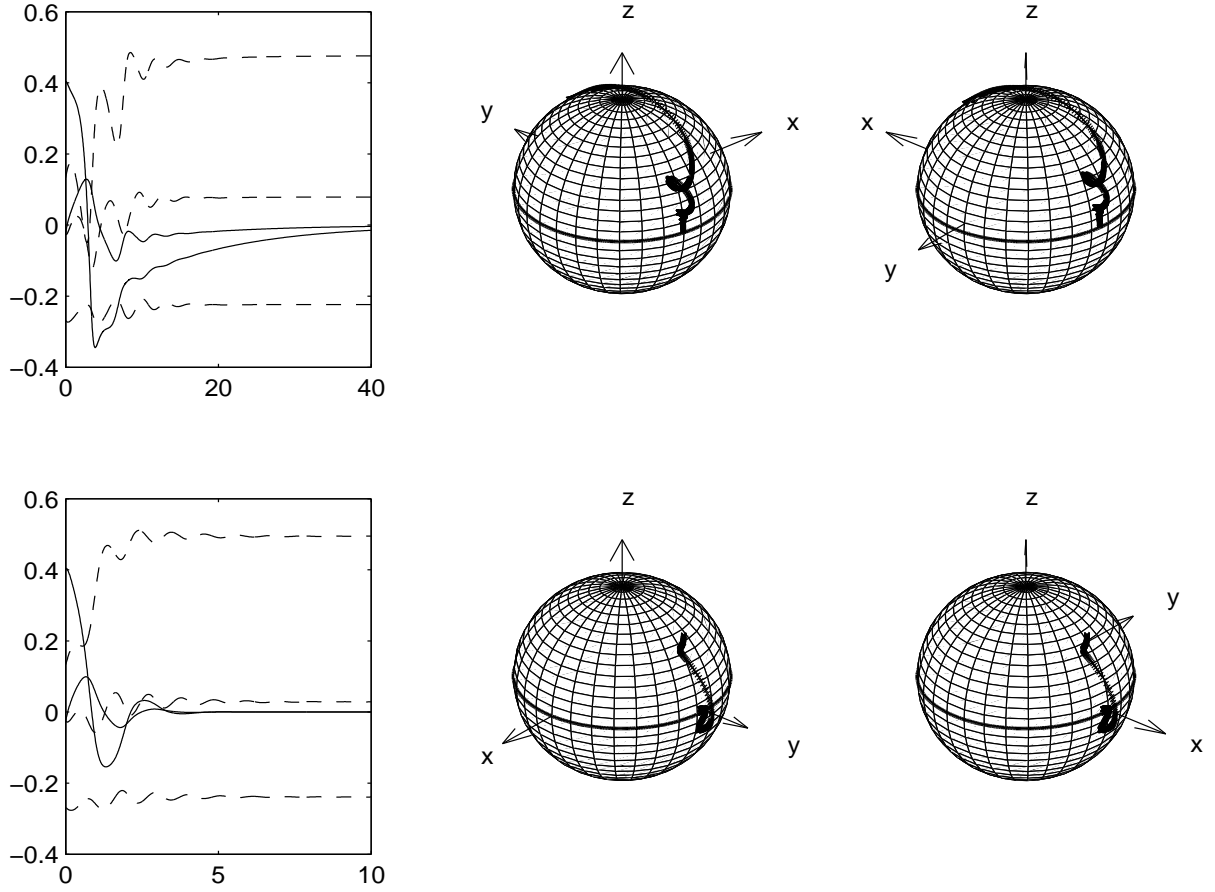


Figure 1.12: Sample paths for **FA** attractors in the high concentration ($N = 6$), strong shear ($Pe = 4, 10$) regime. Column 1: the components of \mathbf{Q} vs time. Column 2: path of the major director for discotic nematic polymers from initial condition $\phi_0 = 93.6^\circ$, $\theta_0 = 45^\circ$. Column 3: path of the major director for rod-like nematic polymers from initial condition $\phi_0 = 3.6^\circ$, $\theta_0 = 45^\circ$. Top row $Pe = 4$; bottom row $Pe = 10$.

Figure 2.9a calculates $-T/(\log(|\rho_2|))(T = \text{period})$, which is the definition of $\langle t_{\text{local}} \rangle$. Figure 2.9b shows the global statistics, indicating that from a random initial condition, the trajectory rapidly converges to the tumbling or wagging attractor. Figure 1.14 depicts N_1 and η for the quick transient and then several periods of the tumbling orbits in this instance.

We now recognize that for $0 < Pe < 2.162$ the **T&W** attractors for $N = 6$ are unstable to out-of-plane (director tipping) instabilities. Nonetheless, if the initial director is aligned in-plane, there is a competition between strong in-plane convergence to **T&W** limit cycles, and relatively weak out-of-plane instability. We are thus led to ask: if the **T** or **W** attractor is resonated, how many periods of the in-plane limit cycle are traversed before the orbit is expected to escape out-of-plane? This question is answered by the Floquet multipliers of

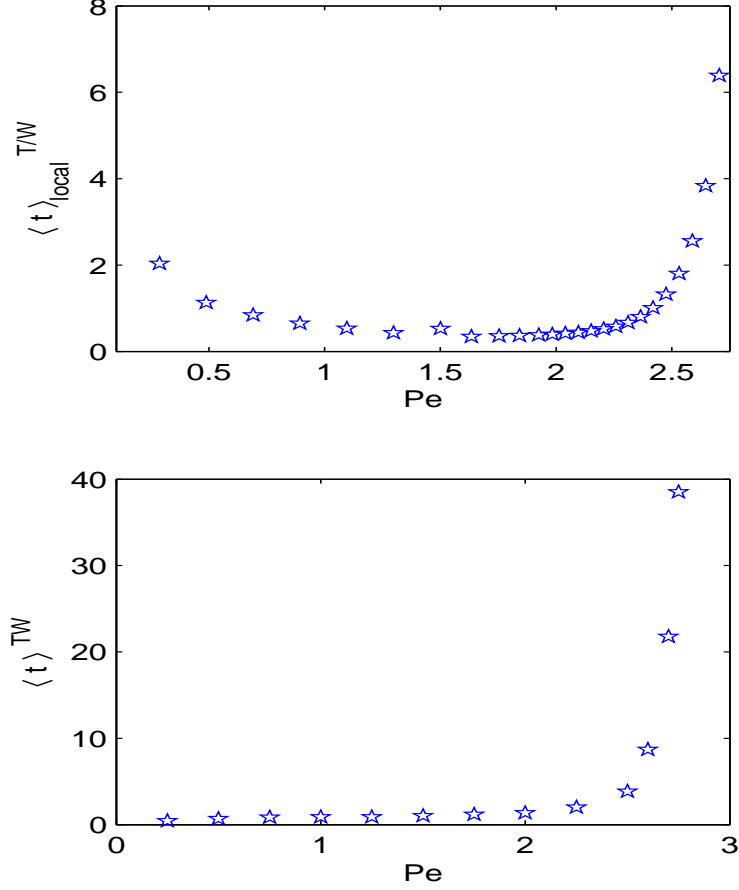


Figure 1.13: In-plane statistics for the expected time to converge to \mathbf{T}/\mathbf{W} attractors of Table 1.3, for confined in-plane dynamics, with nematic concentration $N = 6$.

Figures 1.3, 1.4, discussed in Section 2.2. For $N = 6, |a| = 0.8, Pe = 0.5$, the in-plane limit cycle is tumbling. We compute that the unstable Floquet multiplier is $\rho = 1.08$, the period $P_{\mathbf{T}}$ of the \mathbf{T} orbit is $P_{\mathbf{T}} = 33$, from which we deduce the linearized timescale of instability, $t_{\text{inst}} = P/\log(\rho) \approx 13P_{\mathbf{T}}$, which means it takes 13 director rotations or 430 relaxation units to escape the tumbling attractor! For $N = 6, |a| = 0.8, Pe = 2.02$, the in-plane attractor is wagging, with period $P_{\mathbf{W}} = 8.7$, the unstable multiplier is $\rho = 1.29$, which implies $t_{\text{inst}} \approx 4P_{\mathbf{W}}$, which means it takes 4 wagging cycles (35 relaxation time units) to escape out-of-plane. These properties suggest an experiment of limited duration may very likely observe \mathbf{T} or \mathbf{W} transient behavior, even though longer experiments will escape into out-of-plane response.

Next, we explore the expected convergence times for out-of-plane limit cycles. The above results, showing long times just to build up the out-of-plane components Q_{xz}, Q_{yz} , foreshadow

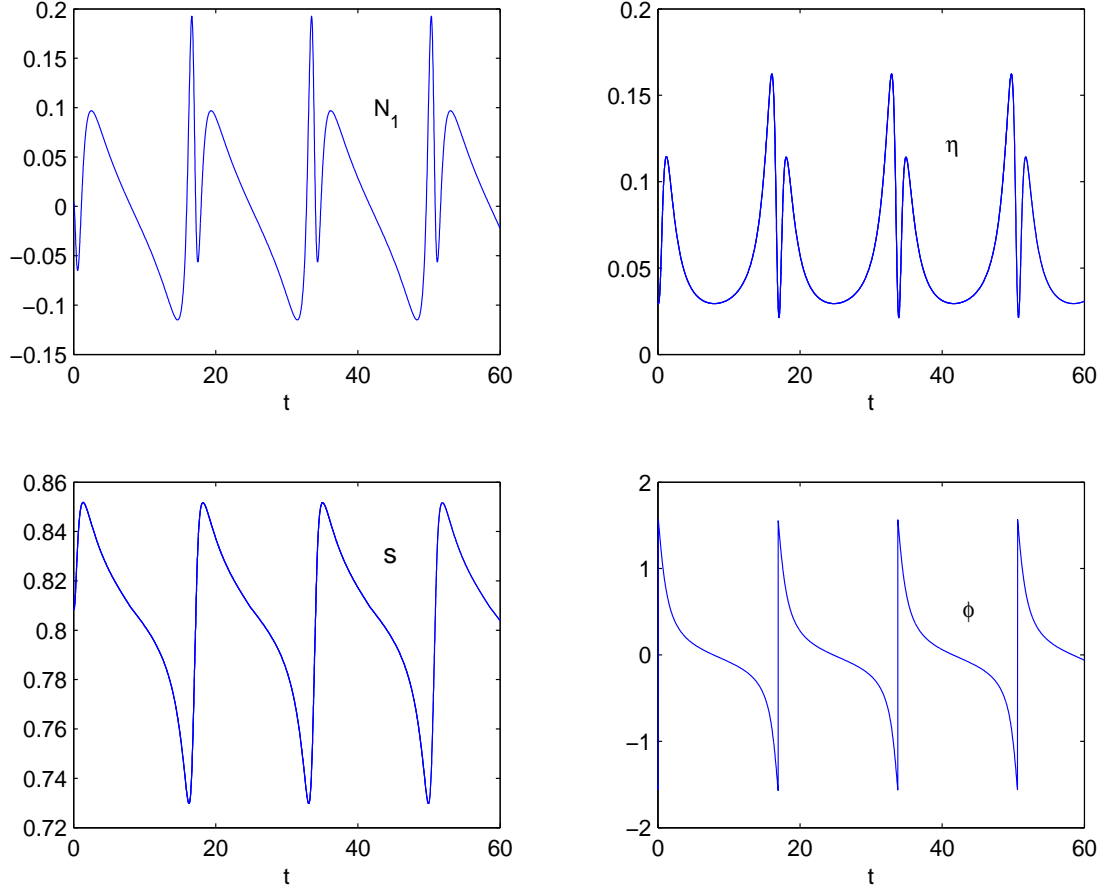


Figure 1.14: First normal stress difference N_1 (left), apparent viscosity η (right) versus time, for a randomly chosen orbit converging to a \mathbf{T} attractor of Table 1.3, with Peclet number $Pe = 1$, $N = 6$. The averages over one period are $\langle N_1 \rangle \approx 1.5 \times 10^{-2}$, $\langle N_2 \rangle \approx -10^{-3}$, $\langle \eta \rangle \approx 7 \times 10^{-2}$, with large deviations by factors of 10 for N_1 and 2 for η .

long convergence times to the out-of-plane attractors.

For Figure 1.4 and Table 1.3, the full tensor model for $N = 6$ has a complex shear response vs Pe . There are two types of kayaking attractors, the standard \mathbf{K}_1 whose major director rotates around the vorticity axis, and mirror-symmetric states $\mathbf{K}_2^{+,-}$ which occur in bi-stable pairs whose major director rotates between the vorticity axis and shearing plane (Forest and Wang (2003), Faraoni *et al.* (1999), Rienacker and Hess (2002), Hess (2003)), Figure 1.4, Table 1.3.

When $0 < Pe < 2.162$, the unique attractor is \mathbf{K}_1 . Near $Pe = 0$ (Figure 2.10), the extremely long convergence time reflects the infinite-period bifurcation from the orientationally degenerate nematic equilibrium to the \mathbf{K}_1 limit cycle (Forest and Wang (2003), Forest *et*

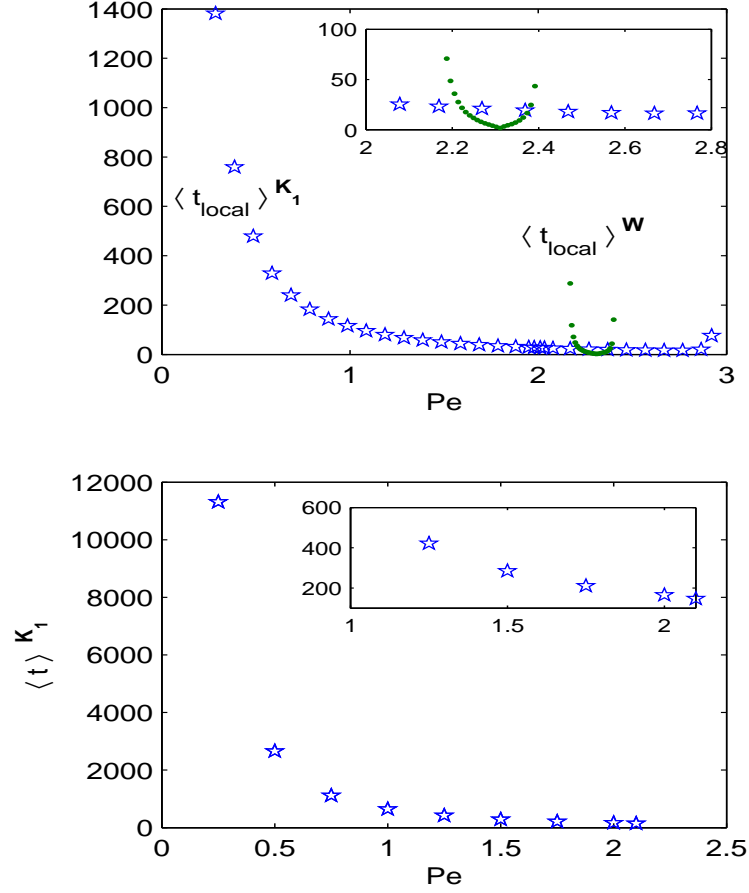


Figure 1.15: Full tensor model statistics for the expected time to converge to the \mathbf{K}_1 attractor of Table 1.3, with $N = 6$.

al. (2003)). The period of \mathbf{K}_1 vs Pe is decreasing, and the expected time $\langle t \rangle_{\mathbf{K}_1}$ likewise decreases vs Pe (Figure 2.10). At $Pe = 1$, $P_{\mathbf{K}_1} = 33.43$, and the expected convergence time is $\langle t \rangle_{\mathbf{K}_1} \approx 641$ relaxation time units. For $Pe \in (1.25, 2.1)$, $\langle t \rangle_{\mathbf{K}_1}$ ranges between 450&150 relaxation time units. As Pe approaches 2.923, the \mathbf{K}_1 attractors disappear through a turning point bifurcation (Forest *et al.* (2003)). We conclude \mathbf{K}_1 attractors in weak shear are rarely (if ever) observed in the laboratory; rather, the transient behavior from the initial data is relevant. The statistical results support private communications by G. Berry, W. Burghardt, and P. Moldenaers, Pittsburgh 2003 Society of Rheology Meeting, who report they have never knowingly observed kayaking monodomains in their laboratories!

For $2.162 < Pe < 2.405$, \mathbf{W} orbits coexist with \mathbf{K}_1 attractors; the \mathbf{W} attractors come and go through an instability transition. Figure 2.10a shows the slowest linearized convergence

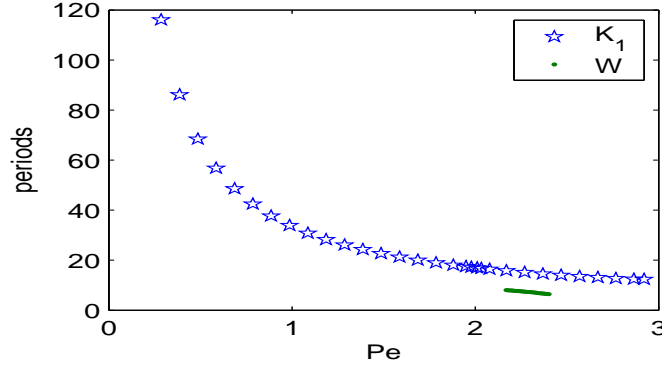


Figure 1.16: Comparison of the limit cycle periods for \mathbf{W} & \mathbf{K}_1 .

rates of \mathbf{K}_1 and \mathbf{W} stable limit cycles, whereas Figure 1.16 compares their periods. Note $P_{\mathbf{W}} \approx \frac{1}{2}P_{\mathbf{K}_1}$ in this bi-stable region, so their “motion” is comparable. In the center of the stable \mathbf{W} regime, $\langle t \rangle_{\mathbf{W}}^{\text{local}} \ll \langle t \rangle_{\mathbf{K}_1}^{\text{local}}$. Because the \mathbf{W} attractor occurs over such a short Pe range, this “stiff” behavior is predicted where a \mathbf{W} limit cycle is weakly then strongly then weakly attractive as Pe slowly rises. Note from Figure 1.4 that the small shear rate window of \mathbf{T}/\mathbf{W} limit cycles for $N = 6$ grows rapidly at higher N , while the complex dynamics region disappear.

Figure 1.17 shows the transient stress signature of a typical \mathbf{W} limit cycle. The difference from the \mathbf{T} attractor, Figure 1.14, is that the stress spikes and not as strong, N_1 only changes sign once per period, and the time-average of N_1 is negative. The apparent viscosity η changes sign once per period, dipping slightly below zero. The order parameter fluctuations are almost 100% during the wagging cycle, indicating dominant molecular elasticity. The order parameter and director dynamics are in phase, and do not reflect the secondary spikes in N_1 and η .

Figure 1.18 repeats Figure 1.17 for the co-stable kayaking attractor. The signature of N_1 is remarkably similar for tumbling and kayaking; however, the apparent viscosity eventually lose the secondary oscillation or “double dip” per period once the limit cycle is reached. The order parameter oscillates in phase with the major director, though with smaller amplitude variations than the \mathbf{W} attractor. The in-plane angle of the major director continues to rotate, while the out-of-plane angle oscillates over a finite range typical of the kayaking image of Larson and Ottinger (1991).

These sample orbits also illustrate the relatively large expected time for convergence to \mathbf{K}_1

vs \mathbf{W} orbits: $\langle t \rangle_{\mathbf{K}_1} \approx 10 \langle t \rangle_{\mathbf{W}}$, or about 100 relaxation time units. The period average of N_1 also has opposite sign: $\langle N_1 \rangle_{\mathbf{W}} < 0$, whereas $\langle N_1 \rangle_{\mathbf{K}_1} > 0$. We return to this bi-stable parameter region in the next section.

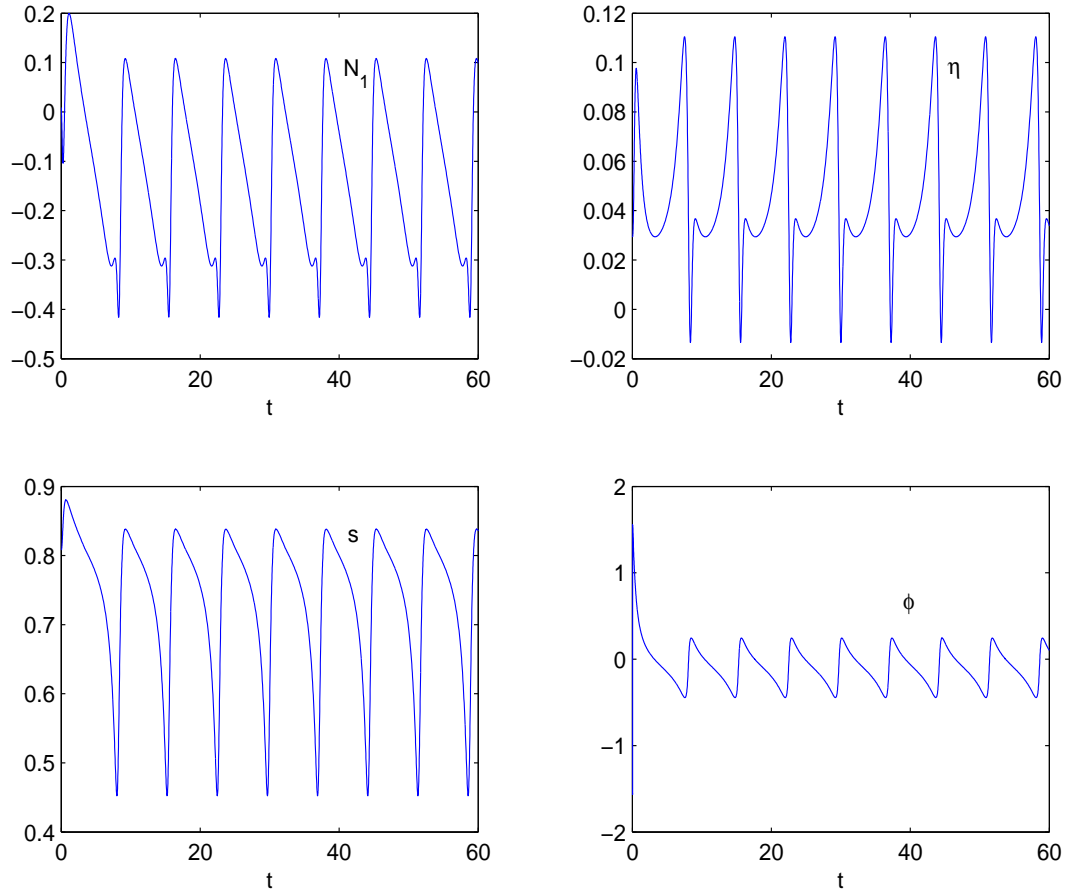


Figure 1.17: First normal stress difference N_1 (top left), apparent viscosity η (top right) versus time, for a randomly chosen orbit that converges to the \mathbf{W} attractor of Table 1.3, with Peclet number $Pe = 2.3$, nematic concentration $N = 6$, rodlike aspect ratio $r = 3$ ($a = 0.8$). $\langle N_1 \rangle \approx -1.1 \times 10^{-1}$, $\langle N_2 \rangle \approx 3.5 \times 10^{-2}$ (not shown), $\langle \eta \rangle \approx 4 \times 10^{-2}$ over the period of \mathbf{W} , with strong fluctuations by factors of 3 for N_1 and 3 for η . The corresponding order parameter and in-plane director dynamics are shown bottom left and right. For discotic aspect ratio $r = \frac{1}{3}$ ($a = -0.8$) with all other parameters held constant, $\langle N_1 \rangle$ and $\langle \eta \rangle$ are nearly identical, while $\langle N_2 \rangle$ increases by a factor of about 2.

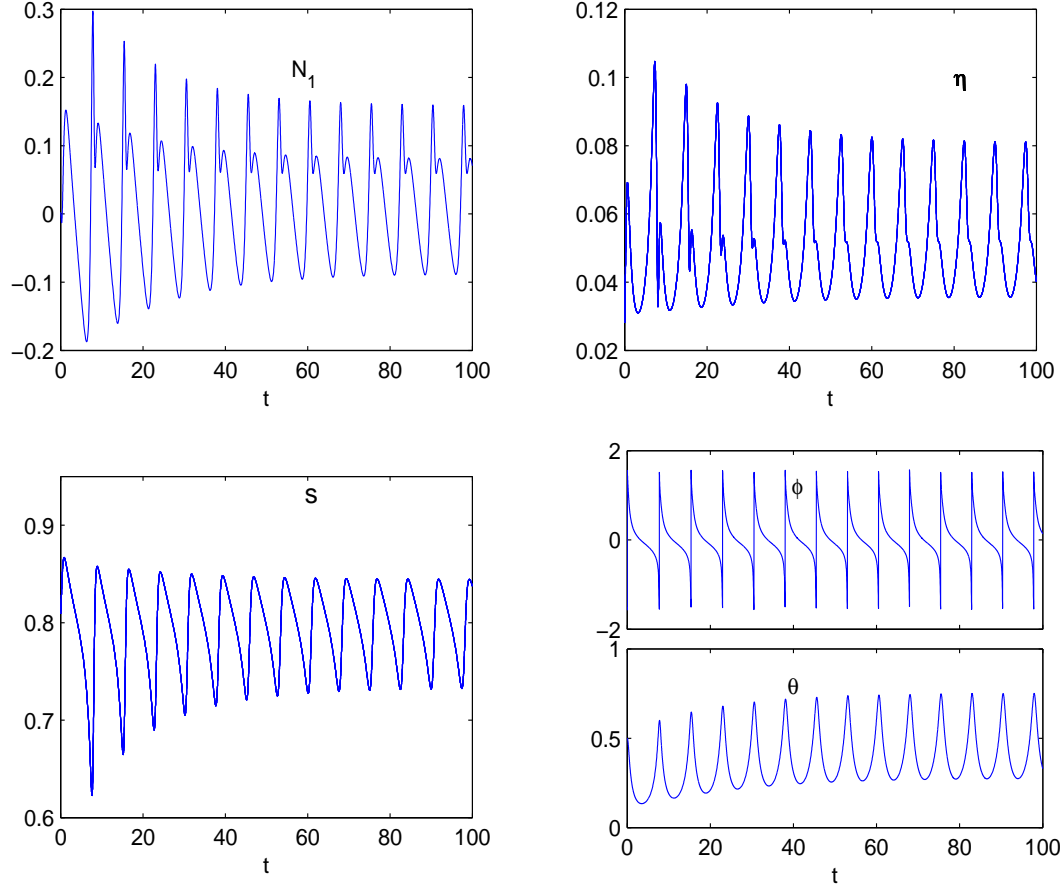


Figure 1.18: First normal stress difference N_1 (top left), apparent viscosity η (top right) versus time, for a randomly chosen orbit that converges to the \mathbf{K}_1 attractor of Table 1.3, with Peclet number $Pe = 2.3$, nematic concentration $N = 6$, rodlike aspect ratio $r = 3$ ($a = 0.8$). $\langle N_1 \rangle \approx 4 \times 10^{-2}$, $\langle N_2 \rangle \approx -3 \times 10^{-2}$ (not shown), $\langle \eta \rangle \approx 5 \times 10^{-2}$ over the period of \mathbf{K}_1 , with strong fluctuations by factors of 5 for N_1 and 2 for η . For discotic aspect ratio $r = \frac{1}{3}$ ($a = -0.8$), $\langle N_1 \rangle$ and $\langle \eta \rangle$ are nearly the same, while $\langle N_2 \rangle$ decreases by a factor of 10.

1.6.4 Domains of attraction in bi-stable and tri-stable regions

Figures 1.3, 1.4 and Tables 1.2, 1.3 indicate that sheared nematic polymers have significant (shear rate, concentration) regimes with multiple attracting states. Furthermore, since typical experimental samples consist of many monodomains, the measured rheology will be a statistical average over the distribution of attractors. In this section, we compute this distribution for selected parameter regimes with bi-stable and tri-stable monodomain modes.

In-plane bi-stable statistics

The first example is the bi-stable **LR**+**T** or **LR**+**W** regime of Figure 1.3, Table 1.3 and Table 1.4, which is consistent with the kinetic phase diagram of Forest *et al.* (2003). By contrast, the full tensor diagram (Figure 1.4) has spurious, closure-induced, out-of-plane **LR** instabilities. Thus, the in-plane model is actually a more faithful approximation of kinetic theory for this bi-stable regime. Grosso *et al.* (2003) recently used kinetic simulations in the **LR**+**W** bi-stable regime to compare with experimental data for a distribution of **LR** and **W** attractors. They posited a (90%**W**, 10%**LR**) distribution, presumably from statistics. Here we compute the statistical distribution as follows. Because the model is confined in-plane, the nematic equilibrium initial data (1.31) is restricted to in-plane with major director in the plane or along the vorticity axis. The dynamics of the in-plane model for this initial data is trivial: all in-plane data converge to the **T** or **W** attractor. Therefore, we completely randomize the initial data set to any Q^{i-p} of the form:

$$Q = s(\mathbf{nn} - \frac{\mathbf{I}}{3}) + \beta(\mathbf{n}^\perp \mathbf{n}^\perp - \frac{\mathbf{I}}{3}) \quad (1.38)$$

where $s = d_1 - d_3$, and $\beta = d_2 - d_3$, $d_i, i = 1, 2, 3$ are the eigenvalues of Q , with $\mathbf{n} = (\cos \phi_0, \sin \phi_0, 0)$. Then we choose 1000 random data, parametrized by (s, β, ϕ_0) , and count the percentage of data that converge to each attractor. This calculation literally gives the relative measure of the domains of attraction of **LR** and **T/W** attractors over the entire 3 dimensional phase space, which we call the likelihood of resonating each attractor. The same method is used for the **FA-LR** bi-stable steady parameter regime of Table 1.3.

Case 1. For fixed concentration $N = 4$, we vary Pe in the **FA** and **LR** bi-stable region. Table 1.4 shows the distribution of arbitrary initial data (1.38) that converges to each attractor. Note that as Pe decreases, the likelihood of **LR** states grows.

Table 1.4: Statistical distribution of attractors in the **FA** and **LR** bi-stable regime for $N = 4$ and three different Pe .

Pe	1	0.5	0.1
% LR	27	39	50
% FA	73	61	50

Case 2. To compare with kinetic results of Grosso *et al.* (2003), we choose $N = 6.66$ in Figure 1.3, which is characterized by the co-existence of a stable **T/W** limit cycle with a stable **LR** solution. Table 1.5 shows the distribution of attractors. In the bi-stable **W-LR** regime, the likelihood of **LR** varies between 15% and 32%, but then jumps to 41% likelihood when bi-stable with **T**.

Table 1.5: Statistical distribution of attractors in the **T/W** and **LR** bi-stable regime, for $N = 6.66$ and five different Pe .

Pe	5	3	2.66	2.3	1
% LR	15	27	30	32	41
% T	0	0	0	0	59
% W	85	73	70	68	0

Out-of-plane bi-stable and tri-stable statistics

From Figure 1.4 and Table 1.3, we have a bi-stable **K₁** and **W** regime. Whenever the tilted kayaking limit cycle **K₂** is stable, it always has its bi-stable twin, on the other side of the shearing plane. We also have a tri-stable region of **K₁** and **K₂^{+,−}**. We now measure the statistical likelihood of converging to each attractor from nematic equilibrium data.

Case 1. When $Pe = 2.3$ and $N = 6$, the **K₁** and **W** bi-stable regime, Figure 1.19 shows the statistical likelihood of convergence to **K₁** and **W** as the initial nematic director at rest is sampled across the sphere.

- If the initial directors **n** have polar angles $\theta_0 \geq 85.5^\circ$, then all the data converge to the

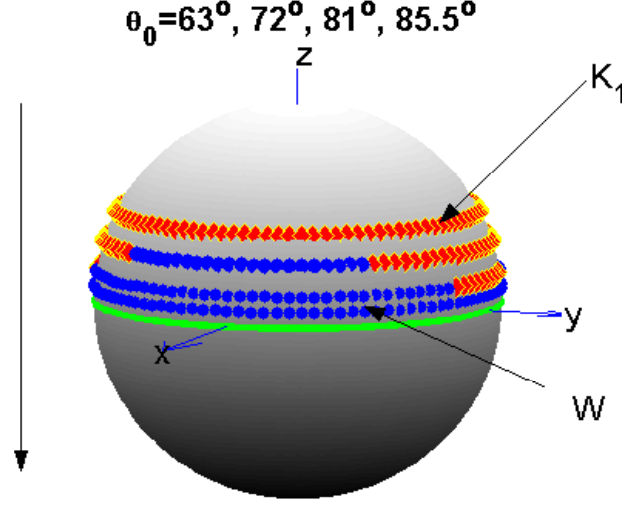


Figure 1.19: Statistics of the likelihood of convergence to attractors from the nematic rest state at a fixed concentration $N = 6$, for the \mathbf{K}_1 and \mathbf{W} bi-stable region with $Pe = 2.3$. The lighter points represent initial director configuration that will converge to \mathbf{K}_1 , whereas the black points converge to \mathbf{W} .

in-plane \mathbf{W} attractor. Thus, initial director orientations that are sufficiently close to the shearing plane are attracted to the \mathbf{W} attractor. This has important consequences since plate preparations in Couette cells can strongly prejudice the director orientation of the rest state.

- For initial directors \mathbf{n} which have polar angles $\theta_0 < 63^\circ$, i.e., tilted sufficiently far from the shearing plane, all converge to the out-of-plane \mathbf{K}_1 attractor. Again, this has important experimental implications.
- Between these two “latitudes”, there is no clear boundary for each attracting set. When θ_0 ranges between 81° and 68.4° , we find initial data with different in-plane tilt angles ϕ_0 converge to different attractors, shown in Table 1.6.

Table 1.6: Likelihood statistics for $N = 6$, $Pe = 2.3$, in the \mathbf{W} and \mathbf{LR} bi-stable regime, with different initial polar angles. The degree of out-of-plane tilt is seen to control the likelihood of \mathbf{W} vs \mathbf{LR} attractors.

θ_0	81°	76°	72°	68.4°
% \mathbf{K}_1	20	36	56	80
% \mathbf{W}	80	64	44	20

- As Pe varies over the range $(2.162, 2.405)$, which is the region of coexistence of \mathbf{K}_1 and \mathbf{W} for $N = 6$, the likelihood of convergence to \mathbf{K}_1 vs \mathbf{W} varies, shown in Table 1.7.

Table 1.7: Statistical distribution of bi-stable attractors for $N = 6$, with different Pe in the \mathbf{W} and \mathbf{K}_1 bi-stable regime.

Pe	2.2	2.3	2.4
% \mathbf{K}_1	92.5	83.2	77
% \mathbf{W}	7.5	16.8	23

Combining these results with Section 2.4, we find that while the expected time to converge to \mathbf{W} attractors $\langle t \rangle_{\mathbf{W}}$ is much shorter than $\langle t \rangle_{\mathbf{K}_1}$, the attracting set of \mathbf{K}_1 is larger than that of \mathbf{W} , if the initial data consists of randomly oriented nematic rest states. However, initial pre-alignment of monodomains can strongly bias the distribution in favor of in-plane \mathbf{W} attractors!

Figure 1.20 shows the time series of averaged N_1, N_2 and η over 1000 random sample orbits, and the average values of N_1, N_2 and η are exactly the weighted average (83% of \mathbf{K}_1 , 17% of \mathbf{W}) of \mathbf{K}_1 and \mathbf{W} . $\langle N_1 \rangle \approx 7 \times 10^{-3}$ is almost negligible (Grosso *et al.* (2003)).

Case 2. Figure 1.21 shows the statistics when we increase Pe to 2.5, the $\mathbf{K}_1, \mathbf{K}_2^{+,-}$ tri-stable regime.

- If the initial directors \mathbf{n} have polar angles $\theta_0 \geq 81^\circ$, all data converge to the \mathbf{K}_2 attractor. Initial directors that are sufficiently close to the shearing plane are attracted to one of the \mathbf{K}_2 orbits!
- Initial directors with polar angles $\theta_0 < 49.5^\circ$, i.e. tilted toward the vorticity axis, all converge to the \mathbf{K}_1 limit cycle.
- Table 1.8 and Figure 1.21 show that the likelihood of \mathbf{K}_1 vs $\mathbf{K}_2^{+,-}$ varies dramatically when the initial polar angle θ_0 ranges between 81° and 49.5° .

Remark: Through explicit solution of the model equations, we compare properties of \mathbf{K}_1 vs $\mathbf{K}_2^{+,-}$ attractors. We find the out-of-plane components Q_{xz} and Q_{yz} of \mathbf{K}_2 attractors are always less than that of \mathbf{K}_1 limit cycles. Thus, it is reasonable to believe that if the initial

Table 1.8: Attractor likelihood distribution for $N = 6$, $Pe = 2.5$, which is in the \mathbf{K}_1 and $\mathbf{K}_2^{+,-}$ tri-stable regime, with different initial polar angles.

θ_0	76.5°	72°	63°	68.4°
% \mathbf{K}_1	16	26	48	92
% $\mathbf{K}_2^{+,-}$	84	74	52	8

director \mathbf{n} is near the shearing plane, it is more likely to converge to either of the \mathbf{K}_2 states, while if the initial director is near the vorticity axis, then the data are attracted to the \mathbf{K}_1 state.

Table 1.9 shows that as Pe increases in the interval $(2.405, 2.546)$, the likelihood of \mathbf{K}_1 decreases to about 70%. Overall however, the domain of attraction \mathbf{K}_1 is greater than the $\mathbf{K}_2^{+,-}$ pair.

Table 1.9: Likelihood statistics for $N = 6$ and different Pe in the \mathbf{K}_1 and $\mathbf{K}_2^{+,-}$ tri-stable regime

Pe	2.45	2.5	2.53
% \mathbf{K}_1	74.1	71.4	70
% $\mathbf{K}_2^{+,-}$	25.9	29.6	30

Case 3. We increase Pe to 3.5, where the \mathbf{K}_1 orbits have disappeared, Table 1.4, with only bi-stable $\mathbf{K}_2^{+,-}$. Figure 1.22 shows that \mathbf{K}_2^+ and \mathbf{K}_2^- have the same strength at each latitude, the data will converge to each attractor with probability 1/2. They have the same strength and size. The expected time for a random initial condition to converge to $\mathbf{K}_2^{+,-}$ is about 200 relaxation time units.

1.6.5 Conclusion

We have provided a summary of the statistical properties of nematic polymers monodomains in simple shear. These data inform the expected time for steady states and limit cycles to appear when shear experiments begin from rest, as well as the likelihood of convergence to each attracting state when there are two or three stable monodomains. The transient rheology of each attractor is also shown.

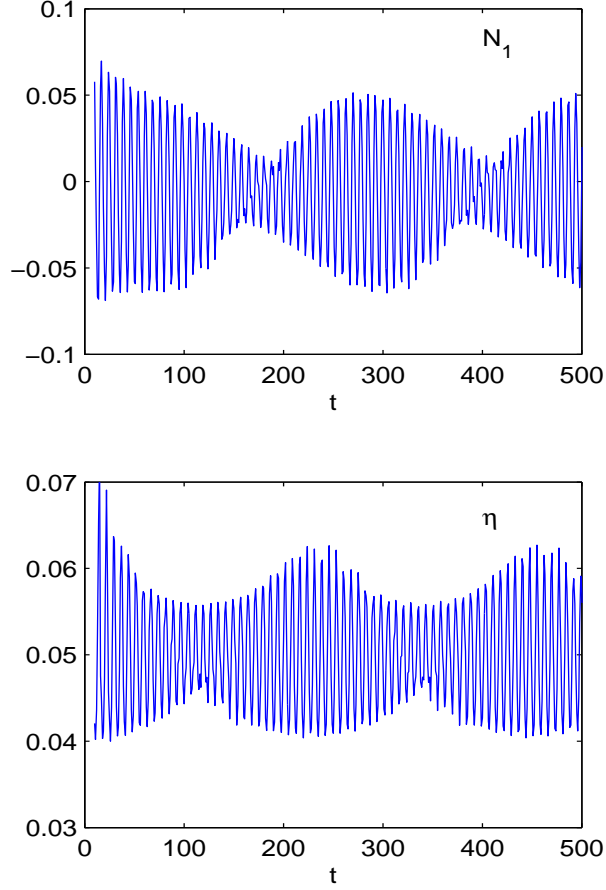


Figure 1.20: First normal stress difference N_1 (top), apparent viscosity η (bottom) versus time, averaged over 1000 sample orbits in the bi-stable region of Table 1.3, with Peclet number $Pe = 2.3$, nematic concentration $N = 6$, rodlike aspect ratio $r = 3$ ($a = 0.8$). $\langle N_1 \rangle \approx -7 \times 10^{-3}$, $\langle N_2 \rangle \approx 1.5 \times 10^{-2}$ (not shown), $\langle \eta \rangle \approx 5 \times 10^{-2}$, with strong fluctuations by factors of 6 for N_1 and 1.3 for η . The results for platelets ($a = -0.8$) are nearly identical for $\langle N_1 \rangle$ and $\langle \eta \rangle$, whereas $\langle N_2 \rangle$ is nearly zero, but negative.

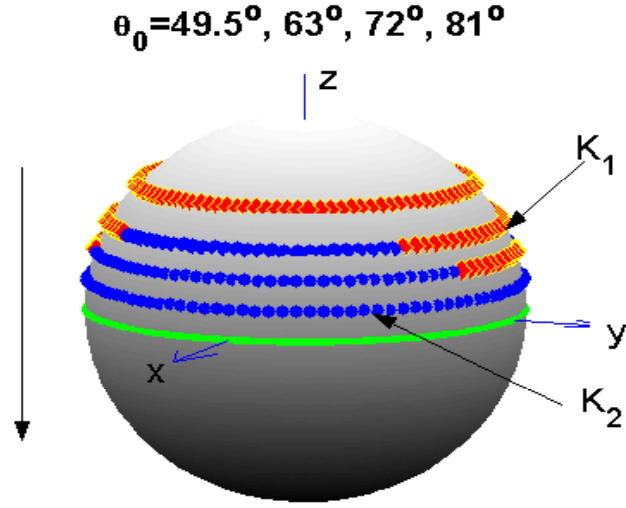


Figure 1.21: Statistics in tri-stable $(\mathbf{K}_1, \mathbf{K}_2^{+, -})$ region with $Pe=2.5$. The lighter gray points on the sphere are the initial director orientations that converge to \mathbf{K}_1 , the black points converge to $\mathbf{K}_2^{+, -}$.

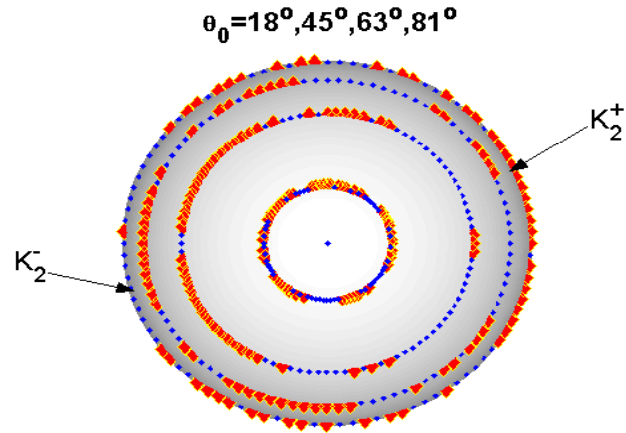


Figure 1.22: Statistics in $\mathbf{K}_2^{+, -}$ bi-stable region with $Pe=3.5$. The light gray points are the initial director orientations that converge to \mathbf{K}_2^+ , the black points converge to \mathbf{K}_2^- . Note this view is looking down from the vorticity axis at the center.

Chapter 2

Effective Conductivity Properties of Nematic Polymer Nano-Composites

2.1 Introduction

Nano-elements with high-contrast properties are combined at low (0.1%-5%) volume fractions with traditional polymeric materials to enhance a diverse set of targeted properties (Vaia (2002)). Notable examples are high electrical conductivity & strength of carbon nanotubes (CNTs) and barrier properties of nano-clay platelets. Current numerical algorithms for composite properties (Lusti *et al.* (2002)) impose either a random distribution or perfect alignment of the nano-rods or nano-platelets. These opposite extremes of orientational probability distribution functions (PDF's) are assumed not because of the inability to handle real molecular distributions, rather because of lack of data from experiments or model simulations. Indeed it is a monumental challenge to infer molecular orientational distributions from experimental methods, although important features of the second moment of the PDF are routinely measured with light scattering methods (Burghardt (1998)). Our goal here is to use kinetic and mesoscopic models to generate the PDF or its moments, which then can be linked to composite property theory and numerical algorithms. This strategy becomes more compelling when the kinetic theory of Doi and Hess (Doi (1981)-Kroger (2004)) or mesoscopic models have been separately benchmarked with experimental data on the flow-induced liquid phase of the composite. For this chapter we assume a rapid quench from the liquid to solid phase which maintains the orientational distribution of the nano-inclusions. We also suppress the effects of the inclusion-matrix interphase. The current predictions, when compared with laboratory measurements, provide an estimate of interphase contributions to effective conductivity based

on volume-averaged effects. The separate, though related, effects due to percolation of the nano-elements is not captured by volume averaging. Strong disparities between the present predictions and experiments would suggest a dominant influence of percolation relative to volume-averaging.

The composite properties, no matter whether they are electrical conductivity (the example chosen here), thermal conductivity, gas or liquid permeabilities, or elastic moduli, require an appropriate average, e.g. over the nano-element electrical conductivity σ_{nano} with volume fraction θ_2 and the polymer conductivity σ_{poly} with volume fraction $(1 - \theta_2)$. The typically strong contrast $\sigma_{nano}/\sigma_{poly} \gg 1$ (or $\sigma_{nano}/\sigma_{poly} \ll 1$ which arise for thermal insulating composites) by itself is not sufficient to achieve the enhancements; the high degree of anisotropy of the nano-inclusion is equally critical. This enabling geometric effect comes at a price, however, introducing complexity into the orientational molecular distribution at rest and in processing flows.

High aspect ratio molecular inclusions naturally are isotropic (randomly oriented) below a critical volume fraction, θ_2^* , but then spontaneously order above θ_2^* , the isotropic-nematic phase transition. Only as $\theta_2 \rightarrow 1$ is perfect alignment achieved, a limit which is never approached in nano-composites. The equilibrium orientational distribution function versus θ_2 is numerically available from the Doi-Hess kinetic theory with an excluded-volume intermolecular potential, e.g., of Onsager Eq.(1.14) or Maier-Saupe type Eq. (1.15) (Faraoni *et al.* (1999), Forest *et al.* (2004), Larson and Ottinger (1991)). For this chapter, our goal is to derive exact formulas for the effective electrical conductivity tensor, at rest and in weak shear flows. This choice is made for two purposes: 1) to illustrate the approach for exactly solvable conditions where the methodology and results become transparent; and 2) to determine exact scaling properties of the effective conductivity tensor versus molecular and flow parameters, albeit in special limits or with mesoscopic closure approximations.

First, we implement tensor formulas for the kinetic probability density function (1.17)(PDF) at dilute concentrations, or the second moment of the PDF derived from mesoscopic models (1.22) at ordered (nematic) concentrations, and substitute these into the low volume fraction expansion of the effective electrical conductivity tensor. We calculate the *effective electrical*

conductivity tensor, Σ^e , versus volume fraction θ_2 , allowing a property comparison of the quiescent isotropic & nematic phases.

Second, nano-composites are flow-processed, which deforms the distribution at all concentrations θ_2 . We use our recent analytical formulas for monodomain, shear-induced PDFs, at dilute concentrations (Forest *et al.* (2004)), and for second moments of the PDF at nematic concentrations (Forest *et al.* (2003)), in the weak shear limit. From these explicit formulas, we quantify the anisotropy and principal values of Σ^e , and thereby predict nano-composite conductivity enhancement versus concentration at rest and in weak shear flow, Section 2.5.

For steady monodomains, the conductivity tensor is constant, for which we exhibit *parametric variations* in \mathcal{E}_{max} versus shear rates and concentrations. For oscillatory monodomains, we consider representative tumbling, kayaking and chaotic attractors and show the corresponding *dynamic ranges* of \mathcal{E}_{max} and $\mathcal{E}_1 - \mathcal{E}_2$, Section 2.6.

2.2 Formulation of the nano-composite effective conductivity problem

Consider conduction in a three-dimensional media, governed by the constitutive equations

$$\vec{J}(x) = \Sigma(x)\vec{E}(x), \quad \nabla \cdot \vec{J} = 0, \quad \nabla \times \vec{E} = 0 \quad (2.1)$$

where $\vec{J}(x)$ is the current field, $\vec{E}(x) = \nabla\phi$ is the electric field, ϕ is the electric potential, and $\Sigma(x)$ is the conductivity tensor of the medium. The **effective conductivity** Σ^e provides the constitutive relation between the average current $\langle \vec{J} \rangle$ and average electric field $\langle \vec{E} \rangle$, i.e.

$$\langle \vec{J} \rangle = \Sigma^e \langle \vec{E} \rangle. \quad (2.2)$$

Here $\langle \vec{J} \rangle$ and $\langle \vec{E} \rangle$ are the volume average of the current and electric field over the polymer suspension. Since the system is ergodic, volume average is equivalent to orientational average. There are two inherent difficulties in Σ^e : anisotropy due to orientational molecular ordering, and spatial heterogeneity due to length scale distortions in the orientational distribution. For

this chapter, we characterize the anisotropy of Σ^e for monodomains of nematic polymer nanocomposites (PNCs), but our framework applies to heterogeneous composites.

2.2.1 Nano-composite microstructure

We consider uniform suspensions of ellipsoidal molecular inclusions with electrical conductivity σ_2 and volume fraction θ_2 in a matrix of electrical conductivity σ_1 . Later we restrict to spheroids, the axi-symmetric case, which is the only class of molecules for which Doi-Hess-type hydrodynamic theory is available.

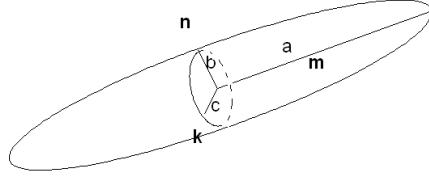


Figure 2.1: The illustration of spheroidal rods with semi-axes lengths $a > b = c$, with respect to axes \mathbf{m} , \mathbf{n} , \mathbf{k} , respectively.

All ellipsoids are assumed to have the same geometry: a , b , c are the three semi-axes, with $a > b = c$ for spheroidal rods and $a = b > c$ for spheroidal platelets. They orient due to excluded-volume interactions and flow according to a probability distribution that is the central object of the Doi-Hess kinetic theory. The theory incorporates the aspect ratio $r = a/b \gg 1$ (rods); $r = c/a \ll 1$ (platelets) in the combination $\frac{r^2 - 1}{r^2 + 1}$.

2.2.2 The effective conductivity tensor $\Sigma_{\theta_2}^e$ for isotropic ellipsoids

The effective conductivity tensor $\Sigma_{\theta_2}^e$, where we attach the nano-inclusion volume fraction θ_2 as a subscript, can be computed by a Taylor expansion in the low volume fraction limit, $\theta_2 \ll 1$ (cf. Milton (2002)):

$$\Sigma_{\theta_2}^e = \sigma_1 \mathbf{I} + \theta_2 (\sigma_2 - \sigma_1) \mathbf{P} + O(\theta_2^2), \quad (2.3)$$

where

$$\mathbf{P} = \int_{S^2} \mathbf{E}(\mathbf{m}) f(\mathbf{m}) d\mathbf{m} \quad (2.4)$$

is called the orientation-averaged polarization tensor, $\mathbf{E}(\mathbf{m})$ is the polarization tensor, defined below, and $f(\mathbf{m})$ is the orientational probability distribution function of the inclusions. \mathbf{I} is the 3 by 3 identity matrix. From (2.3), the key object to quantify is \mathbf{P} , which requires knowledge of two ingredients: $\mathbf{E}(\mathbf{m})$ is a geometric tensor specified by the nano-inclusion geometry, whereas $f(\mathbf{m})$ is the fundamental object of the Smoluchowski equation of Doi-Hess kinetic theory for quiescent or flowing nematic polymers.

The polarization tensor $\mathbf{E}(\mathbf{m})$ can be computed explicitly from three scalar depolarization factors: $L_a, L_b, L_c \geq 0$ (cf. Stratton (1941)):

$$\begin{aligned} L_a &= \frac{abc}{2} \int_0^\infty \frac{ds}{(s+a^2)\sqrt{(s+a^2)(s+b^2)(s+c^2)}} \\ L_b &= \frac{abc}{2} \int_0^\infty \frac{ds}{(s+b^2)\sqrt{(s+a^2)(s+b^2)(s+c^2)}} \\ L_c &= \frac{abc}{2} \int_0^\infty \frac{ds}{(s+c^2)\sqrt{(s+a^2)(s+b^2)(s+c^2)}} \\ L_a + L_b + L_c &= 1, \end{aligned} \quad (2.5)$$

$$\mathbf{E}(\mathbf{m}) = \left[\left(1 + \left(\frac{\sigma_2 - \sigma_1}{\sigma_1} \right) L_a \right) \mathbf{m}\mathbf{m} + \left(1 + \left(\frac{\sigma_2 - \sigma_1}{\sigma_1} \right) L_b \right) \mathbf{n}\mathbf{n} + \left(1 + \left(\frac{\sigma_2 - \sigma_1}{\sigma_1} \right) L_c \right) \mathbf{k}\mathbf{k} \right]^{-1}, \quad (2.6)$$

where \mathbf{m} is the unit vector along the long axis of length a , \mathbf{n} is the unit vector along the axis of length b , \mathbf{k} is the unit vector along the axis of length c ; refer to Figure 2.1. All that remains is an explicit characterization of $f(\mathbf{m})$ (which we now develop in several limiting cases, where analytical formulas are possible), and then finally an analysis of the integral (2.4). In more generality, numerical data for $f(\mathbf{m})$ can be implemented in this framework, which we defer to a sequel.

2.2.3 The effective conductivity tensor $\Sigma_{\theta_2}^e$ for anisotropic ellipsoids

For future reference, we give the general effective conductivity tensor for isotropic matrix and anisotropic nano-inclusion. If the principal axes of the ellipsoid coincide with the principal

the the conductivity tensor, then

$$\Sigma_2 = \begin{pmatrix} \sigma_{2,a} & 0 & 0 \\ 0 & \sigma_{2,b} & 0 \\ 0 & 0 & \sigma_{2,c} \end{pmatrix}, \quad (2.7)$$

the second subscript represent along the principal axes a, b, c , then the effective conductivity of the composite average over the orientations in the ensemble is:

$$\Sigma_{\theta_2}^e = \Sigma_1 + \theta_2(\Sigma_2 - \Sigma_1) \int_{S^2} (\mathbf{I} + (\Sigma_2 - \Sigma_1)\Sigma_1^{-1}L)^{-1} f(\mathbf{m}) d\mathbf{m} + O(\theta_2^2), \quad (2.8)$$

where $\Sigma_1 = \sigma_1 \mathbf{I}$ and

$$L = \begin{pmatrix} L_a & 0 & 0 \\ 0 & L_b & 0 \\ 0 & 0 & L_c \end{pmatrix}. \quad (2.9)$$

In the case of spheroids, i.e. $L_b = L_c = (1 - L_a)/2$, and $\sigma_{2,a} > \sigma_{2,b} = \sigma_{2,c}$, so that a is the long axis, the conductivity is largest along the axial direction, and the conductivity in the transverse direction $\sigma_{2,b}, \sigma_{2,c}$ is less.

2.2.4 The effective conductivity tensors $\Sigma_{\theta_2}^e$ for isotropic coated ellipsoids

Generally, in a nano-composite, the contact between the nano-inclusion and viscous solvent is not perfect, an interphase always exists. To resolve the reality, we can make an assumption about the inclusion, which consists of coated ellipsoid, whose inner core has the property of nano-inclusion, the outer layer is usually unknown. Under this circumstance, an inverse problem is needed to be study to get the property of the interphase.

Consider the cell problem, one coated particle embedded in a infinite medium. To solve the Laplace equations, we need to consider the imposition continuities of the potential and normal fluxes across the inner and outer bounding surface. The effective conductivity tensor is given by the series expansion of the volume of the coated ellipsoid:

$$\Sigma^e = \sigma_1 \mathbf{I} + \theta_c \sigma_1 \langle E_1 \rangle + O(\theta_c^2) \quad (2.10)$$

$$E_{1,ii} = \frac{(\sigma_{sh} - \sigma_1)(\sigma_{sh} + (\sigma_2 - \sigma_{sh})(L_i^2 - fL_i^{sh})) + f\sigma_{sh}(\sigma_2 - \sigma_{sh})}{(\sigma_{sh} + (\sigma_2 - \sigma_{sh})(L_i^2 - fL_i^{sh}))(\sigma_1 + (\sigma_{sh} - \sigma_1)L_i^{sh}) + fL_i^{sh}(\sigma_2 - \sigma_{sh})\sigma_{sh}} \quad (2.11)$$

where $f = abc/(ABC)$, and

$$\begin{aligned} L_i^{sh} &= \frac{ABC}{2} \int_0^\infty \frac{ds}{(s+i^2)\sqrt{(s+A^2)(s+B^2)(s+C^2)}}, \quad i = A, B, C \\ L_i^2 &= \frac{abc}{2} \int_0^\infty \frac{ds}{(s+i^2)\sqrt{(s+a^2)(s+b^2)(s+C^2)}}, \quad i = a, b, c \end{aligned} \quad (2.12)$$

$A^2 = a^2 + t, B^2 = b^2 + t, C^2 = c^2 + t, t$ is related to the thickness of the shell.

2.3 Nano-composite properties of nematic polymer monodomains

We proceed to compute the effective conductivity tensor $\Sigma_{\theta_2}^e$ for low volume fraction spheroidal suspensions in several limiting regimes:

- the quiescent isotropic phase of dilute random suspensions vs. concentration (N) and molecular aspect ratio (r);
- the nematic equilibrium phase vs. N and r using second-moment approximate descriptions of the PDF;
- the flow-induced PDF in simple shear at low (isotropic) quiescent concentrations; and
- mesoscopic approximations of the PDF for weak shear-induced nematic phases.

Our first result is to derive an explicit formula for the polarization tensor \mathbf{P} , equation (2.4), and thereby the effective conductivity tensor $\Sigma_{\theta_2}^e$, equation (2.3). This formula is special for spheroidal rod-like (or platelet) nano-inclusions, yet general for any orientational PDF $f(\mathbf{m})$ of the inclusions.

For *rod-like spheroidal nano-inclusions*, the depolarization factors become $L_b = L_c = (1 - L_a)/2$ and $\mathbf{mm} + \mathbf{nn} + \mathbf{kk} = \mathbf{I}$, from which we can explicitly express the polarization tensor \mathbf{E} as a linear combination of the isotropic tensor \mathbf{I} and the quadratic (dyadic) product \mathbf{mm} :

$$\mathbf{E}(\mathbf{m}) = \left[\left(1 + \left(\frac{\sigma_2 - \sigma_1}{\sigma_1} \right) L_a \right) \mathbf{mm} + \left(1 + \left(\frac{\sigma_2 - \sigma_1}{\sigma_1} \right) \frac{1 - L_a}{2} \right) (\mathbf{I} - \mathbf{mm}) \right]^{-1}. \quad (2.13)$$

We now observe that the inverse of a linear combination of \mathbf{I} and \mathbf{mm} is itself a linear combination of \mathbf{I} and \mathbf{mm} . Thus, for spheroids, equation (2.13) is explicitly invertible, and we deduce

$$\mathbf{E}(\mathbf{m}) = \frac{1}{1 + \frac{\sigma_2 - \sigma_1}{2\sigma_1}(1 - L_a)} \left(\mathbf{I} + \left[\frac{\frac{\sigma_2 - \sigma_1}{2\sigma_1} - \frac{3}{2} \frac{\sigma_2 - \sigma_1}{\sigma_1} L_a}{1 + \frac{\sigma_2 - \sigma_1}{\sigma_1} L_a} \right] \mathbf{mm} \right), \quad (2.14)$$

where the spheroidal depolarization factor L_a is explicitly integrable (graphed in Figure 2.2)

$$L_a = \frac{1 - \epsilon^2}{\epsilon^2} \left\{ \frac{1}{2\epsilon} \ln \left(\frac{1 + \epsilon}{1 - \epsilon} \right) - 1 \right\}, \epsilon = \sqrt{1 - (b/a)^2}. \quad (2.15)$$

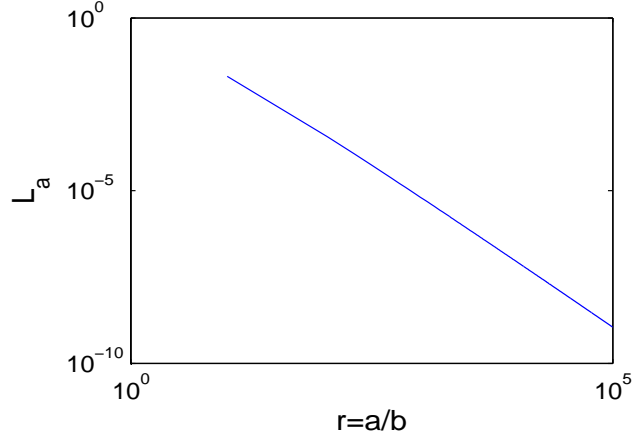


Figure 2.2: Depolarization factor L_a versus aspect ratio r .

The explicit form (2.14) of $\mathbf{E}(\mathbf{m})$ has strong consequences. First, even though $f(\mathbf{m})$ generically has an infinite spherical harmonic expansion, by orthogonality relations of spherical harmonics and the linear form (2.13), *only the second moments of $f(\mathbf{m})$ contribute to \mathbf{P}* , equation (2.4). This result is valid for any distribution $f(\mathbf{m})$ of monodisperse spheroids, no matter how $f(\mathbf{m})$ is generated, and furthermore, for both homogeneous monodomains as well as heterogeneous dispersions where $f(\mathbf{m}, \mathbf{x})$ varies in space.

Performing the integral (2.4) by virtue of (2.14), we deduce an explicit formula for \mathbf{P} directly in terms of the second-moment $\mathbf{M}(f)$ of the orientational probability density f :

$$\mathbf{P} = \int_{\|\mathbf{m}\|=1} \mathbf{E}(\mathbf{m})f(\mathbf{m})d\mathbf{m} = \frac{1}{1 + \frac{\sigma_2 - \sigma_1}{2\sigma_1}(1 - L_a)} \left(\mathbf{I} + \frac{\frac{\sigma_2 - \sigma_1}{2\sigma_1} - \frac{3}{2}\frac{\sigma_2 - \sigma_1}{\sigma_1}L_a}{1 + \frac{\sigma_2 - \sigma_1}{\sigma_1}L_a} \mathbf{M} \right). \quad (2.16)$$

Combining (2.15) and (2.16) gives the explicit connection between the second moment of the orientational distribution and the overall electrical properties of the nano-composite, and the central result of this chapter:

The effective electrical conductivity tensor $\Sigma_{\theta_2}^e$ of the composite is given by:

$$\begin{aligned} \Sigma_{\theta_2}^e = & \Sigma_0 + \sigma_1 \theta_2 (\sigma_2 - \sigma_1) \left(\frac{2}{\sigma_2 + \sigma_1 - (\sigma_2 - \sigma_1)L_a} \mathbf{I} \right. \\ & \left. + \frac{(\sigma_2 - \sigma_1)(1 - 3L_a)}{((\sigma_1 + \sigma_2) - (\sigma_2 - \sigma_1)L_a)(\sigma_1 + (\sigma_2 - \sigma_1)L_a)} \mathbf{M}(f) \right) + O(\theta_2^2). \end{aligned} \quad (2.17)$$

In general, we define the nano-composite *electrical conductivity enhancement* in terms of the difference between $\Sigma_{\theta_2}^e$ at volume fraction $\theta_2 > 0$ and $\Sigma_0 = \sigma_1 \mathbf{I}$, the isotropic conductivity of the pure matrix with zero volume fraction $\theta_2 = 0$. We shall focus on the principal value(s) of $\Sigma_{\theta_2}^e$ and in the generic case of anisotropy, the principal axes of $\Sigma_{\theta_2}^e$. The primary formula (2.17) already provides intuitively natural results:

The *principal axes of the effective conductivity tensor $\Sigma_{\theta_2}^e$ are identical to those of $\mathbf{M}(f(\mathbf{m}))$* , which are the so-called "directors" \mathbf{n}_j of the nematic liquid measured in light scattering experiments. The corresponding order parameter (eigenvalues) d_j of $\mathbf{M}(f)$, $\mathbf{M}\mathbf{n}_j = d_j\mathbf{n}_j$, which satisfy $0 \leq d_j \leq 1$, $\sum_{j=1}^3 d_j = 1$, measure the *degrees of optical anisotropy of the composite*. Whenever $d_j \neq 1/3$ or $\mathbf{M} \neq \mathbf{I}/3$, from (2.17), d_j enter explicitly into the degrees of conductivity anisotropy, which are measured by the eigenvalues σ_j^e of Σ^e . In a variety of special cases, we will explicitly calculate the distinct principal values (eigenvalues) σ_j^e and corresponding princi-

pal axes \mathbf{n}_j of $\Sigma_{\theta_2}^e$, which then generically lead to *three relative principal value enhancements*:

$$\mathcal{E}_j = \frac{\sigma_j^e - \sigma_1}{\sigma_1} = \frac{(\Sigma_{\theta_2}^e - \Sigma_0^e)}{\sigma_1} : \mathbf{n}_j \mathbf{n}_j, \quad j = 1, 2, 3. \quad (2.18)$$

Equivalently, the effective anisotropy tensor $\Sigma_{\theta_2}^e$ admits a representation explicitly in terms of its principal axes \mathbf{n}_j and relative enhancements \mathcal{E}_j :

$$\Sigma_{\theta_2}^e = \Sigma_0 + \sigma_1 \sum_{j=1}^3 \mathcal{E}_j \mathbf{n}_j \mathbf{n}_j. \quad (2.19)$$

The formula (2.17) therefore immediately yields a series of general conclusions, which then form the basis for simplified scaling properties in additional asymptotic limits, either on the molecule geometry or on the contrast between conductivities of the nano-inclusion and matrix.

2.4 Finer estimates for high contrast conductivity and extreme aspect ratio

For typical nematic polymer nano-composites, two asymptotic limits are routinely observed:

- high aspect ratio ($r \gg 1$), spheroidal nano-inclusions, where the molecules depicted in Figure 2.1 satisfy $a \gg b = c$; then L_a , equation (2.15) and Figure 2.2, admits the asymptotic evaluation

$$L_a = (\log(r)/r^2) + O(r^{-2}) \text{ for } r \gg 1; \quad (2.20)$$

- high contrast conductivities, where the nano-inclusion has extreme conductivity σ_2 relative to the matrix value σ_1 ,

$$\sigma_1/\sigma_2 \ll 1. \quad (2.21)$$

Table 2.1 indicates typical scaling properties for r , L_a and σ_1/σ_2 in nematic polymer composites. The fundamental formula (2.17) requires a careful analysis of the relative order among these two asymptotic parameters, σ_1/σ_2 and L_a , with the outcome dependent on three possi-

ble ranges for the ratio $\frac{L_a}{\sigma_1/\sigma_2}$, which we now analyze. These scaling results are valid for any molecular distribution function $f(\mathbf{m})$; in the next section, we will assert knowledge of $f(\mathbf{m})$ versus nano-element volume fraction and shear rate.

Table 2.1: Data for the range of typical aspect ratios r and electrical conductivity contrasts σ_1/σ_2 of rod-like nematic polymer nano-composites.

r	L_a	σ_1/σ_2
$10^2 \sim 10^5$	$10^{-9} \sim 10^{-3}$	$10^{-12} \sim 10^{-5}$

Case 1: Suppose $\frac{L_a}{\sigma_1/\sigma_2} \gg 1$, e.g. $L_a \sim 10^{-3}$ and $\sigma_1/\sigma_2 \sim 10^{-8}$.

Then the effective conductivity tensor $\Sigma_{\theta_2}^e$ (2.17), and corresponding relative enhancement \mathcal{E}_j (2.18), have the following scaling behavior:

$$\begin{cases} \Sigma_{\theta_2}^e &= \Sigma_0 + \frac{\sigma_1 \theta_2}{L_a} \mathbf{M} + O(\theta_2 \sigma_1) \mathbf{I} + O(\theta_2 \sigma_1) \mathbf{M} + O(\theta_2^2), \\ \mathcal{E}_j &= \frac{\sigma_j^e - \sigma_1}{\sigma_1} = \frac{\theta_2}{L_a} d_j + O(\theta_2), \quad j = 1, 2, 3. \end{cases} \quad (2.22)$$

Case 2: Suppose $\frac{L_a}{\sigma_1/\sigma_2} \sim O(1)$, e.g. $L_a \sim 10^{-6}$ and $\sigma_1/\sigma_2 \sim 10^{-6}$.

Then the scaling properties become:

$$\begin{cases} \Sigma_{\theta_2}^e &= \Sigma_0 + \frac{\theta_2 \sigma_2}{1 + \frac{L_a}{\sigma_1/\sigma_2}} \mathbf{M} + O(\theta_2 \sigma_1) \mathbf{I} + O(\theta_2 \sigma_1) \mathbf{M} + O(\theta_2^2), \\ \mathcal{E}_j &= \frac{\theta_2 (\sigma_2/\sigma_1)}{1 + \frac{L_a}{\sigma_1/\sigma_2}} d_j + O(\theta_2), \quad j = 1, 2, 3. \end{cases} \quad (2.23)$$

Case 3: Suppose $\frac{L_a}{\sigma_1/\sigma_2} \ll 1$, e.g. $L_a \sim 10^{-7}$ and $\sigma_1/\sigma_2 \sim 10^{-5}$.

Then the scaling properties become:

$$\begin{cases} \Sigma_{\theta_2}^e &= \Sigma_0 + \theta_2 \sigma_2 \mathbf{M} + O(\theta_2 \sigma_1) \mathbf{I} + O(\theta_2 \sigma_1) \mathbf{M} + O(\theta_2^2), \\ \mathcal{E}_j &= \theta_2 (\sigma_2/\sigma_1) d_j + O(\theta_2), \quad j = 1, 2, 3. \end{cases} \quad (2.24)$$

Comments: *The property impact (relative gain) due to the nano-inclusions becomes apparent and significant.* In each case, the relative enhancement of the effective conductivity is captured by a product of the volume fraction $\theta_2 \sim O(10^{-2})$ and either L_a^{-1} or σ_2/σ_1 , which are both expected to be comparable to θ_2^{-1} and potentially much greater.

Recall the principal values d_j of $\mathbf{M}(f(\mathbf{m}))$ satisfy $0 \leq d_j \leq 1$, $\sum_{j=1}^3 d_j = 1$. When the distribution is random, all $d_j = 1/3$, and otherwise $1/3 < d_1 < 1$.

So far, these results are quite general; we now inject explicit knowledge about $f(\mathbf{m})$ and $\mathbf{M}(f(\mathbf{m}))$. In the dilute concentration regime, we (Forest *et al.* (2004)) have recently derived explicit formulas for f in weak shear, and thereby have a precise characterization of $\mathbf{M}(f)$, and consequently \mathbf{P} and $\Sigma_{\theta_2}^e$. There are only preliminary analytical characterizations of f at very high nematic concentrations (Constantin *et al.* (2004)). Nonetheless, decades of mesoscopic theory are based on closing the equations at the second-moment tensor level of resolution of f (Beris and Edwards (1994), de Gennes and Prost (1993), Larson (1999)). In particular we (Forest and Wang (2003), Forest *et al.* (2003)) have introduced moment-closure benchmarks based on faithful reproduction of the PDF attractors & phase transitions versus concentration (volume fraction) and shear rate. Using special properties of the Doi theory (Forest *et al.* (2003), Forest *et al.* (2004 c)), we can easily extend these formulas to any linear planar flow in the weak flow rate limit. In all these cases we can now give explicit formulas for \mathbf{P} and $\Sigma_{\theta_2}^e$; we proceed to several illustrative examples.

2.5 Applications I: Effective conductivity tensors for quiescent and shear-induced mesophases

2.5.1 Dilute isotropic concentrations $f_0(\mathbf{m}) = \frac{1}{4\pi}$

If the molecular inclusions are randomly oriented, i.e. $f(\mathbf{m}) \equiv 1/(4\pi)$, then $\mathbf{M} = \mathbf{I}/3$ with all $d_j = 1/3$, and the effective conductivity tensor $\Sigma_{\theta_2}^e$ remains isotropic (i.e. proportional to \mathbf{I}), with an explicit characterization of the inclusions:

$$\Sigma_{\theta_2}^e = \Sigma_0 + \frac{\sigma_1 \theta_2 (\sigma_2 - \sigma_1)(\sigma_2 + 5\sigma_1 + 3(\sigma_2 - \sigma_1)L_a)}{3(\sigma_2 + \sigma_1 - (\sigma_2 - \sigma_1)L_a)(\sigma_1 + (\sigma_2 - \sigma_1)L_a)} \mathbf{I} + O(\theta_2^2). \quad (2.25)$$

Equivalently, we have the decomposition

$$\Sigma_{\theta_2}^e = \Sigma_0 + \sigma_1 \mathcal{E}^{iso} \mathbf{I}, \quad (2.26)$$

where the *scalar, isotropic, relative effective conductivity enhancement* \mathcal{E}^{iso} is

$$\mathcal{E}^{iso} = (\Sigma_{\theta_2}^e - \Sigma_0^e) : \mathbf{n}\mathbf{n} = \frac{\theta_2(\sigma_2 - \sigma_1)(\sigma_2 + 5\sigma_1 + 3(\sigma_2 - \sigma_1)L_a)}{3(\sigma_2 + \sigma_1 - (\sigma_2 - \sigma_1)L_a)(\sigma_1 + (\sigma_2 - \sigma_1)L_a)} + O(\theta_2^2). \quad (2.27)$$

Here \mathbf{n} is any unit vector, since for isotropic tensors, any unit vector is a principal axis.

For high contrast and high aspect ratio molecular elements at dilute concentrations in the isotropic phase, we simply insert $\mathbf{M} = \mathbf{I}/3$ into the formulas in Section 2.4 or analyze (2.25), (2.26) directly, with the following results.

- When $\frac{L_a}{\sigma_1/\sigma_2} \gg 1$,

$$\begin{cases} \Sigma_{\theta_2}^e & \approx \sigma_1(1 + \frac{\theta_2}{3L_a})\mathbf{I}, \\ \mathcal{E}^{iso} & \approx \frac{\theta_2}{3L_a}. \end{cases} \quad (2.28)$$

- When $\frac{L_a}{\sigma_1/\sigma_2} \sim O(1)$,

$$\begin{cases} \Sigma_{\theta_2}^e & \approx \sigma_1 \left(1 + \frac{\theta_2(\sigma_2/\sigma_1)}{3(1 + \frac{3L_a}{\sigma_1/\sigma_2})} \right) \mathbf{I}, \\ \mathcal{E}^{iso} & \approx \frac{\theta_2(\sigma_2/\sigma_1)}{3(1 + \frac{L_a}{\sigma_1/\sigma_2})}. \end{cases} \quad (2.29)$$

- When $\frac{L_a}{\sigma_1/\sigma_2} \ll 1$,

$$\begin{cases} \Sigma_{\theta_2}^e & \approx \sigma_1(1 + \frac{\theta_2\sigma_2}{3\sigma_1})\mathbf{I}, \\ \mathcal{E}^{iso} & \approx \frac{\theta_2(\sigma_2/\sigma_1)}{3}. \end{cases} \quad (2.30)$$

These formulas explicitly clarify that, *even at quiescent dilute concentrations*, when e.g. $\theta_2 \approx 5 \times 10^{-3}$, *a high conductivity contrast* ($\sigma_1/\sigma_2 \ll 1$) *or an extreme molecular aspect ratio* ($L_a \ll 1$) *will overwhelm the low volume fraction and conservatively lead to gains in effective*

conductivity on the order of 100-1000%.

2.5.2 Shear-induced monodomains at dilute concentrations

Our goal here is to extract the flow-induced scaling corrections to the above results, (2.25)-(2.30), as well as the weak anisotropy induced by weak shear flow. We analyze the PDF $f(\mathbf{m})$ arising from weak steady shear of dilute spheroidal nematic polymers (Forest *et al.* (2004)), where the asymptotic parameter is the Peclet number Pe , the ratio of shear rate to average molecular relaxation rate. The normalized flow field is $\mathbf{v} \equiv Pe(y, 0, 0)$, where $0 < Pe \ll 1$. The result is:

$$\begin{aligned} f &= \frac{1}{\sqrt{4\pi}}(f_0 + Pe f_1 + O(Pe^2)), \quad \text{with} \\ f_0 &= \frac{1}{\sqrt{4\pi}}, \quad f_1 = \frac{i}{2} \sqrt{\frac{5}{6}} \frac{a}{N-5} (Y_2^2 - Y_2^{-2}), \end{aligned} \quad (2.31)$$

where $a = \frac{r^2 - 1}{r^2 + 1}$ is the molecule geometry parameter, N is a dimensionless concentration related to θ_2 by

$$\frac{N}{\theta_2} = \frac{8r}{\pi}, \quad (2.32)$$

and Y_2^2, Y_2^{-2} are spherical harmonics which capture anisotropy of the orientational distribution of the nano-inclusions generated by the shear flow. The representation (2.31) is valid for $0 < N < 5 - 1.869a^{1/2}Pe^{1/2}$, equivalently for $0 < \theta_2 < \frac{1}{r} (1.9635 - 0.734\sqrt{\frac{r^2 - 1}{r^2 + 1}}Pe^{1/2})$, the range of volume fractions for which the sheared isotropic phase persists and is stable. The upper bound on N was first derived by See, Doi and Larson (See *et al.* (1990)) and corresponds to a turning point bifurcation of the shear-perturbed Smoluchowski equation (Forest *et al.* (2004)). These scaling properties are necessary to control the PDF expansion (2.31) and see that it is bounded at the upper limit on θ_2 (respectively, N) as the shear-perturbed, nearly isotropic steady states become unstable.

We now simply insert (2.31) into (1.23) and compute the integral. At first order in Pe , we

have

$$\mathbf{M}(f(\mathbf{m})) = \begin{pmatrix} \frac{1}{3} & -\frac{Pe}{6(N-5)} & \\ -\frac{Pe}{6(N-5)} & \frac{1}{3} & 0 \\ 0 & 0 & \frac{1}{3} \end{pmatrix}, \quad (2.33)$$

whose principal values are

$$d_1 = \frac{1}{3} + \frac{Pe}{6(N-5)}, \quad d_2 = \frac{1}{3}, \quad d_3 = \frac{1}{3} - \frac{Pe}{6(N-5)}, \quad (2.34)$$

with principal axes \mathbf{n}_j listed below.

The anisotropic effective conductivity tensor Σ^e follows in explicit form from $\mathbf{M}(f)$ by the formula (2.17), and more precisely from (2.22)-(2.24) given more refined information. The principal directions \mathbf{n}_j of $\Sigma_{\theta_2}^e$ (inherited from \mathbf{M}) at leading order are aligned midway between the flow (x) and flow-gradient (y) direction and along the vorticity (z) axis,

$$\mathbf{n}_1 = (1, 1, 0), \mathbf{n}_2 = (0, 0, 1), \mathbf{n}_3 = (1, -1, 0), \quad (2.35)$$

where the corresponding *principal values* σ_j^e of $\Sigma_{\theta_2}^e$ are *distinct and ordered*, $\sigma_1^e = \sigma_{max}^e > \sigma_2^e = \sigma_{vorticity}^e > \sigma_3^e = \sigma_{min}^e$, with explicit formulas given below.

- For $\frac{L_a}{\sigma_1/\sigma_2} \gg 1$, the 3 distinct principal values of $\Sigma_{\theta_2}^2$ are

$$\begin{aligned} \sigma_{max}^e &\approx \sigma_1 \left(1 + \frac{\theta_2}{3 L_a}\right) + \frac{Pe \theta_2 \sigma_1}{6(5-N) L_a} \approx \sigma_1 + \sigma_1(\mathcal{E}^{iso} + \mathcal{E}_{Pe}^{iso}), \\ \sigma_{vorticity}^e &\approx \sigma_1 \left(1 + \frac{\theta_2}{3 L_a}\right) \approx \sigma_1 + \sigma_1 \mathcal{E}^{iso}, \\ \sigma_{min}^e &\approx \sigma_1 \left(1 + \frac{\theta_2}{3 L_a}\right) - \frac{Pe \theta_2 \sigma_1}{6(5-N) L_a} \approx \sigma_1 + \sigma_1(\mathcal{E}^{iso} - \mathcal{E}_{Pe}^{iso}). \end{aligned} \quad (2.36)$$

The *maximum relative conductivity enhancement* is given by:

$$\begin{aligned}
\mathcal{E}_{max} &= \frac{(\Sigma_{\theta_2, Pe}^e - \Sigma_{0,0}^e)}{\sigma_1} : \mathbf{n}_1 \mathbf{n}_1 = \frac{\sigma_{max}^e - \sigma_1}{\sigma_1} \\
&= \frac{(\Sigma_{\theta_2, Pe}^e - \Sigma_{\theta_2, 0}^e + \Sigma_{\theta_2, 0}^e - \Sigma_{0,0}^e)}{\sigma_1} : \mathbf{n}_1 \mathbf{n}_1 \\
&\approx \frac{\theta_2}{3L_a} + \frac{Pe \theta_2}{6(5-N)L_a} \\
&\approx \mathcal{E}^{iso} + \mathcal{E}_{Pe}^{iso}.
\end{aligned} \tag{2.37}$$

- For $\frac{L_a}{\sigma_1/\sigma_2} \sim O(1)$, the 3 distinct principal values of $\Sigma_{\theta_2}^e$ and maximum relative conductivity enhancement are

$$\begin{aligned}
\sigma_{max}^e &\approx \sigma_1 + \frac{\theta_2 \sigma_2}{3(1 + \frac{L_a}{\sigma_1/\sigma_2})} + \frac{Pe \theta_2 \sigma_2}{6(5-N)(1 + \frac{L_a}{\sigma_1/\sigma_2})} \approx \sigma_1 + \sigma_1(\mathcal{E}^{iso} + \mathcal{E}_{Pe}^{iso}), \\
\sigma_{vorticity}^e &\approx \sigma_1 + \frac{\theta_2 \sigma_2}{3(1 + \frac{L_a}{\sigma_1/\sigma_2})} \approx \sigma_1 + \sigma_1 \mathcal{E}^{iso}, \\
\sigma_{min}^e &\approx \sigma_1 + \frac{\theta_2 \sigma_2}{3(1 + \frac{L_a}{\sigma_1/\sigma_2})} - \frac{Pe \theta_2 \sigma_2}{6(5-N)(1 + \frac{L_a}{\sigma_1/\sigma_2})} \approx \sigma_1 + \sigma_1(\mathcal{E}^{iso} - \mathcal{E}_{Pe}^{iso}), \\
\mathcal{E}_{max} &\approx \frac{\theta_2 (\sigma_2/\sigma_1)}{3(1 + \frac{L_a}{\sigma_1/\sigma_2})} + \frac{Pe \theta_2 (\sigma_2/\sigma_1)}{6(5-N)(1 + \frac{L_a}{\sigma_1/\sigma_2})} \approx \mathcal{E}^{iso} + \mathcal{E}_{Pe}^{iso}.
\end{aligned} \tag{2.38}$$

- For $\frac{L_a}{\sigma_1/\sigma_2} \ll 1$, the formulas are

$$\begin{aligned}
\sigma_{max}^e &\approx \sigma_1(1 + \frac{\theta_2 \sigma_2}{3\sigma_1}) + \frac{Pe \theta_2 \sigma_2}{6(5-N)} \approx \sigma_1 + \sigma_1(\mathcal{E}^{iso} + \mathcal{E}_{Pe}^{iso}), \\
\sigma_{vorticity}^e &\approx \sigma_1(1 + \frac{\theta_2 \sigma_2}{3\sigma_1}) \approx \sigma_1 + \sigma_1 \mathcal{E}^{iso}, \\
\sigma_{min}^e &\approx \sigma_1(1 + \frac{\theta_2 \sigma_2}{3\sigma_1}) - \frac{Pe \theta_2 \sigma_2}{6(5-N)} \approx \sigma_1 + \sigma_1(\mathcal{E}^{iso} - \mathcal{E}_{Pe}^{iso}), \\
\mathcal{E}_{max} &\approx \frac{\theta_2 (\sigma_2/\sigma_1)}{3} + \frac{Pe \theta_2 (\sigma_2/\sigma_1)}{6(5-N)} \approx \mathcal{E}^{iso} + \mathcal{E}_{Pe}^{iso}.
\end{aligned} \tag{2.39}$$

Notice: In all three limits, the overall conductivity enhancement is a sum of the quiescent isotropic enhancement \mathcal{E}^{iso} and a flow-induced enhancement \mathcal{E}_{Pe}^{iso} .

The relative size of \mathcal{E}^{iso} and \mathcal{E}_{Pe}^{iso} defers to $1/3$ vs. $Pe/(6(5-N))$. The latter term increases with both Pe and N and is bounded from above by $O(Pe^{1/2})$. The contributions appear to be comparable even at weak shear rates, so formula (2.17) predicts a definite benefit from weak flow processing.

We can also define the conductivity analog of optical birefringence Bi , which is

$$Bi = d_{max} - d_{min} = d_1 - d_3, \quad (2.40)$$

where d_i are the principal values of $\mathbf{M}(f(\mathbf{m}))$. The analog is the *maximum conductivity contrast* along the major and minor principal axes, $\sigma_{contrast}^e$, given by

$$\sigma_{contrast}^e = \sigma_1(\mathcal{E}_{max} - \mathcal{E}_{min}). \quad (2.41)$$

Naturally, *the maximum anisotropy in conductivity comes purely from the shear flow* for these three dilute concentration cases:

$$\mathcal{E}_{max} - \mathcal{E}_{min} \approx \begin{cases} \frac{Pe \theta_2}{3(5-N)L_a}, & \frac{L_a}{\sigma_1/\sigma_2} \gg 1; \\ \frac{Pe \theta_2 (\sigma_2/\sigma_1)}{3(1 + \frac{L_a}{\sigma_1/\sigma_2})(5-N)}, & \frac{L_a}{\sigma_1/\sigma_2} \sim O(1); \\ \frac{Pe \theta_2 (\sigma_2/\sigma_1)}{3(5-N)}, & \frac{L_a}{\sigma_1/\sigma_2} \ll 1. \end{cases} \quad (2.42)$$

Note: Indeed, the above expressions can be directly cast in terms of the optical birefringence parameter, Bi , by using the formulas for d_j in (2.34). Doing so, we find

$$\sigma_{contrast}^e = \sigma_1(\mathcal{E}_{max} - \mathcal{E}_{min}) \approx \begin{cases} \frac{\sigma_1 \theta_2}{L_a} Bi, & \frac{L_a}{\sigma_1/\sigma_2} \gg 1; \\ \frac{\theta_2 \sigma_2}{(1 + \frac{L_a}{\sigma_1/\sigma_2})} Bi, & \frac{L_a}{\sigma_1/\sigma_2} \sim O(1); \\ \theta_2 \sigma_2 Bi, & \frac{L_a}{\sigma_1/\sigma_2} \ll 1. \end{cases} \quad (2.43)$$

2.5.3 Quiescent nematic phases and mesoscopic approximations

Exact formulas for the PDF $f(\mathbf{m})$ at nematic concentrations do not exist, except in the limit as $N \rightarrow \infty$ (Constantin *et al.* (2004)). Alternatively, we employ second-moment closure models, where scaling properties can be derived and subsequently compared with numerical computations or with other closures. We consider the Doi closure model for illustrative purposes, given in terms of the orientation tensor \mathbf{Q} , $\mathbf{Q} = \mathbf{M} - 1/3 \mathbf{I}$, capturing the deviatoric part of $\mathbf{M}(f)$ which measures the departure from isotropy. Nematic states exist for sufficiently high concentration $N > 8/3$, equivalently for $\theta_2 > \pi/(3r)$, in the Doi closure model. (We remark that N has been effectively scaled by the closure; $N = 8/3$ here is only proportional to the critical value for kinetic theory, which for $r \rightarrow \infty$ is approximately $N=4$.) For the uniaxial nano-inclusion distribution at rest, $\mathbf{Q} = s(\mathbf{nn} - \mathbf{I}/3)$, where s is the uniaxial order parameter ($s = d_1 - d_2$, $d_2 = d_3$), which measures anisotropy of the distribution; the isotropic phase has $s = 0$, whereas the stable nematic phase has

$$s = \frac{1}{4} \left(1 + 3\sqrt{1 - \frac{8}{3N}} \right) \in \left(\frac{1}{4}, 1 \right). \quad (2.44)$$

The uniaxial director $\mathbf{n} = (\cos \phi \sin \theta, \sin \phi \sin \theta, \cos \theta)$ is the principal axis of \mathbf{Q} or \mathbf{M} corresponding to the distinct, maximum eigenvalue (d_1 of \mathbf{M} , $d_1 - 1/3$ of \mathbf{Q}).

Consider the orientation tensor \mathbf{Q} at rest, corresponding to major director $\mathbf{n}_0 = (\cos \phi_0 \sin \theta_0, \sin \phi_0 \sin \theta_0, \cos \theta_0)$. The nematic phase is $O(3)$ degenerate, meaning any similarity transformation of \mathbf{Q} , $\mathcal{O}^t \mathbf{Q} \mathcal{O}$, is also an equilibrium, where $\mathcal{O} \in O(3)$, the orthogonal group. From the primary formula (2.17) and remarks below, the principal axes of the effective conductivity tensor $\Sigma_{\theta_2}^e$ are also $O(3)$ invariant, whereas, the anisotropic principal values σ_i^e for $\Sigma_{\theta_2}^e$ have scaling behavior that depends on three limit cases of L_a vs. σ_1/σ_2 .

- For $\frac{L_a}{\sigma_1/\sigma_2} \gg 1$,

$$\begin{aligned}
\sigma_1^e &= \sigma_{max}^e \approx \sigma_1 + \frac{\theta_2 \sigma_1}{3 L_a} (1 + 2s), \\
\sigma_2^e &= \sigma_3^e = \sigma_{min}^e \approx \sigma_1 + \frac{\theta_2 \sigma_1}{3 L_a} (1 - s), \\
\mathcal{E}_{max} &\approx \frac{\theta_2}{3 L_a} + \frac{2 s \theta_2}{3 L_a} \approx \mathcal{E}^{iso} + \mathcal{E}^{nema}.
\end{aligned} \tag{2.45}$$

- For $\frac{L_a}{\sigma_1/\sigma_2} \sim O(1)$,

$$\begin{aligned}
\sigma_1^e &= \sigma_{max}^e \approx \sigma_1 + \frac{\theta_2 \sigma_2}{3 \left(1 + \frac{L_a}{\sigma_1/\sigma_2}\right)} (1 + 2s), \\
\sigma_2^e &= \sigma_3^e = \sigma_{min}^e \approx \sigma_1 + \frac{\theta_2 \sigma_2}{3 \left(1 + \frac{L_a}{\sigma_1/\sigma_2}\right)} (1 - s), \\
\mathcal{E}_{max} &\approx \frac{\theta_2 (\sigma_2/\sigma_1)}{3 \left(1 + \frac{L_a}{\sigma_1/\sigma_2}\right)} + \frac{2 s \theta_2 (\sigma_2/\sigma_1)}{3 \left(1 + \frac{L_a}{\sigma_1/\sigma_2}\right)} \approx \mathcal{E}^{iso} + \mathcal{E}^{nema}.
\end{aligned} \tag{2.46}$$

- For $\frac{L_a}{\sigma_1/\sigma_2} \ll 1$,

$$\begin{aligned}
\sigma_1^e &= \sigma_{max}^e \approx \sigma_1 + \frac{1}{3} \theta_2 \sigma_2 (1 + 2s), \\
\sigma_2^e &= \sigma_3^e = \sigma_{min}^e \approx \sigma_1 + \frac{1}{3} \theta_2 \sigma_2 (1 - s), \\
\mathcal{E}_{max} &\approx \frac{\theta_2 (\sigma_2/\sigma_1)}{3} + \frac{2 \theta_2 (\sigma_2/\sigma_1) s}{3} \approx \mathcal{E}^{iso} + \mathcal{E}^{nema}.
\end{aligned} \tag{2.47}$$

The maximum anisotropy in conductivity of the quiescent nematic phase for these three cases is now explicit:

$$\mathcal{E}_{max} - \mathcal{E}_{min} \approx \begin{cases} \frac{\theta_2 s}{L_a}, & \frac{L_a}{\sigma_1/\sigma_2} \gg 1; \\ \frac{\theta_2 (\sigma_2/\sigma_1) s}{1 + \frac{L_a}{\sigma_1/\sigma_2}}, & \frac{L_a}{\sigma_1/\sigma_2} \sim O(1); \\ \frac{\theta_2 \sigma_2 s}{\sigma_1}, & \frac{L_a}{\sigma_1/\sigma_2} \ll 1. \end{cases} \tag{2.48}$$

Comparison of these scaling properties (2.48) of the pure nematic phase with both the pure

isotropic phase (Section 2.5.1) and the shear-induced isotropic phase (Section 2.5.2) reveals the same isotropic enhancement \mathcal{E}^{iso} *plus* a magnification of the anisotropic enhancement (2.42) with the asymptotic pre-factor Pe replaced by the $O(1)$ scalar order parameter $s \in (1/4, 1)$. As we illustrate later, these scaling properties clearly expose the dominant effect of nematic order on the conductivity enhancement, with a discontinuous gain in \mathcal{E}_{max} as the order parameter S jumps at the disorder-order phase transition ($N = 8/3$ in this model).

2.5.4 Shear perturbed, flow-aligned monodomains at nematic concentrations

Until this point, we have characterized effects of shear on the isotropic phase and of the order transition to the nematic phase, to which we now couple the effects due to weak shear. This will only perturbatively alter the principal values of the anisotropic conductivity tensor, but has the important effect of selecting the principal axes of anisotropy, i.e. breaking the $O(3)$ degeneracy of the nematic phase. The perturbed solution \mathbf{Q} corresponding to a shear-induced monodomain at low shear rate ($Pe \ll 1$) is explicitly constructed (Forest *et al.* (2003)),

$$\mathbf{Q} = s(\mathbf{nn} - \frac{1}{3}\mathbf{I}) + Pe \left[\frac{c_1}{2} \begin{pmatrix} 0 & 1 & 0 \\ 1 & 0 & 0 \\ 0 & 0 & 0 \end{pmatrix} + c_2 \begin{pmatrix} 1 & 0 & 0 \\ 0 & 1 & 0 \\ 0 & 0 & -2 \end{pmatrix} + c_3 \begin{pmatrix} 1 & 0 & 0 \\ 0 & -1 & 0 \\ 0 & 0 & 0 \end{pmatrix} \right] + O(Pe^2), \quad (2.49)$$

where s depends only on θ_2 from (2.44), the $O(1)$ estimate of the shear-selected major director of \mathbf{Q} is $\mathbf{n} = (\cos \phi_L, \sin \phi_L, 0)$, where the so-called Leslie alignment angle $\phi_L = \frac{1}{2} \cos^{-1} \left(\frac{3s}{a(2+s)} \right)$ depends on θ_2 (through s) and aspect ratio (through a); and the constants c_i depend on θ_2 and r ,

$$\begin{aligned} c_1 &= \frac{(1-s)^2(1+2s)}{9s(4s-1)} \left[a(11s+4) - \frac{9s^2(19s+8)}{a(2+s)^2} \right], \\ c_2 &= \frac{(1-s)^2(1+2s) \tan 2\phi_L}{6(4s-1)}, \\ c_3 &= \frac{3s(1-s)^2(1+2s)(19s+8) \tan 2\phi_L}{6a(2+s)^2(4s-1)}. \end{aligned} \quad (2.50)$$

The $O(Pe)$ shear-dependent angle $\tilde{\phi}_L$ of the major director $\tilde{\mathbf{n}}$ of \mathbf{Q} , $\tilde{\mathbf{n}} = (\cos \tilde{\phi}_L, \sin \tilde{\phi}_L, 0)$, is given by

$$\cos 2\tilde{\phi} = \cos 2\phi_L + Pe \frac{4(1-s)^2(1+2s)^2 \sin 2\phi_L}{3s(2+s)(4s-1)} + O(Pe^2). \quad (2.51)$$

The principal values of $\Sigma_{\theta_2, Pe}^e$ in the three different limit cases follow, where σ_{max}^e is associated with the principal axis $\tilde{\mathbf{n}}$, $\sigma_{vorticity}^e$ with $(0, 0, 1)$, and σ_{min}^e with the normal $\tilde{\mathbf{n}}^\perp$ to $\tilde{\mathbf{n}}$ in the shear plane. This implies, for example, that the maximum conductivity anisotropy lies in the plane of flow deformation for these flow-aligned monodomains. (As the shear rate and volume fraction vary, a remarkable array of transient orientational distributions emerge (Faraoni *et al.* (1999), Forest *et al.* (2004a), Forest *et al.* (2004b), Grosso *et al.* (2001), Larson and Ottinger (1991)), whose conductivity will likewise oscillate until the system is quenched. These dynamic properties will be reported in a subsequent study.)

- For $\frac{L_a}{\sigma_1/\sigma_2} \gg 1$,

$$\begin{aligned} \sigma_{max}^e &\approx \sigma_1 + \frac{\theta_2 \sigma_1}{3 L_a} (1 + 2s + \chi(a, \theta_2) Pe), \\ \sigma_{vorticity}^e &\approx \sigma_1 + \frac{\theta_2 \sigma_1}{3 L_a} \left(1 - s - \chi(a, \theta_2) Pe \frac{s+2}{3(1+2s)} \right), \\ \sigma_{min}^e &\approx \sigma_1 + \frac{\theta_2 \sigma_1}{3 L_a} \left(1 - s - \chi(a, \theta_2) Pe \frac{5s+1}{3(1+2s)} \right). \end{aligned} \quad (2.52)$$

where χ is a recurring factor that depends only on the aspect ratio parameter a and the volume fraction θ_2 , depicted in Figure 2.3 for aspect ratio $r = 100$,

$$\chi(a, \theta_2) = \frac{a(1-s)^2(1+2s)^2 \sin 2\phi_L}{s(4s-1)}. \quad (2.53)$$

So the maximum enhancement is given by

$$\begin{aligned} \mathcal{E}_{max} &\approx \frac{\theta_2}{3 L_a} (1 + 2s + \chi(a, \theta_2) Pe) \approx \mathcal{E}^{iso} + \mathcal{E}^{nema} + \mathcal{E}_{Pe}^{nema}, \\ \mathcal{E}_{Pe}^{nema} &\approx Pe \cdot \frac{\theta_2}{3 L_a} \cdot \chi(a, \theta_2), \end{aligned} \quad (2.54)$$

where the first two terms are precisely the result (2.45) without flow, and the new term

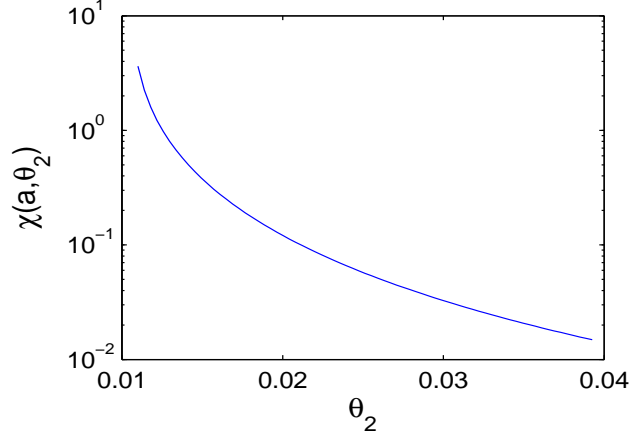


Figure 2.3: The scaling factor $\chi(a, \theta_2)$ vs. θ_2 , for $r = 100$.

is the flow-induced enhancement \mathcal{E}_{Pe}^{nema} of the nematic phase. We note that even though Pe is small, e.g. $Pe \sim 0.1$, the product $\chi \cdot Pe$ is comparable to the other two factors 1 and $2s$, when θ_2 is close to 1%.

The decomposition formula (2.54a) will be reproduced in the two remaining regimes, where the precise forms of the isotropic (dilute) enhancement \mathcal{E}^{iso} , the boost \mathcal{E}^{nema} from the nematic phase, and the flow-induced enhancement of the nematic phase \mathcal{E}_{Pe}^{nema} , depend on the ratio of L_a and σ_1/σ_2 . In all cases, the property enhancement decomposes into the sum of these three contributions, illustrated in Section 2.5.5.

- For $\frac{L_a}{\sigma_1/\sigma_2} \sim O(1)$,

$$\begin{aligned}
\sigma_{max}^e &\approx \sigma_1 + \frac{\theta_2 \sigma_2}{3(1 + \frac{L_a}{\sigma_1/\sigma_2})} (1 + 2s + \chi(a, \theta_2) Pe), \\
\sigma_{vorticity}^e &\approx \sigma_1 + \frac{\theta_2 \sigma_2}{3(1 + \frac{L_a}{\sigma_1/\sigma_2})} \left(1 - s - \chi(a, \theta_2) Pe \frac{s+2}{3(1+2s)} \right), \\
\sigma_{min}^e &\approx \sigma_1 + \frac{\theta_2 \sigma_2}{3(1 + \frac{L_a}{\sigma_1/\sigma_2})} \left(1 - s - \chi(a, \theta_2) Pe \frac{5s+1}{3(1+2s)} \right), \\
\mathcal{E}_{max} &\approx \frac{\theta_2 (\sigma_2/\sigma_1)}{3(1 + \frac{L_a}{\sigma_1/\sigma_2})} (1 + 2s + \chi(a, \theta_2) Pe) \approx \mathcal{E}^{iso} + \mathcal{E}^{nema} + \mathcal{E}_{Pe}^{nema},
\end{aligned} \tag{2.55}$$

where

$$\mathcal{E}_{Pe}^{nema} \approx Pe \cdot \frac{\theta_2(\sigma_2/\sigma_1)}{3(1 + \frac{L_a}{\sigma_2/\sigma_1})} \cdot \chi(a, \theta_2). \quad (2.56)$$

- For $\frac{L_a}{\sigma_2/\sigma_1} \ll 1$,

$$\begin{aligned} \sigma_{max}^e &\approx \sigma_1 + \frac{\theta_2 \sigma_2}{3} (1 + 2s + \chi(a, \theta_2) Pe), \\ \sigma_{vorticity}^e &\approx \sigma_1 + \frac{\theta_2 \sigma_2}{3} \left(1 - s - \chi(a, \theta_2) Pe \frac{s+2}{3(1+2s)} \right), \\ \sigma_{min}^e &\approx \sigma_1 + \frac{\theta_2 \sigma_2}{3} \left(1 - s - \chi(a, \theta_2) Pe \frac{5s+1}{3(1+2s)} \right), \\ \mathcal{E}_{max} &\approx \frac{\theta_2 \sigma_2}{3\sigma_1} (1 + 2s + \chi(a, \theta_2) Pe) \approx \mathcal{E}^{iso} + \mathcal{E}^{nema} + \mathcal{E}_{Pe}^{nema}, \end{aligned} \quad (2.57)$$

where

$$\mathcal{E}_{Pe}^{nema} \approx Pe \cdot \frac{\theta_2(\sigma_2/\sigma_1)}{3} \cdot \chi(a, \theta_2). \quad (2.58)$$

Finally, the maximum anisotropy in effective conductivity for these three cases is given by

$$\mathcal{E}_{max} - \mathcal{E}_{min} \approx \begin{cases} \frac{\theta_2}{L_a} \left(s + \chi(a, \theta_2) Pe \frac{11s+4}{9(1+2s)} \right), & \frac{L_a}{\sigma_1/\sigma_2} \gg 1; \\ \frac{\theta_2(\sigma_2/\sigma_1)}{(1 + \frac{L_a}{\sigma_1/\sigma_2})} \left(s + \chi(a, \theta_2) Pe \frac{11s+4}{9(1+2s)} \right), & \frac{L_a}{\sigma_1/\sigma_2} \sim O(1); \\ \theta_2(\sigma_2/\sigma_1) \left(s + \chi(a, \theta_2) Pe \frac{11s+4}{9(1+2s)} \right), & \frac{L_a}{\sigma_1/\sigma_2} \ll 1. \end{cases} \quad (2.59)$$

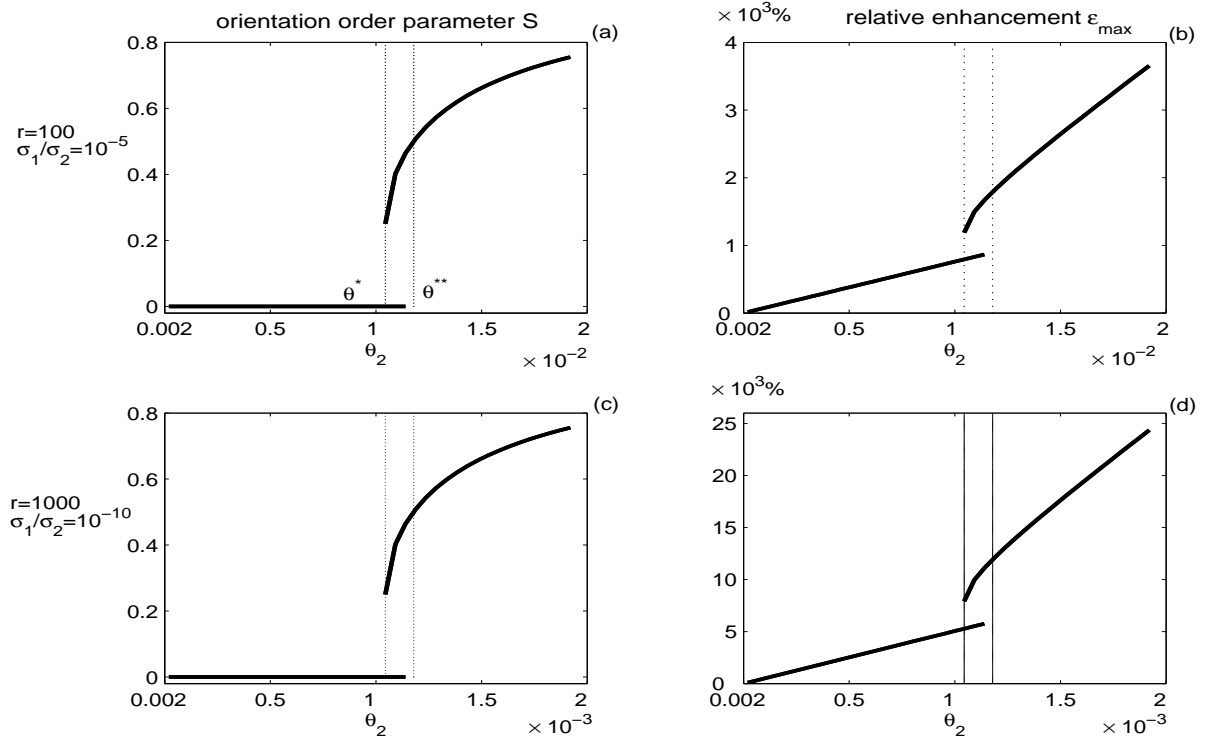


Figure 2.4: Quiescent orientation-conductivity enhancement correlations versus volume fraction for two model nano-composites. Hysteresis associated with the quiescent I-N phase transition is duplicated in the effective conductivity property enhancement for two model systems. Left column: Order parameter S versus volume fraction θ_2 . Right column: Corresponding relative conductivity enhancement \mathcal{E}_{\max} . Model system aspect ratio and conductivity contrasts are given for each row. The two vertical lines mark the critical concentration, θ_2^* and θ_2^{**} , of each model system; θ_2^* is the onset of the nematic phase, while θ_2^{**} is the instability transition of the isotropic phase.

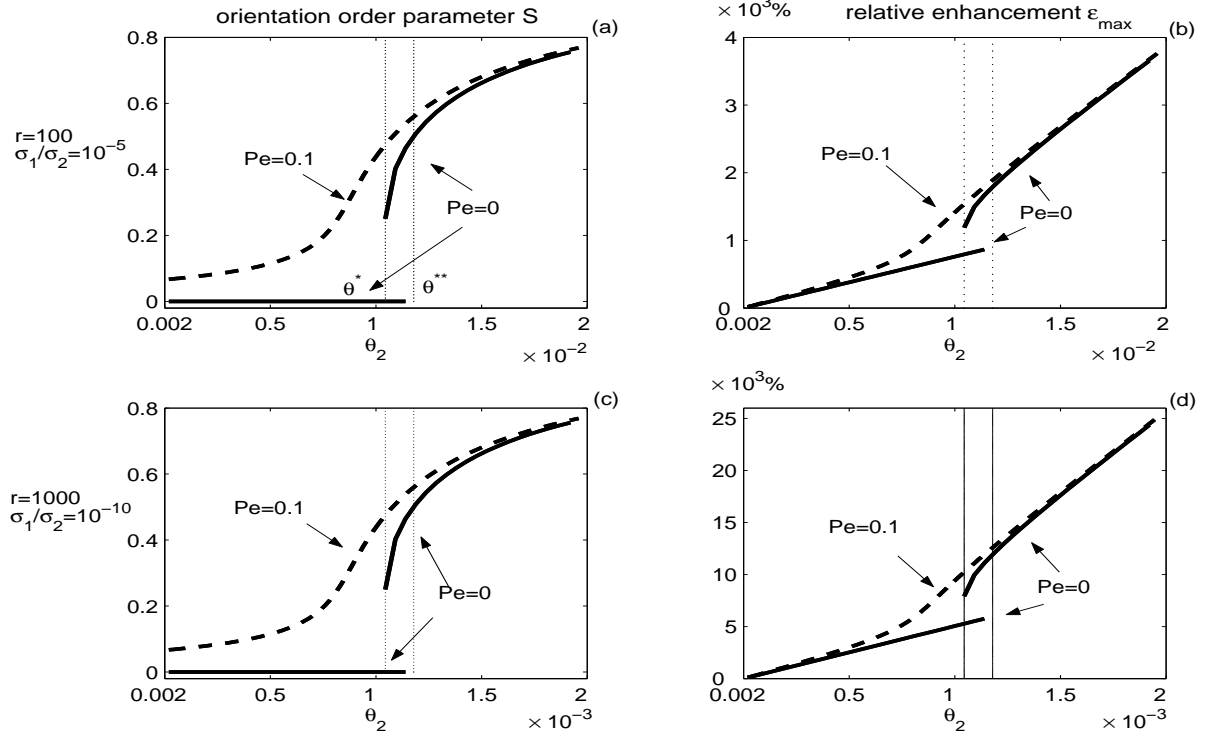


Figure 2.5: Comparison between shear-induced and quiescent orientation order parameter versus volume fraction, and the corresponding effective conductivity enhancements for the two model systems of Figure 2.4. Left column: Order parameter S versus volume fraction θ_2 (dark color is for $Pe=0$, light color is for weak shear rate $Pe = 0.1$). Right column: Corresponding relative conductivity enhancements.

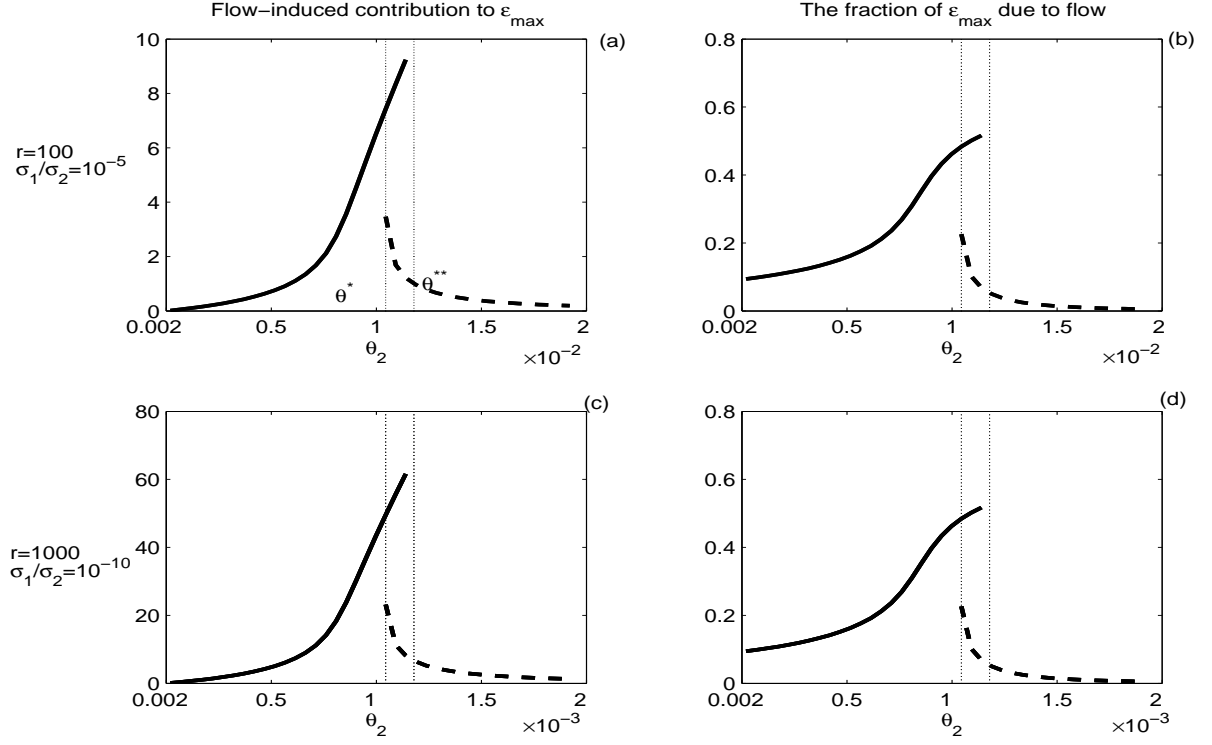


Figure 2.6: Left column: The flow-induced contribution to \mathcal{E}_{max} , defined by $\mathcal{E}_{max} - \mathcal{E}_{max}^{Pe=0}$, where $\mathcal{E}_{max}^{Pe=0}$ depends on the volume fraction (Figure 2.4). In the bistable region, we show the flow contribution for both stable phases at $Pe = 0$. Right column: The fraction of the total enhancement, \mathcal{E}_{max} , contributed by the flow-induced values \mathcal{E}_{Pe}^{iso} , \mathcal{E}_{Pe}^{nema} , respectively.

2.5.5 Illustrations

The scaling properties derived above will now be illustrated through graphs of the maximum relative conductivity enhancement (\mathcal{E}_{max}) versus volume fraction of the nano-composite, Figures 2.4, 2.5. The graphs are based on the general formula (2.17), and the scaling properties are validated against them. We present the properties of the composite in a hierarchy suggested by the decomposition scaling formulas (2.54), (2.55), (2.57), first (Figure 2.4) amplifying the transference of the classical I-N phase transition into electrical conductivity principal values, and then (Figures 2.5, 2.6) comparing the additional enhancement due to weak shear flow.

We will use polymer-CNT (carbon nanotube) composites as a model example, system II below, where the polymer matrix is typically non-conductive ($\sigma_1 \sim O(10^{-8})(\Omega \cdot \text{cm})^{-1}$), and the CNTs are extremely conductive ($\sigma_2 \sim O(10^4)(\Omega \cdot \text{cm})^{-1}$). In these model systems, $\sigma_1/\sigma_2 \sim O(10^{-12})$, whereas the typical aspect ratio of CNTs is $r = \frac{10^4 \sim 10^5 \text{ nm}}{1 \sim 50 \text{ nm}} \sim O(2 \times 10^2 \sim 10^5)$. From the formula (2.20), the geometry parameter L_a is then estimated as $L_a \sim O(10^{-4} \sim 10^{-9})$. These estimates imply polymer-CNT composites always lie in the regime $\frac{L_a}{\sigma_1/\sigma_2} \gg 1$, i.e. Case I, in all estimates of the previous section 2.5. We will illustrate the results of the formula (2.17) for two model systems: (I) $r = 100, \sigma_1/\sigma_2 = 10^{-5}$; (II) $r = 1000, \sigma_1/\sigma_2 = 10^{-10}$. The first system I is posited to compare enhancements when the aspect ratio and contrast are less extreme, yet still significant.

Figure 2.4 conveys that for quiescent phases, \mathcal{E}_{max} inherits hysteresis, bi-stability, and discontinuous jumps between the volume fractions θ_2^* where the nematic phase begins and θ_2^{**} where the isotropic phase becomes unstable. The predictions then fall into 3 intervals of volume fraction: $\theta_2 < \theta_2^*$; $\theta_2^* < \theta_2 < \theta_2^{**}$; and $\theta_2 > \theta_2^{**}$. For model system I, $\theta_2^* = 1.05\%, \theta_2^{**} = 1.18\%$, while for model system II, $\theta_2^* = 0.105\%, \theta_2^{**} = 0.118\%$.

For model system I, the maximum enhancement \mathcal{E}_{max} grows over interval 1 to 792% at θ_2^* , likewise grows over interval 3 from 1788% at θ_2^{**} to 3700% at 2% volume fraction. In the bi-stable isotropic and nematic interval $\theta_2^* < \theta_2 < \theta_2^{**}$, the isotropic phase enhancement grows from 792% to 895%, whereas the nematic phase enhancement begins at 1189% and increases to 1788%. Note the difference in \mathcal{E}_{max} between the bi-stable phases is significant: $\mathcal{E}_{max}^{nema} - \mathcal{E}_{max}^{iso}$ is 397% at θ_2^* and grows to 893% at θ_2^{**} .

For model system II, the maximum enhancement \mathcal{E}^{max} grows over interval 1 to 5274% at θ_2^* , likewise grows over interval 3 from 11900% at θ_2^{**} to 25000% at 0.2% volume fraction. In the bi-stable isotropic and nematic interval $\theta_2^* < \theta_2 < \theta_2^{**}$, the isotropic phase enhancement grows from 5274% to 5953%, whereas the nematic phase enhancement begins at 7924% and increases to 11900%. Note the difference $\mathcal{E}_{max}^{nema} - \mathcal{E}_{max}^{iso}$ between the bi-stable phases is 2650% at θ_2^* and grows to 6000% at θ_2^{**} .

Figure 2.5 shows that at the weak normalized shear rate $Pe = 0.1$, the hysteresis cycle has been pulled out, leaving a unique stable equilibrium phase for each volume fraction θ_2 . (The volume fraction interval 2 above of bi-stable phases is gone.) The corresponding \mathcal{E}_{max} for each equilibrium phase mirrors the monotonicity of the scalar order parameter S .

Figure 2.6 isolates the flow-induced contribution to \mathcal{E}_{max} for system I (top row) and II (bottom row). Both left figures show the flow-induced contribution \mathcal{E}_{Pe}^{iso} on the isotropic branch grows rapidly, whereas \mathcal{E}_{Pe}^{nema} , the nematic flow-induced contribution, is greatest at onset of the nematic phase, $\theta_2 = \theta_2^*$, and then rapidly falls off to negligible gain. The right figures provide the fraction $\mathcal{E}_{Pe}^{iso}/\mathcal{E}_{max}$ and $\mathcal{E}_{Pe}^{nema}/\mathcal{E}_{max}$ of the conductivity enhancement due specifically to the flow contribution. The figures are almost identical for system I and II, after accounting for the volume fraction scaling due to r . On the isotropic branch, the flow contribution ranges from 10% to 53%, whereas on the nematic branch, the range is 23% down to almost zero. These figures underscore that the gain due to flow has a peak, which suggests flow-induced gain can be optimized if these scaling features persist into more general processing regimes.

2.5.6 Conclusion

We have derived $\Sigma_{\theta_2}^e$, the effective electrical conductivity tensor, in explicit form for nanocomposites with volume fraction θ_2 of nematic polymers with matrix conductivity σ_1 and nano-inclusion conductivity σ_2 . This result is based on volume averaging over an arbitrary orientational probability distribution of monodisperse, spheroidal molecular inclusions. The formula encodes both quiescent and weak shear bulk phases through the second moment tensor of the orientational PDF; all higher moments of the PDF are rigorously shown to not enter $\Sigma_{\theta_2}^e$ at leading order in θ_2 .

We then infer an explicit decomposition of the *conductivity enhancement* \mathcal{E} (associated with the maximum principal value of $\Sigma_{\theta_2}^e$) into contributions \mathcal{E}^{iso} of the isotropic phase, \mathcal{E}^{nema} of the nematic phase, and \mathcal{E}_{Pe} of the shear-induced isotropic or nematic phase:

$$\mathcal{E} = \mathcal{E}^{iso} + \mathcal{E}^{nema} + \mathcal{E}_{Pe}. \quad (2.60)$$

The directions and degrees of anisotropy are also characterized. Refined scaling laws are then determined depending on the relative size of two independent large parameters in nematic polymer nano-composites, the molecular aspect ratio r and the conductivity contrast σ_2/σ_1 .

Key features of the analysis are :

- The conductivity enhancement inherits the hysteresis of the isotropic-nematic phase diagram. That is, \mathcal{E}^{nema} is a dominant contribution that emerges spontaneously at the critical volume fraction $\theta_2 = \theta_2^*$ of the I-N transition. The analogy with a percolation threshold is compelling, and will be addressed elsewhere.
- The high conductivity contrast $\sigma_2/\sigma_1 \gg 1$ and high molecule aspect ratio $r \gg 1$ are sufficient to overwhelm the low volume fraction $\theta_2 \ll 1$. For typical CNT composites, we predict conductivity enhancements on the order of 1000-10,000 %. These extreme gains are greater than those reported in experimental systems, compelling the incorporation of additional effects as noted below.
- The principal axes of $\Sigma_{\theta_2}^e$ follow those of the second moment \mathbf{M} of the nano-inclusion orientational distribution function $f(\mathbf{m})$, a rigorous consequence of our main formula (2.17), which is intuitively natural.
- These results for bulk homogenous mesophases of nematic polymer nano-composites lay the groundwork for extensions to heterogeneity, (i.e. ensembles of local mesophases with confinement and flow-induced spatial structures), more general flow rates and flow type, and the incorporation of effects of the “interphase” between the matrix and nano-inclusions.

2.6 Applications II: Anisotropy and dynamic ranges in effective properties of sheared nematic polymer nano-composites

In this section, we consider typical model NPNCs with the nematogen aspect ratio is $r = 200$ (and one figure with $r = 50$ for comparison). For $r = 200$, the perfactor L_a in (2.15), is $O(10^{-4})$; for $r = 50$, L_a is 10^{-3} . We specify the conductivity contrast between the nano phase and the matrix solvent as $\sigma_2/\sigma_1 = 10^6$. These specifications obey the inequality $L_a \gg (\sigma_1/\sigma_2)$, in which case the scaling law in Zheng *et al.* (2005) yields a simplified estimate for the effective conductivity tensor, (2.22):

$$\Sigma^e \approx \sigma_1(\mathbf{I} + \frac{\theta_2}{L_a}\mathbf{M}), \quad \mathcal{E}_j \approx \frac{\theta_2}{L_a}d_j, j = 1, 2, 3. \quad (2.61)$$

Recall d_j are the three eigenvalues of \mathbf{M} , $0 \leq d_j \leq 1$. We now appeal to the “monodomain phase diagram” of Doi-Hess kinetic theory, as developed in 1.5 (Forest *et al.*, 2004a,b).

We proceed now to sample from within Regions in (θ_2, Pe) where each of these attracting sheared responses occur, and extract the important effective conductivity features from the analytical framework described in Section 2.3.

2.6.1 Conductivity enhancement of NPNCs at steady state

For flow-aligned (FA) states, Figure 2.7 shows the peak axis (Leslie alignment angle) of the steady PDF and maximum scalar conductivity enhancement (\mathcal{E}_{max}), versus Peclet number Pe for three different volume fractions θ_2 . These correspond to slices of the Region I in (Forest *et al.*, 2004b) at $N = 4.7, 5.5, 6$ ($\theta_2 = 0.92\%, 1.08\%, 1.26\%$ with $r = 200$, $\theta_2 = 3.69\%, 4.32\%, 5.03\%$ with $r = 50$). (At rest, each nematic liquid is isotropic at lowest volume fraction, and nematic at the other two.) Note that as the volume fraction increases, so does the shear rate required to induce steady alignment. The primary result from Figure 1b is the prediction that the maximum scalar conductivity σ_{max}^e of the NPNC monodomain is on the order of 50 – 75 times the isotropic matrix conductivity σ_1 . Thus, for these sheared composites, one captures 2 orders of magnitude gain at these extremely low volume fractions, from the upper limit of 6 orders of magnitude in property contrast: $\sigma_2/\sigma_1 = 10^6$.

The second result for these FA steady states from Fig. 2.7 is that $\partial\mathcal{E}_{max}/\partial Pe \approx 0.2$ for $r = 200$, so that there is a considerable benefit to \mathcal{E}_{max} in shearing near the highest shear rate of stability of these FA states. If we lower the aspect ratio to $r = 50$, then $\partial\mathcal{E}_{max}/\partial Pe \approx 0.06$, so the enhancement due to increased shear rate is quite weak. At higher θ_2 or N , which require higher Pe to stabilize the FA phase, one finds an additional 20 – 50% rise in \mathcal{E}_{max} for both aspect ratios. Comparing the two figures 2.7(b) and 2.7(c) with different aspect ratios and the same normalized concentration N , the lower aspect ratio corresponds to higher volume fraction, and consistent with the scaling law (2.61), the relative enhancement drops by 2/3. We can conclude that aspect ratio is a dominant factor in controlling the effective electrical conductivity. For the remaining simulations and Figures, we restrict to $r = 200$.

Figure 2.8 shows the major enhancement for steady logrolling (LR) states, for which the principal axis \mathbf{n}_1 lies along the flow vorticity direction, and \mathbf{n}_2 lies in the flow-flow gradient plane. As volume fraction increases, the Pe window of stable LR states widens, by contrast with Fig. 2.7 and FA states. We again give results for three concentrations versus shear rate. The maximum scalar conductivity σ_{max}^e of logrolling NPNC monodomain distribution functions is on the order of 68 – 78 times the matrix conductivity σ_1 . These enhancements are slightly greater ($\sim 10\%$) than FA steady distributions at comparable volume fractions, and these PDFs are achievable at significantly lower shear rates. We note further from Figure 2.8 that $\partial\mathcal{E}_{max}/\partial Pe \approx -0.5$, so that it is advantageous to operate near the lowest stable shear rates for LR states at a given volume fraction.

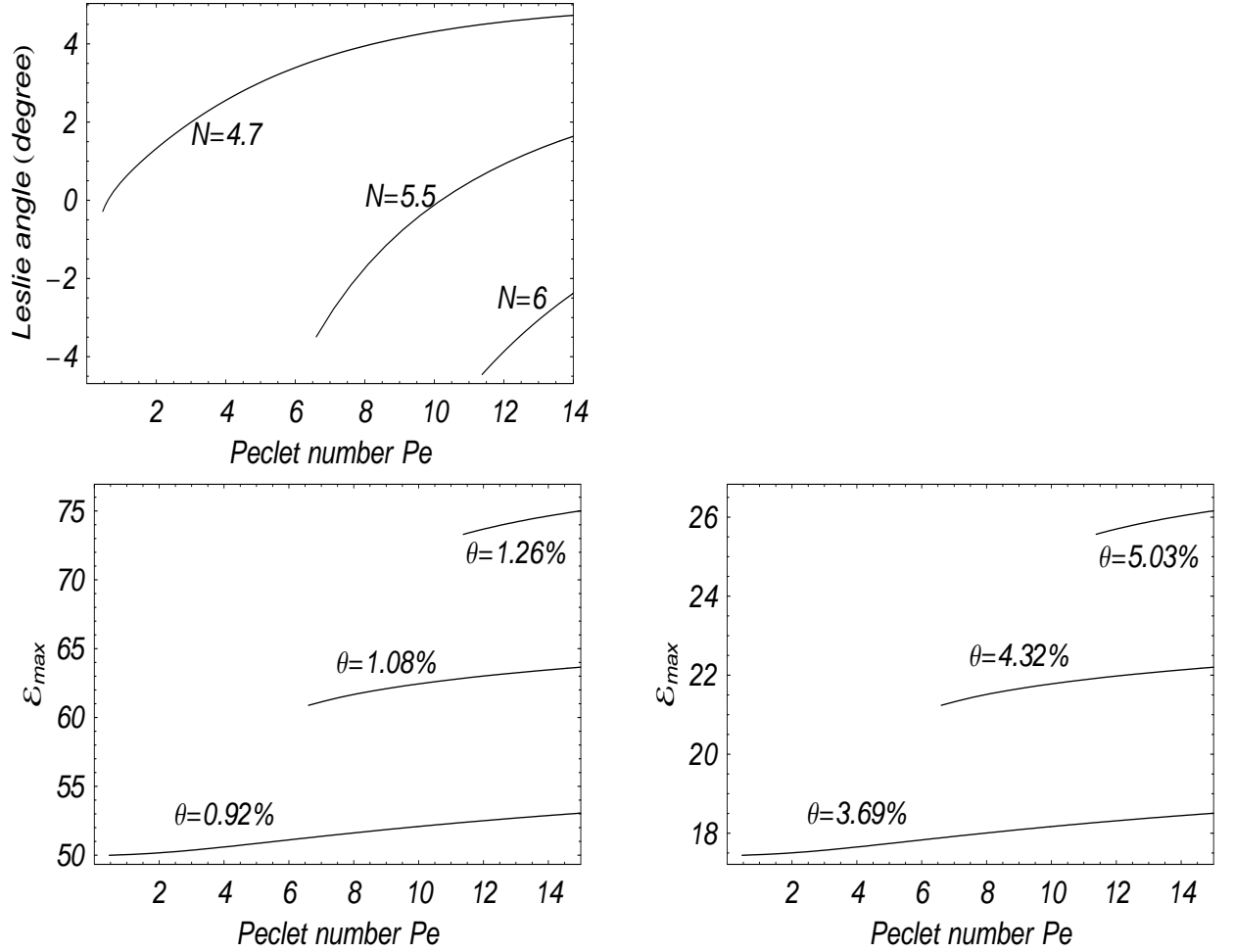


Figure 2.7: Peak alignment angle (figure a) and maximum scalar conductivity enhancement (b,c) for families of flow-aligned steady states at normalized concentrations for $N = 4.7, 5.5, 6$, respectively, volume fractions $\theta_2 = 0.92\%, 1.08\%, 1.26\%$ corresponding to $r = 200$ (figure b) and $\theta_2 = 3.69\%, 4.32\%, 5.03\%$ for $r = 50$ (figure c). These states exist and are stable over the indicated ranges of normalized shear rate (Pe).

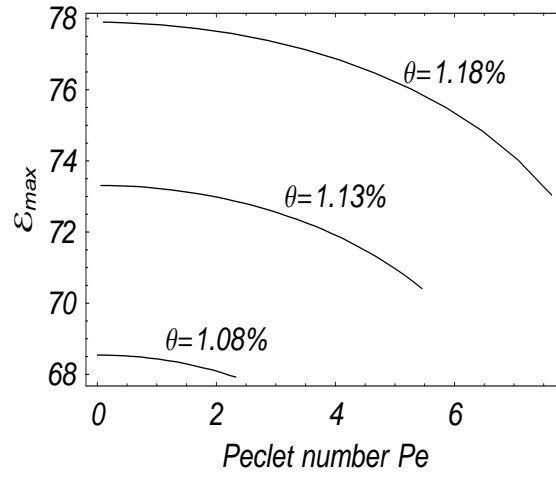


Figure 2.8: Maximum scalar conductivity enhancements for steady logrolling states at concentrations $N = 5.5, 5.75, 6$, respectively, volume fractions $\theta_2 = 1.08\%, 1.13\%, 1.18\%$ with aspect ratio $r = 200$ over the range of normalized shear rates (Pe) where these states are stable.

2.6.2 Dynamic and anisotropy of property enhancement for periodic attractors

Figure 2.9 shows the *dynamic property fluctuations* of tumbling (T) and wagging (W) stable sheared responses at volume fraction $\theta_2 = 1.08\%$ ($N = 5.5$). The maximum scalar conductivity σ_{max}^e is on the order of 35–75 times the matrix conductivity σ_1 ; recall the conductivity contrast is $\sigma_2/\sigma_1 = 10^6$. The horizontal axis shows the large dynamic range of the maximum effective conductivity,

$$\frac{\max \mathcal{E}_1(t)}{\min \mathcal{E}_1(t)} \approx \begin{cases} 1.5 & \text{for W orbits} \\ 2 & \text{for T orbits;} \end{cases} \quad (2.62)$$

the vertical axis, $\mathcal{E}_1(t) - \mathcal{E}_2(t)$, shows the high degree and large dynamic range of anisotropy.

$$\frac{\max(\mathcal{E}_1(t) - \mathcal{E}_2(t))}{\min(\mathcal{E}_1(t) - \mathcal{E}_2(t))} \approx \begin{cases} 4 & \text{for W orbits} \\ 8 & \text{for T orbits.} \end{cases} \quad (2.63)$$

The tumbling attractor transitions to wagging as the shear rate increases at these volume fractions.

Figure 2.10 shows the corresponding results for the oscillatory kayaking state (K_1) whose peak orientation rotates about the vorticity axis with volume fraction $\theta_2 = 1.02\%$ ($N = 5.2$) and shear rate $Pe = 3$. The maximum scalar conductivity σ_{max}^e is on the order 59–62 times the matrix conductivity σ_1 . The horizontal axis shows a smaller dynamic range of \mathcal{E}_1 than tumbling or wagging phases, with:

$$\frac{\max \mathcal{E}_1(t)}{\min \mathcal{E}_1(t)} \approx 1.05. \quad (2.64)$$

The vertical axis, $\mathcal{E}_1 - \mathcal{E}_2$, shows large anisotropy of the effective conductivity Σ^e with relatively small dynamic range:

$$\frac{\max(\mathcal{E}_1(t) - \mathcal{E}_2(t))}{\min(\mathcal{E}_1(t) - \mathcal{E}_2(t))} \approx 1.1. \quad (2.65)$$

Figure 2.11 shows corresponding results for the tilted kayaking limit cycle (K_2), at slightly higher volume fraction $\theta_2 = 1.08\%$ and $Pe = 6$. In this case the maximum scalar conductivity

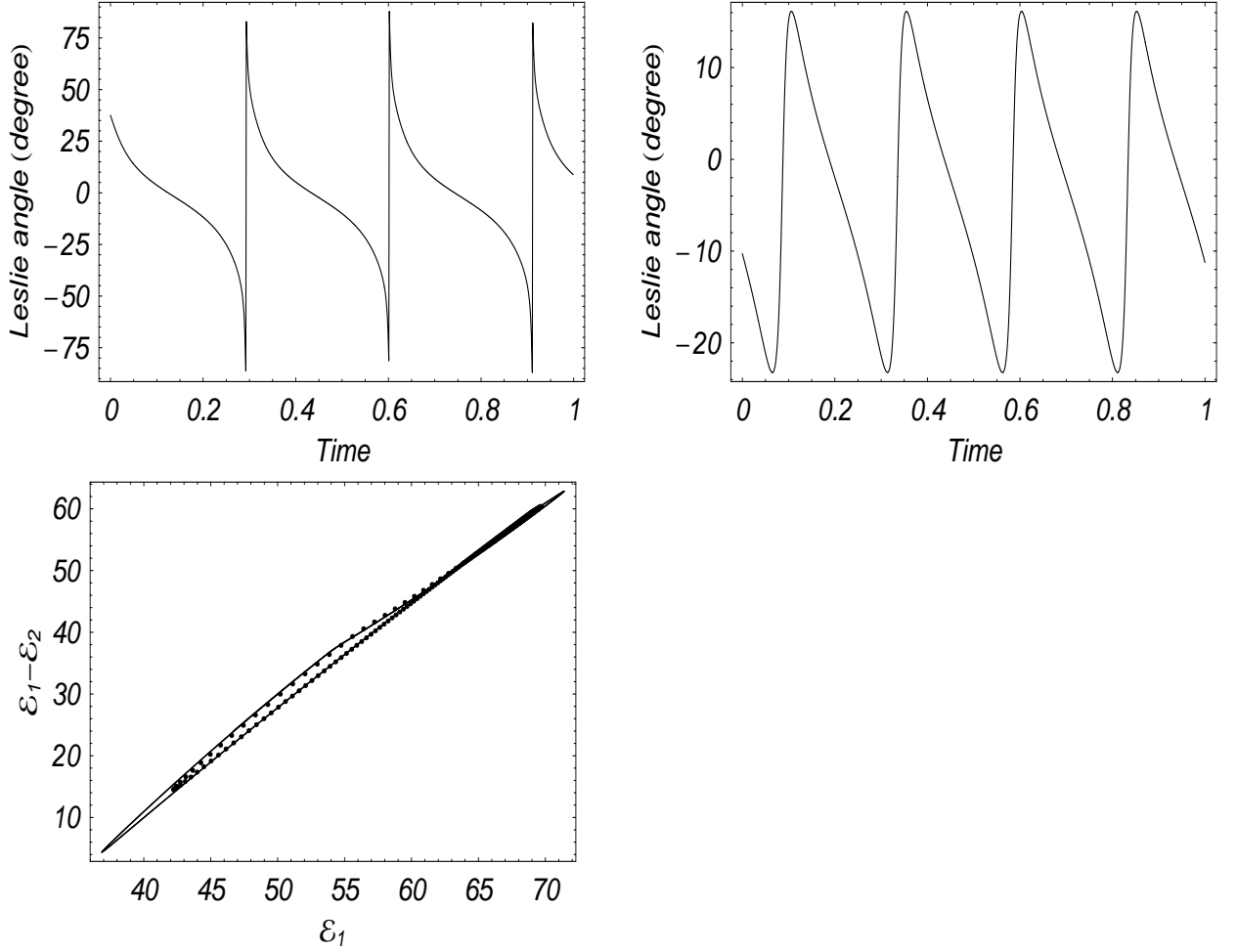


Figure 2.9: Dynamic ranges at low volume fraction $\theta_2 = 1.08\%$ ($N = 5.5, r = 200$) of the peak alignment direction for tumbling (top left, $Pe = 3.4$) and wagging (top right, $Pe = 4$) sheared monodomains; and (bottom) corresponding *maximum scalar effective conductivity enhancement* \mathcal{E} , and *effective conductivity anisotropy measure* $\mathcal{E}_1 - \mathcal{E}_2$, where tumbling values are solid and wagging values are dotted.

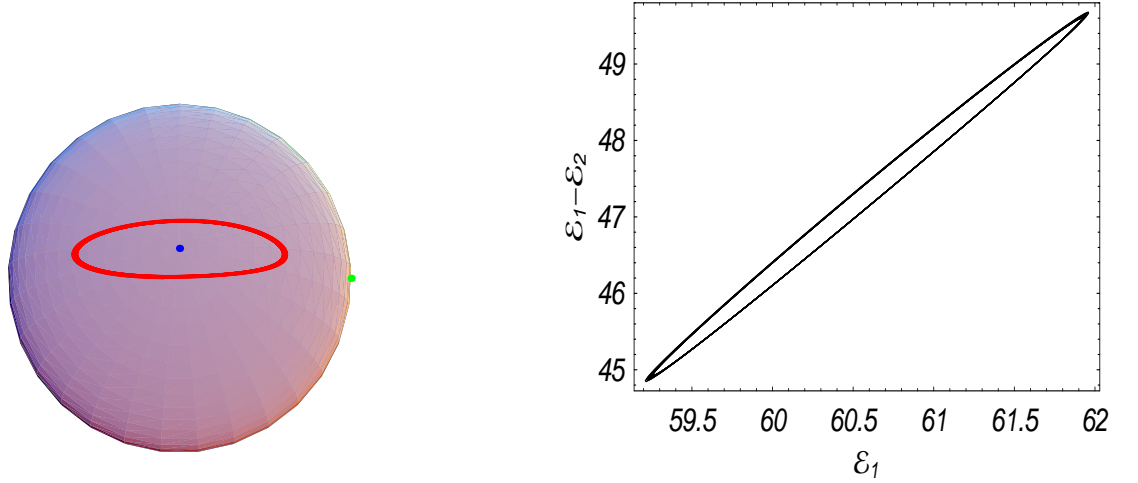


Figure 2.10: (Left) Dynamics of the peak orientation of the PDF around the vorticity axis (the dot in the middle), and (right) the dynamic ranges of \mathcal{E}_1 and $\mathcal{E}_1 - \mathcal{E}_2$, for a typical kayaking limit cycle (K_1) at normalized shear rate $Pe = 3$, and normalized rod concentration $N = 5.2$, achieved for volume fraction $\theta_2 = 1.02\%$ with $r = 200$.

σ_{max}^e is on the order 55 – 64 times the matrix conductivity σ_1 . The horizontal axis shows a larger dynamic range of \mathcal{E}_1 compared to the K_1 state of Figure 2.10,

$$\frac{\max \mathcal{E}_1(t)}{\min \mathcal{E}_1(t)} \approx 1.16, \quad (2.66)$$

and the vertical axis of $\mathcal{E}_1 - \mathcal{E}_2$ shows less but still significant anisotropy of the effective conductivity Σ^e and large dynamic range,

$$\frac{\max(\mathcal{E}_1(t) - \mathcal{E}_2(t))}{\min(\mathcal{E}_1(t) - \mathcal{E}_2(t))} \approx 1.5. \quad (2.67)$$

The analogous results for chaotic orientational sheared responses is shown in Figure 2.12, with volume fraction $\theta_2 = 1.02\%$ ($N = 5.2$) and Peclet number $Pe = 4.044$. The maximum scalar conductivity σ_{max}^e is on the order 35 – 65 times the matrix conductivity σ_1 . The horizontal axis shows the largest dynamic range of \mathcal{E}_1 for all states,

$$\frac{\max \mathcal{E}_1(t)}{\min \mathcal{E}_1(t)} \approx 1.85, \quad (2.68)$$

and the vertical axis of $\mathcal{E}_1 - \mathcal{E}_2$ shows large anisotropy of the effective conductivity Σ^e with

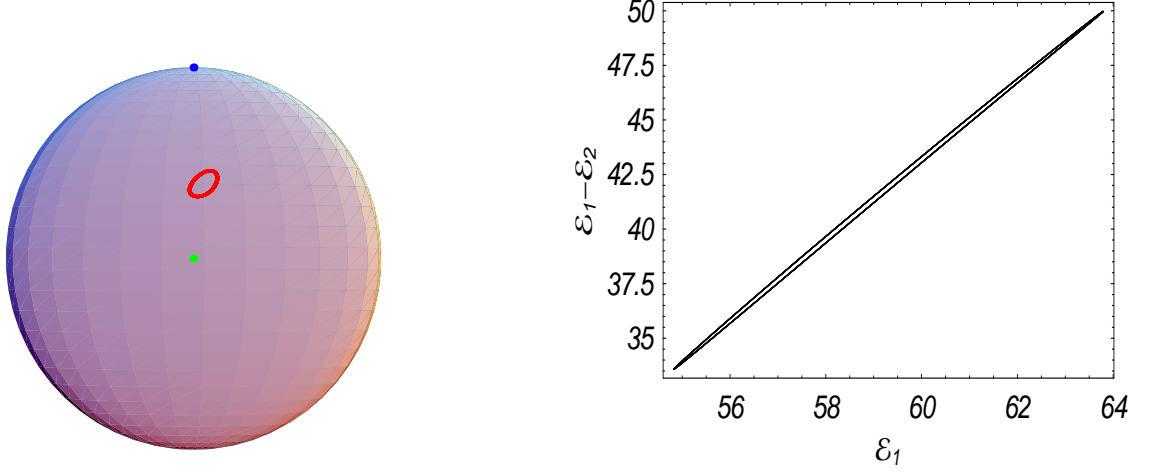


Figure 2.11: (Left) Dynamics of the peak orientation axis of the PDF around the vorticity axis (the dot in the middle), and (right) the dynamic ranges of \mathcal{E}_1 and $\mathcal{E}_1 - \mathcal{E}_2$ for a typical tilted kayaking state (K_2) at higher shear rate $Pe = 6$, normalized concentration $N = 5.5$, achieved by volume fraction $\theta_2 = 1.08\%$ with nano-rod aspect ratio $r = 200$.

huge dynamic fluctuations,

$$\frac{\max(\mathcal{E}_1(t) - \mathcal{E}_2(t))}{\min(\mathcal{E}_1(t) - \mathcal{E}_2(t))} \approx 26.0. \quad (2.69)$$

Finally, we give the effective property analog of a bifurcation diagram in time-averaged, maximum enhancement \mathcal{E}_{max} of the effective conductivity tensor Σ^e versus normalized shear rate Pe for fixed normalized concentration $N = 5.2$, corresponding to volume fraction $\theta_2 = 1.02\%$. These bifurcation diagrams are now standard in the rheology literature on sheared nematic polymer monodomains, where typically the vertical axis is the amplitude of projection of the PDF onto one spherical harmonic. The diagrams show the effective property transitions versus shear rate (Pe) between the various stable (solid curves) and unstable (dashed curves) sheared response modes of the NPNC. For this specific volume fraction, this "property bifurcation diagram" shows the kayaking state (K_1) attains the maximum enhancement. The diagram also shows the maximum effective conductivity is increasing with shear rate for stable K_1 and FA states, yet decreasing for LR, T, W, and K_2 states. Furthermore, when the K_1 branch is lost at the indicated Pe , the new stable state (K_2) acquires a discontinuous drop in \mathcal{E}_{max} ! This result, in nonlinear physics parlance on sheared nematic polymer liquids, is a first-order phase transition, a shear-induced analog of the isotropic-nematic phase transition.

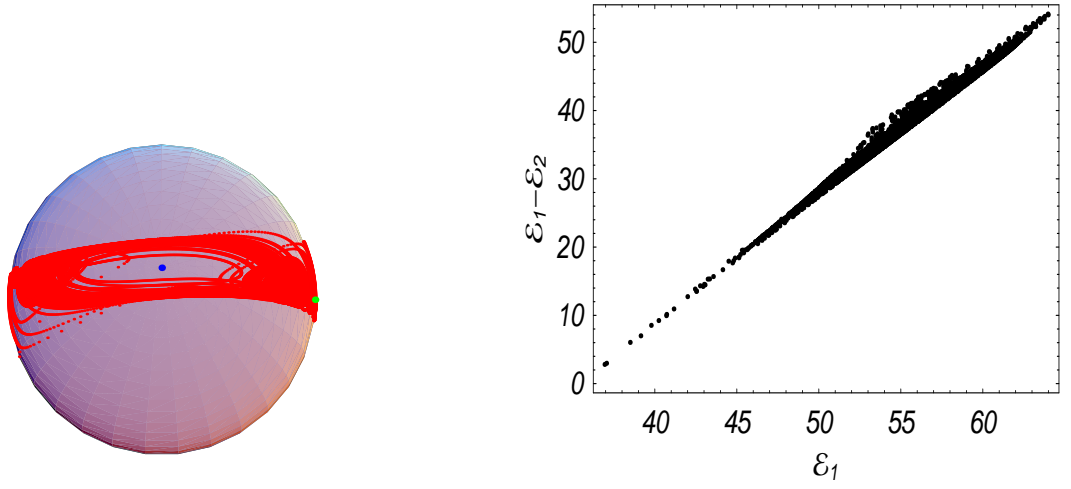


Figure 2.12: (Left) Chaotic orbit of the peak orientation axis of PDF at moderate shear rate $Pe = 4.044$ and normalized concentration $N = 5.2$ ($\theta_2 = 1.02\%$ for $r = 200$). (Right) The dynamics ranges of \mathcal{E}_1 and $\mathcal{E}_1 - \mathcal{E}_2$ for the chaotic monodomain PDF attractor on the left.

The message here is that property tensors inherit these phase transitions!

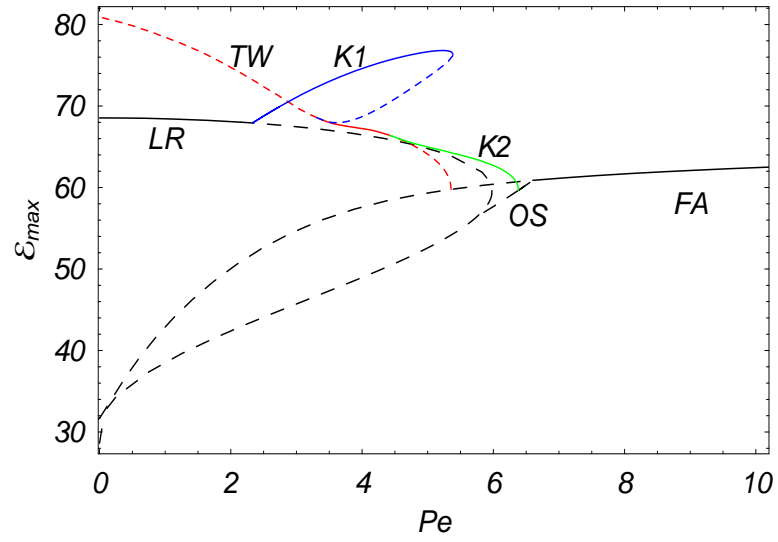


Figure 2.13: “Property bifurcation diagram” of maximum conductivity enhancement \mathcal{E}_{max} versus normalized shear rate Pe at fixed normalized concentration $N = 5.5$, achieved by $\theta_2 = 1.02\%$ for $r = 200$. The vertical axis is the time-averaged, maximum principal value, \mathcal{E}_{max} , of the effective conductivity tensor Σ^e , for each stable (solid curves) and unstable (dashed) sheared monodomain response over this entire range of shear rates (Pe).

2.6.3 Conclusion

Sheared monodomains of high aspect ratio nematic polymers in viscous solvents are modeled by the Doi-Hess kinetic theory, which yields the orientational probability distribution function versus volume fraction and shear rate. Numerical databases for these distribution functions (Forest *et al.*, 2004a,b) are implemented in homogenization formulas (Zheng *et al.*, 2005) for the effective conductivity tensor Σ^e , given the volume fractions θ_1 , θ_2 and scalar conductivities σ_1 , σ_2 of the matrix solvent and nematic polymer nano phase, respectively. We have illustrated typical gains and dynamic fluctuations in both maximum conductivity and anisotropy for steady and unsteady sheared monodomain distribution functions. From these predictions, we also give relative comparisons. These results suggest that there is a clear potential in using tools such as these to optimize or control property gains in NPNCs. The next step in this program is to allow for heterogeneity. Typical films are textured, i.e. a heterogeneous mixture of monodomains mediated by defects, so results herein represent building blocks for macroscopic film property characterization.

Chapter 3

Anisotropic Elastic Moduli of Quiescent and Sheared NPNCs

3.1 Introduction

In this chapter, we model and compute effective mechanical properties of nano-composite monodomains, consisting of nematic polymer macromolecules (transversely isotropic spheroids) in an isotropic matrix. Both phases are endowed with linear elasticity properties to make contact with theoretical results on random and perfectly aligned spheroidal composites (Odegard *et al.* (2003), Gusev *et al.* (2002), Torquato (2002), Milton (2002)) and with experimental data (Odegard *et al.* (2003)). We predict the degree of enhancement and anisotropy in elastic moduli, arising from extremely stiff spheroidal inclusions at low volume fractions, for quiescent and sheared bulk monodomains. We allow the nano-particles to have transversely isotropic mechanical properties, since many nano-rods and nano-platelets have high contrast modulus along vs. transverse to their axis of symmetry. The key modeling contribution in this chapter is that we inject symmetries and numerical databases for the orientational probability distribution function (PDF) of the nematic polymer ensemble into the classical Mori-Tanaka effective elasticity tensor (EET) formalism. Intuitive symmetries of effective elasticity tensors are rigorously established from PDF symmetries (Forest *et al.* (2002b)), which then determine the number of independent moduli versus volume fraction and imposed flow type and strength (e.g. isotropic, transversely isotropic and monoclinic). Analogous to effective conductivity properties (Zheng *et al.* (2005), Forest *et al.* (2005)), we show that bistable dispersions as well as first- and second- order phase transitions in PDF phase diagrams translate to similar mechanical property phenomena.

3.1.1 Stress-strain relations

Throughout the chapter, we use Greek letters (e.g. τ, ε) to denote a second order tensor, capital letters (e.g. C, I, S) to denote a fourth order tensor, and lower case letters (e.g. n, t, x) to denote a vector or scalar.

Let $u(x)$ denote the displacement, $\tau(x)$ and $\varepsilon(x)$ denote the symmetric local stress and strain tensors at position x . In steady states without sources, $\tau(x)$ and $\varepsilon(x)$ satisfy (cf. Torquato (2002)):

$$\nabla \cdot \tau(x) = 0, \quad \nabla \times (\nabla \times \varepsilon)^T = 0, \quad (3.1)$$

which means the strain can be written as a symmetrized gradient of displacements $u(x)$,

$$\varepsilon(x) = \frac{1}{2}[\nabla u(x) + \nabla u(x)^T]. \quad (3.2)$$

The linear elastic constitutive law is

$$\tau(x) = C(x) : \varepsilon(x), \quad \varepsilon(x) = M(x) : \tau(x), \quad (3.3)$$

where fourth order tensors C and M are the local stiffness and compliance tensor with

$$C : M = I, \quad I = \frac{1}{2}[\delta_{ik}\delta_{jl} + \delta_{il}\delta_{jk}], \quad (3.4)$$

and I is the fourth order identity tensor.

We are concerned here with 2-phase composites, consisting of a nano-particle phase of rods or platelets and a matrix phase. Each phase satisfies (3.1)-(3.3) with distinct, and often highly contrasted, stiffness tensors. From classical homogenization theory, the composite satisfies a form of (3.3), but with averaged stress, strain and effective stiffness tensor C^e :

$$\langle \tau(x) \rangle = C^e : \langle \varepsilon(x) \rangle, \quad (3.5)$$

under the assumption that the phases are perfectly bonded.

3.1.2 Stiffness tensor and elastic moduli

Since the stress tensor and strain tensor are symmetric, we must have

$$C_{ijkl} = C_{jikl}, \quad C_{ijkl} = C_{ijlk}. \quad (3.6)$$

This reduces the 81 independent components of C_{ijkl} to 36 for three-dimensional elasticity. It is traditional (Torquato (2002)) to retain the label C for the 6 by 6 matrix representation of these 36 stiffness constants. Likewise, the stress and strain tensors are compressed into 6-dimensional vectors so that (3.3) reduces to:

$$\begin{pmatrix} \tau_1 \\ \tau_2 \\ \tau_3 \\ \tau_4 \\ \tau_5 \\ \tau_6 \end{pmatrix} = \begin{pmatrix} C_{11} & C_{12} & C_{13} & C_{14} & C_{15} & C_{16} \\ C_{12} & C_{22} & C_{23} & C_{24} & C_{25} & C_{26} \\ C_{13} & C_{23} & C_{33} & C_{34} & C_{35} & C_{36} \\ C_{14} & C_{24} & C_{34} & C_{44} & C_{45} & C_{46} \\ C_{15} & C_{25} & C_{35} & C_{45} & C_{55} & C_{56} \\ C_{16} & C_{26} & C_{36} & C_{46} & C_{56} & C_{66} \end{pmatrix} \begin{pmatrix} \varepsilon_1 \\ \varepsilon_2 \\ \varepsilon_3 \\ \varepsilon_4 \\ \varepsilon_5 \\ \varepsilon_6 \end{pmatrix}, \quad (3.7)$$

with the following identification:

$$\begin{aligned} \tau_i &= \tau_{ii}, \text{ for } i = 1, 2, 3, \tau_4 = \tau_{23}, \tau_5 = \tau_{13}, \tau_6 = \tau_{12}, \\ \varepsilon_i &= \varepsilon_{ii}, \text{ for } i = 1, 2, 3, \varepsilon_4 = 2\varepsilon_{23}, \varepsilon_5 = 2\varepsilon_{13}, \varepsilon_6 = 2\varepsilon_{12}; \end{aligned} \quad (3.8)$$

while the identification C_{ijkl} and C_{pq} is:

$$11 \leftrightarrow 1, 22 \leftrightarrow 2, 33 \leftrightarrow 3, 23(32) \leftrightarrow 4, 13(31) \leftrightarrow 5, 12(21) \leftrightarrow 6. \quad (3.9)$$

If the stress can be expressed as a derivative of the strain energy density function with respect to strain, then the stiffness tensor must additionally have the symmetry

$$C_{ijkl} = C_{klij}, \quad (3.10)$$

which further reduces the independent elastic constants to 21. If certain symmetries exist in

the material, this number will be reduced even further as follows.

Monoclinic symmetry

With symmetry with respect to one plane, say the x_1 - x_2 plane, the elasticity tensor has 13 independent components:

$$C = \begin{pmatrix} C_{11} & C_{12} & C_{13} & 0 & 0 & C_{16} \\ C_{12} & C_{22} & C_{23} & 0 & 0 & C_{26} \\ C_{13} & C_{23} & C_{33} & 0 & 0 & C_{36} \\ 0 & 0 & 0 & C_{44} & C_{45} & 0 \\ 0 & 0 & 0 & C_{45} & C_{55} & 0 \\ C_{16} & C_{26} & C_{36} & 0 & 0 & C_{66} \end{pmatrix}. \quad (3.11)$$

As in the general anisotropic case, here pure strain can give rise to a normal stress.

Orthotropic symmetry

For symmetry with respect to three orthogonal planes, or alternately three orthogonal symmetry axes, the elasticity tensor has 9 independent components. The elasticity tensor in coordinates aligned with principal material directions is:

$$C = \begin{pmatrix} C_{11} & C_{12} & C_{13} & 0 & 0 & 0 \\ C_{12} & C_{22} & C_{23} & 0 & 0 & 0 \\ C_{13} & C_{23} & C_{33} & 0 & 0 & 0 \\ 0 & 0 & 0 & C_{44} & 0 & 0 \\ 0 & 0 & 0 & 0 & C_{55} & 0 \\ 0 & 0 & 0 & 0 & 0 & C_{66} \end{pmatrix}. \quad (3.12)$$

It is convenient to relate the elastic components to engineering moduli, respectively called Young's moduli E_1, E_2, E_3 in the 1-, 2- and 3- directions; Poisson's ratios $\nu_{12}, \nu_{13}, \nu_{23}$, which are defined by the negative of the transverse strain in the j -direction over the strain in the i -direction when stress is applied in the i -direction, and shear moduli G_{12}, G_{13}, G_{23} in the 1-

2, 1-3 and 2-3 planes. The correspondences between the elastic components and engineering moduli are:

$$\begin{aligned}
C_{11} &= E_1(1 - (E_3/E_2)\nu_{23}^2)D, & C_{12} &= (E_2\nu_{12} + E_3\nu_{13}\nu_{23})D, \\
C_{13} &= E_3(\nu_{12}\nu_{23} + \nu_{13})D, & C_{22} &= E_2(1 - (E_3/E_1)\nu_{13}^2)D, \\
C_{23} &= (E_3/E_1)(E_1\nu_{23} + E_2\nu_{12}\nu_{13})D, & C_{33} &= E_3(1 - (E_2/E_1)\nu_{12}^2)D, \\
C_{44} &= G_{23}, & C_{55} &= G_{13}, & C_{66} &= G_{12},
\end{aligned} \tag{3.13}$$

with

$$D^{-1} = 1 - 2(E_3/E_1)\nu_{12}\nu_{23}\nu_{13} - \nu_{13}^2(E_3/E_2) - \nu_{23}^2(E_3/E_2) - \nu_{12}^2(E_2/E_1). \tag{3.14}$$

The compliance tensor M can be expressed in terms of the independent moduli:

$$M = \begin{pmatrix} \frac{1}{E_1} & -\frac{\nu_{21}}{E_2} & -\frac{\nu_{31}}{E_3} & 0 & 0 & 0 \\ -\frac{\nu_{12}}{E_1} & \frac{1}{E_2} & -\frac{\nu_{32}}{E_3} & 0 & 0 & 0 \\ -\frac{\nu_{13}}{E_1} & -\frac{\nu_{23}}{E_2} & \frac{1}{E_3} & 0 & 0 & 0 \\ 0 & 0 & 0 & \frac{1}{4G_{23}} & 0 & 0 \\ 0 & 0 & 0 & 0 & \frac{1}{4G_{13}} & 0 \\ 0 & 0 & 0 & 0 & 0 & \frac{1}{4G_{12}} \end{pmatrix}, \tag{3.15}$$

with $\frac{\nu_{ij}}{E_i} = \frac{\nu_{ji}}{E_j}$.

Transversely isotropic symmetry

For symmetry with respect to one axis, the elasticity tensor has 5 independent constants. For example, if the symmetry axis is the $x_1 = (1, 0, 0)$ axis, then the stiffness tensor can be

expressed by:

$$C = \begin{pmatrix} C_{11} & C_{12} & C_{12} & 0 & 0 & 0 \\ C_{12} & C_{22} & C_{23} & 0 & 0 & 0 \\ C_{12} & C_{23} & C_{22} & 0 & 0 & 0 \\ 0 & 0 & 0 & 1/2(C_{22} - C_{23}) & 0 & 0 \\ 0 & 0 & 0 & 0 & C_{66} & 0 \\ 0 & 0 & 0 & 0 & 0 & C_{66} \end{pmatrix}. \quad (3.16)$$

The 5 engineering moduli are longitudinal (E_L) and transverse (E_T) Young's moduli, transverse bulk modulus (k_T), longitudinal (G_L) and transverse (G_T) shear moduli. The components of the stiffness tensor are traditionally labeled according to:

axial modulus under an axial strain	$n = C_{11}$
transverse bulk modulus	$k_T = (C_{22} + C_{23})/2$
cross modulus	$l = C_{12}$
longitudinal Young's modulus	$E_L = n - l^2/k_T$
transverse shear modulus	$G_T = (C_{22} - C_{23})/2$
longitudinal shear modulus	$G_L = C_{66}$
Poisson's ratio	$\nu_{12} = l/(2k_T)$

Isotropic symmetry

When the elastic moduli are invariant under coordinate transformations, there are only two independent elastic moduli, and C has the representation

$$C = \begin{pmatrix} C_{11} & C_{12} & C_{12} & 0 & 0 & 0 \\ C_{12} & C_{11} & C_{12} & 0 & 0 & 0 \\ C_{12} & C_{12} & C_{11} & 0 & 0 & 0 \\ 0 & 0 & 0 & 1/2(C_{11} - C_{12}) & 0 & 0 \\ 0 & 0 & 0 & 0 & 1/2(C_{11} - C_{12}) & 0 \\ 0 & 0 & 0 & 0 & 0 & 1/2(C_{11} - C_{12}) \end{pmatrix}, \quad (3.17)$$

where $C_{12} = \lambda$ is the Lamé constant, $1/2(C_{11} - C_{12}) = G$ is the shear modulus, and $K = \lambda + \frac{2}{3}G$ is the bulk modulus governing volumetric and dilatational changes. The isotropic elasticity and compliance tensors can also be expressed using indicial notation:

$$\begin{aligned} C_{ijkl} &= (K - \frac{2}{3}G)\delta_{ij}\delta_{kl} + G(\delta_{ik}\delta_{jl} + \delta_{il}\delta_{jk}), \\ M_{ijkl} &= (\frac{1}{9K} - \frac{1}{6G})\delta_{ij}\delta_{kl} + \frac{1}{4G}(\delta_{ik}\delta_{jl} + \delta_{il}\delta_{jk}). \end{aligned} \quad (3.18)$$

The relationships between the shear modulus G , Young's modulus E and bulk modulus K , transversely bulk modulus k_T are given by

$$G = \frac{E}{2(1 + \mu)}, \quad K = \frac{E}{3(1 - 2\mu)}, \quad k_T = K + G/3. \quad (3.19)$$

3.2 Effective stiffness tensors

3.2.1 Low volume fraction expansion vs. Mori-Tanaka theory

Considering a perfect bond between the inclusions and matrix, the effective stiffness tensor of a dilute (low volume fraction θ_2) suspension is given by Hill (1964):

$$C^e = C_1 + \theta_2 \langle N \rangle + O(\theta_2^2), \quad (3.20)$$

$$N = (C_2 - C_1) : T, \quad T = [I + S : C_1^{-1} : (C_2 - C_1)]^{-1}, \quad \langle \cdot \rangle = \int_{S^2} \cdot f d\mathbf{m}, \quad (3.21)$$

where C_1 and C_2 are stiffness tensors for the matrix and inclusion; S is the Eshelby tensor for an ellipsoidal inclusion embedded in an isotropic matrix with Poisson ratio ν_1 ; N is the polarization tensor, T is the Wu strain tensor (c.f. Torquato (2002)), and f is the orientational PDF of the inclusions.

The effective stiffness tensor for composites approximated by Mori-Tanaka theory is given by

$$C^e = C_1 + \theta_2 \langle N \rangle : (\theta_1 I + \theta_2 \langle T \rangle)^{-1}. \quad (3.22)$$

This formula purports to account for interactions between the inclusions and matrix and

is assumed to be valid for any volume fraction θ_2 . The low volume fraction limit of Hill (1964) is based on a unit the cell problem with one inclusion.

The computation of the tensor C^e is straightforward yet tedious. Since S and C_2 are transversely isotropic, and C_1 is isotropic, we can use standard rules for the inner products of tensors given below in Section 3.2.3.

3.2.2 Eshelby tensor S

For a spheroidal inclusion embedded in a matrix with Poisson ratio ν_1 , and aspect ratio $\alpha = a/b$, the Eshelby tensor S is given by (Eshelby (1957)):

$$\begin{aligned}
S_{2222} = S_{3333} &= \frac{3}{8(1-\nu_1)} \frac{\alpha^2}{\alpha^2-1} + \frac{1}{4(1-\nu_1)} \left[1 - 2\nu_1 - \frac{9}{4(\alpha^2-1)} \right] q, \\
S_{1111} &= \frac{1}{2(1-\nu_1)} \left\{ 1 - 2\nu_1 + \frac{3\alpha^2-1}{\alpha^2-1} - \left[1 - 2\nu_1 + \frac{3\alpha^2}{\alpha^2-1} \right] q \right\}, \\
S_{3322} = S_{2233} &= \frac{1}{4(1-\nu_1)} \left\{ \frac{\alpha^2}{2(\alpha^2-1)} - \left[1 - 2\nu_1 + \frac{3}{4(\alpha^2-1)} \right] q \right\}, \\
S_{3311} = S_{2211} &= \frac{1}{2(1-\nu_1)} \left\{ \frac{-\alpha^2}{\alpha^2-1} + \frac{1}{2} \left[\frac{3\alpha^2}{\alpha^2-1} - (1-2\nu_1) \right] q \right\}, \\
S_{1133} = S_{1122} &= \frac{1}{2(1-\nu_1)} \left\{ 2\nu_1 - 1 - \frac{1}{\alpha^2-1} + \left[1 - 2\nu_1 + \frac{3}{2(\alpha^2-1)} \right] q \right\}, \\
S_{2323} &= \frac{1}{4(1-\nu_1)} \left\{ \frac{\alpha^2}{2(\alpha^2-1)} + \left[1 - 2\nu_1 - \frac{3}{4(\alpha^2-1)} \right] q \right\}, \\
S_{1212} = S_{1313} &= \frac{1}{4(1-\nu_1)} \left\{ 1 - 2\nu_1 - \frac{\alpha^2+1}{\alpha^2-1} - \frac{1}{2} \left[1 - 2\nu_1 - \frac{3(\alpha^2+1)}{(\alpha^2-1)} \right] q \right\}.
\end{aligned} \tag{3.23}$$

$$q = \begin{cases} \frac{\alpha}{(\alpha^2-1)^{3/2}} [\alpha(\alpha^2-1)^{1/2} - \cosh^{-1} \alpha], & \alpha \geq 1, \\ \frac{\alpha}{(1-\alpha^2)^{3/2}} [\cos^{-1} \alpha - \alpha(\alpha^2-1)^{1/2}], & \alpha \leq 1. \end{cases} \tag{3.24}$$

Since S is not symmetric (except for a sphere in an isotropic matrix), S can be expressed following the classical notation (Hill (1964), Walpole (1969)):

$$S = (S_{2222} + S_{2233}, S_{1122}, S_{2211}, S_{1111}, 2S_{2323}, 2S_{1212}), \tag{3.25}$$

specialized to a spheroid.

3.2.3 Tensor computations

We follow the notation in Hill (1964) for transverse isotropic tensors:

$$C_2 = (2k_T, l, l, n, 2G_T, 2G_L). \quad (3.26)$$

With this notation, the tensor operations yield (cf. Qiu and Weng (1990)):

$$\begin{aligned} C &= (c, g, h, d, e, f), \quad C' = (c', g', h', d', e', f'), \\ CM &= I, \quad I = (1, 0, 0, 1, 1, 1), \\ M &= (d/(cd - 2gh), -g/(cd - 2gh), -h/(cd - 2gh), c/(cd - 2gh), 1/e, 1/f), \\ CC' &= (cc' + 2hg', gc' + dg', hd' + ch', dd' + 2gh', ee', ff'), \end{aligned} \quad (3.27)$$

where again M is the compliance tensor.

For an isotropic stiffness tensor (which will be specified for the matrix, where we attach the subscript 1), following the same notation and operations, we have

$$\begin{aligned} C_1 &= (2k_1, l_1, l_1, n_1, 2G_1, 2G_1) = (2(K + 1/3G), K - 2/3G, K - 2/3G, K + 4/3G, 2G, 2G), \\ M_1 &= \left(\frac{1 - \nu_1}{E_1}, -\frac{\nu_1}{E_1}, -\frac{\nu_1}{E_1}, \frac{1}{E_1}, \frac{1}{2G}, \frac{1}{2G} \right). \end{aligned} \quad (3.28)$$

We now provide the result of computation of T and N from equation (3.21):

$$\begin{aligned}
P=S : C_1^{-1} &= \left(\frac{1}{E_1} [(1-\nu_1)(S_{2222} + S_{2233}) - 2\nu_1 S_{2211}], \frac{1}{E_1} [(1-\nu_1)S_{1122} - \nu_1 S_{1111}], \right. \\
&\quad \left. \frac{1}{E_1} (S_{2211} - \nu_1(S_{2222} + S_{2233})), \frac{1}{E_1} (S_{1111} - 2\nu_1 S_{1122}), \frac{1}{G_1} S_{2323}, \frac{1}{G_1} S_{1212} \right), \\
[I+P : (C_2 - C_1)] &= (c', g', h', d', e', f'), \\
c' &= 1 + \frac{2(k_2 - k_1)}{E_1} [(1-\nu_1)(S_{2222} + S_{2233}) - 2\nu_1 S_{2211}] + \frac{2(l_2 - l_1)}{E_1} [S_{2211} - \nu_1(S_{2222} + S_{2233})], \\
d' &= 1 + \frac{n_2 - n_1}{E_1} [S_{1111} - 2\nu_1 S_{1122}] + \frac{2(l_2 - l_1)}{E_1} [(1-\nu_1)S_{1122} - \nu_1 S_{1111}], \\
e' &= 1 + \frac{2(G_T - G_1)}{G_1} S_{2323}, \\
f' &= 1 + \frac{2(G_L - G_1)}{G_1} S_{1212}, \\
g' &= \frac{2(k_2 - k_1)}{E_1} [(1-\nu_1)S_{1122} - \nu_1 S_{1111}] + \frac{l_2 - l_1}{E_1} [S_{1111} - 2\nu_1 S_{1122}], \\
h' &= \frac{n_2 - n_1}{E_1} [S_{2211} - \nu_1(S_{2222} + S_{2233})] + \frac{l_2 - l_1}{E_1} [(1-\nu_1)(S_{2222} + S_{2233}) - 2\nu_1 S_{2211}].
\end{aligned} \tag{3.29}$$

$$T = [I + P : (C_2 - C_1)]^{-1} = (d'/p', -g'/p', -h'/p', c'/p', 1/e', 1/f'), \quad p' = c'd' - 2g'h',$$

$$N = (C_2 - C_1) : T = (c, g, h, d, e, f),$$

$$c = 2(k_2 - k_1)d'/p' - 2(l_2 - l_1)h'/p',$$

$$g = (l_2 - l_1)d'/p' - (n_2 - n_1)g'/p',$$

$$h = (l_2 - l_1)c'/p' - 2h'(k_2 - k_1)/p',$$

$$d = (n_2 - n_1)c'/p' - 2h'(l_2 - l_1)/p',$$

$$e = 2(G_T - G_1)/e',$$

$$f = 2(G_L - G_1)/f'.$$

(3.30)

To complete the Mori-Tanaka formula, what remains is the orientational average of T and N , equation (3.22).

3.2.4 Orientational averages

To compute orientational averages of the 4th order tensors enclosed with angle brackets in equation (3.22), we need to transform local coordinates (x, y, z) to global coordinates (x', y', z') . This change of coordinates is give by

$$\bar{N}_{ijkl} = \omega_{ip}\omega_{jq}\omega_{kr}\omega_{ls}N_{pqrs}, \quad (3.31)$$

where the components of ω_{ij} are the direction cosines for the transformation of Euler angles:

$$\omega(\phi, \gamma, \psi) = \begin{pmatrix} \cos \phi & \sin \phi & 0 \\ -\sin \phi & \cos \phi & 0 \\ 0 & 0 & 1 \end{pmatrix} \begin{pmatrix} \cos \theta & 0 & \sin \theta \\ 0 & 1 & 0 \\ -\sin \theta & 0 & \cos \theta \end{pmatrix} \begin{pmatrix} \cos \psi & \sin \psi \\ -\sin \psi & \cos \psi & 0 \\ 0 & 0 & 1 \end{pmatrix} \quad (3.32)$$

Using the above coordinate transformation, the averaging operation $\langle N \rangle$ becomes:

$$\langle N \rangle = \frac{\int_0^\pi \int_0^{\pi/2} \int_0^\pi \bar{N}(\phi, \theta, \psi) f(\phi, \theta, \psi) \sin \theta d\phi d\theta d\psi}{\int_0^\pi \int_0^{\pi/2} \int_0^\pi f(\phi, \theta, \psi) \sin \theta d\phi d\theta d\psi}. \quad (3.33)$$

However, the above integral is difficult to compute, so we proceed as follows. If N is a rank 4 transversely isotropic tensor, it has the 6-vector representation described earlier, $N = (c, g, h, d, e, f)$. Alternatively, N can be represented as a linear combination of the 6 dimensional basis of transversely isotropic tensors, with \mathbf{m} a unit vector corresponding to the axis of symmetry of N ,

$$\begin{aligned} N_{ijkl}(\mathbf{m}) = & b_1 \mathbf{m}_i \mathbf{m}_j \mathbf{m}_k \mathbf{m}_l + b_2 (\delta_{ik} \mathbf{m}_j \mathbf{m}_l + \delta_{il} \mathbf{m}_j \mathbf{m}_k + \delta_{jk} \mathbf{m}_i \mathbf{m}_l + \delta_{jl} \mathbf{m}_i \mathbf{m}_k) \\ & + b_3 \delta_{ij} \mathbf{m}_k \mathbf{m}_l + b_4 \delta_{kl} \mathbf{m}_i \mathbf{m}_j + b_5 \delta_{ij} \delta_{kl} + b_6 (\delta_{ik} \delta_{jl} + \delta_{il} \delta_{jk}), \end{aligned} \quad (3.34)$$

and the relationship between these 2 “coordinates” of N is

$$\begin{aligned} b_1 &= d + (c + e)/2 - g - h - 2f, & b_2 &= (f - e)/2, \\ b_3 &= h - (c - e)/2, & b_4 &= g - (c - e)/2, \\ b_5 &= (c - e)/2, & b_6 &= e/2. \end{aligned} \quad (3.35)$$

(Note: The developments above assume (3.10), which force $b_3 = b_4$, and therefore has 5 independent elements of transversely isotropic N .)

We denote the second moment \mathbf{M}_2 and fourth moment \mathbf{M}_4 of the PDF f by:

$$\mathbf{M}_2 = \langle \mathbf{m}_i \mathbf{m}_j \rangle, \quad \mathbf{M}_4 = \langle \mathbf{m}_i \mathbf{m}_j \mathbf{m}_k \mathbf{m}_l \rangle. \quad (3.36)$$

The orientational average of a transversely isotropic tensor N is therefore given by:

$$\begin{aligned} \langle N \rangle = & b_1 \mathbf{M}_4 + b_2 (\delta_{ik} M_{jl} + \delta_{il} M_{jk} + \delta_{jk} M_{il} + \delta_{jl} M_{ik}) + \\ & b_3 \delta_{ij} M_{kl} + b_4 \delta_{kl} M_{ij} + b_5 \delta_{ij} \delta_{kl} + b_6 (\delta_{ik} \delta_{jl} + \delta_{il} \delta_{jk}), \end{aligned} \quad (3.37)$$

where M_{ij} denotes the corresponding components of \mathbf{M}_2 . We note that kinetic theory of nematic polymer provides the PDF f of the inclusions, from which fourth and second moments are given by the first several terms in a spherical harmonic expansion. Traditional Landau-deGennes or second moment tensor models only provide \mathbf{M}_2 , and some additional *ad hoc* rule has to be invoked to get the fourth moment \mathbf{M}_4 .

3.2.5 A hierarchy of symmetries of the effective elasticity tensor of nano-spheroid composites

The orientational distributions of nano-elements often possess certain symmetries. Armed with the above developments, we now show how particle symmetries and mean-field PDF symmetries can be combined to prove symmetries of the effective elasticity and compliance tensors of the nano-composites. These symmetry results then provide a rigorous determination of the number of independent elasticity constants.

Recall that C_1 is an isotropic tensor and C_2 is a transversely isotropic tensor.

1. **Random distribution limit.** In the dilute limit, the PDF f is isotropic at rest, which implies

$$\mathbf{M}_2 = \frac{1}{3} \delta_{ij}, \quad \mathbf{M}_4 = \frac{1}{15} (\delta_{ij} \delta_{kl} + \delta_{ik} \delta_{jl} + \delta_{il} \delta_{jk}). \quad (3.38)$$

From equation(3.37), we get $\langle N \rangle$ explicitly for random orientational distributions:

$$\langle N \rangle_{ijkl} = \left(b_5 + \frac{1}{15}b_1 + \frac{1}{3}(b_3 + b_4) \right) \delta_{ij}\delta_{kl} + \left(b_6 + \frac{1}{15}b_1 + \frac{2}{3}b_2 \right) (\delta_{ik}\delta_{jl} + \delta_{il}\delta_{jk}). \quad (3.39)$$

which is, of course, isotropic. The same argument shows that $\langle T \rangle$, equation (3.21) is also isotropic. Further, the inversion, summation, and contraction preserve isotropy. Thus, the composite elasticity tensor C^e , equation (3.22), is isotropic.

2. Perfect alignment limit. Although not physically realizable, the extreme limit of perfect particle alignment across the entire ensemble is often considered. Mathematically, this limit allows exact analysis, and it is widely believed to represent some form of extreme bound, with the random alignment limit at the other extreme. (We will investigate these limits in examples to follow; they sometimes bound properties, yet not always.) Suppose all particles have the identical direction $\mathbf{m} = (\mathbf{m}_1, \mathbf{m}_2, \mathbf{m}_3)$, so the PDF f is a delta distribution:

$$f(\mathbf{m}) = \delta(\mathbf{m}). \quad (3.40)$$

Using equation (3.33), $\langle N \rangle_{ijkl} = N_{ijkl}(\mathbf{m})$. From (3.20), the effective stiffness tensor C^e has the form (3.34), which by construction is transversely isotropic, with principal axis \mathbf{m} .

3. Biaxial PDFs. Under simple shear or other rotational flows, the PDFs are generically biaxial, i.e., the second moment \mathbf{M}_2 has 5 independent components. Since C^e inherits the symmetries of \mathbf{M}_4 and \mathbf{M}_2 , we proceed to properties of \mathbf{M}_4 .

Generally, without any known symmetries, the fourth moment \mathbf{M}_4 of the orientational distribution is symmetric under all permutations of subscripts, i.e., $M_{ijkl} = M_{jikl} = M_{klij} = M_{lijk} = M_{kijl}$. These conditions reduce the number of independent components of \mathbf{M}_4 from 81 to 15. Furthermore, there are additional relations between \mathbf{M}_4 and \mathbf{M}_2 , e.g.,

$$\sum_k M_{ijkk} = M_{ij}, \quad \sum_i M_{ii} = 1. \quad (3.41)$$

These relations imply that *if* one knows \mathbf{M}_2 , then 6 components of \mathbf{M}_4 can be constructed. Thus, the number of independent elements of \mathbf{M}_4 , given \mathbf{M}_2 , is 9, which coincide with the space

of orthotropic rank 4 tensors; however this is indeed a coincidence, in that \mathbf{M}_4 is *not necessarily orthotropic*. Any orthotropic rank 4 tensor has the form of (3.12) in some orthogonal frame; if \mathbf{M}_4 is orthotropic, the basis that yields the form (3.12) comes from \mathbf{M}_2 .

Faraoni *et al.* (1999) showed numerically that \mathbf{M}_4 does not obey orthotropic symmetry. For f which obey in-plane symmetry with respect to the shear flow plane, clearly, \mathbf{M}_4 is symmetric with respect to the flow plane. Therefore, \mathbf{M}_4 has monoclinic symmetry. All simulations below confirm this property. For out-of-plane monodomain attractors, e.g. kayaking limit cycles, out-of-plane steady states, and chaotic orbits, \mathbf{M}_4 has no a “piori” special symmetry.

4. Uniaxial PDFs. Uniaxial orientational distributions occur at rest above a critical volume fraction, the so-called nematic phase (de Gennes and Prost (1993), Doi and Edwards (1986)), or in response to uniaxial extensional flow (Forest *et al.* (2000), Forest *et al.* (2004 c), Forest *et al.* (1999)) and applied magnetic fields (Forest *et al.* (2006)), at all volume fractions.

For nematic phases at equilibrium, there is a distinguished principal axis \mathbf{n}_1 of \mathbf{M}_2 , with corresponding eigenvalue d_1 , and isotropy transverse to \mathbf{n}_1 , i.e., the remaining two eigenvalues of \mathbf{M}_2 are equal, $d_2 = d_3$, indicating isotropy in the plane transverse to \mathbf{n}_1 . The fourth moment \mathbf{M}_4 is transversely isotropic, by numerical computation, and the effective stiffness tensor C^e is also transversely isotropic, and the symmetry axes of \mathbf{M}_4 , C , \mathbf{M}_2 are orthogonal and the same.

3.3 Mechanical property predictions of rod nano-composites

In this section, the moduli of NPNCs, as predicted using the Mori-Tanaka theory just described, are presented in terms of volume fraction and shear rate. These processing conditions, together with particle aspect ratio, parametrize the Doi-Hess kinetic equation for the nano-particle PDF f . We consider typical model NPNCs with aspect ratio $r = 100$. So that our predictions have contact with realistic materials, elastic constants of individual transversely-isotropic nano-particles (PmPV) and isotropic matrix LaRC-SI, are provided in Table 1, adopted from Odegard *et al.* (2003). The longitudinal and transverse Young’s moduli of the nano-fibers are 120 and 3.2 times that of the matrix, respectively; the longitudinal and transverse shear moduli are 20 and 3.2 times that of the matrix. The orientational distribution

functions are obtained from numerical simulations of the Smoluchowski equation of Doi-Hess (Doi (1981), Hess (1976), Forest *et al.* (2004a), Forest *et al.* (2004b)). The fundamental objects of interest are:

1. NPNC enhancements in moduli relative to the nano-particle/matrix contrasts;
2. nonlinear (superlinear) gains which might be exploited in design strategies; and
3. anisotropy characterization.

Table 3.1: Properties of matrix and nano-rod inclusion (GPa)

inclusion		matrix	
k_2	9.9	k_1	6.79
l_2	8.4	l_1	5.43
n_2	457.6	n_1	8.14
G_T	4.4	G_1	1.36
G_L	27.0	G_1	1.36
E_L	450.4	E_1	3.80
E^T	12.1	E_1	3.80
ν_2	0.42	ν_1	0.4

3.3.1 Effective properties vs. volume fraction for quiescent mesophases

First, the relative enhancement of effective moduli (and the number of distinct moduli) are presented as a function of inclusion volume fraction for quiescent phases. Recall the equilibrium phase diagram of nematic polymers exhibits a first-order phase transition and hysteresis in the PDF versus volume fraction (cf. Doi and Edwards (1986)); this feature is described in terms of the Flory order parameter, $s = d_1 - d_2$, computed from the second moment $\mathbf{M}_2(f)$, Figure 3.1.a. All symmetries of C^e follow from those of $\mathbf{M}_2(f)$, $\mathbf{M}_4(f)$, and corresponding independent moduli are computed from our numerical databases of f , \mathbf{M}_2 , \mathbf{M}_4 , according to the above developments and presented in Figure 3.1.b, c, d.

We define the relative enhancement of Young's moduli as

$$\mathcal{E}_E = \frac{E^e - E_1}{E_1}, \quad (3.42)$$

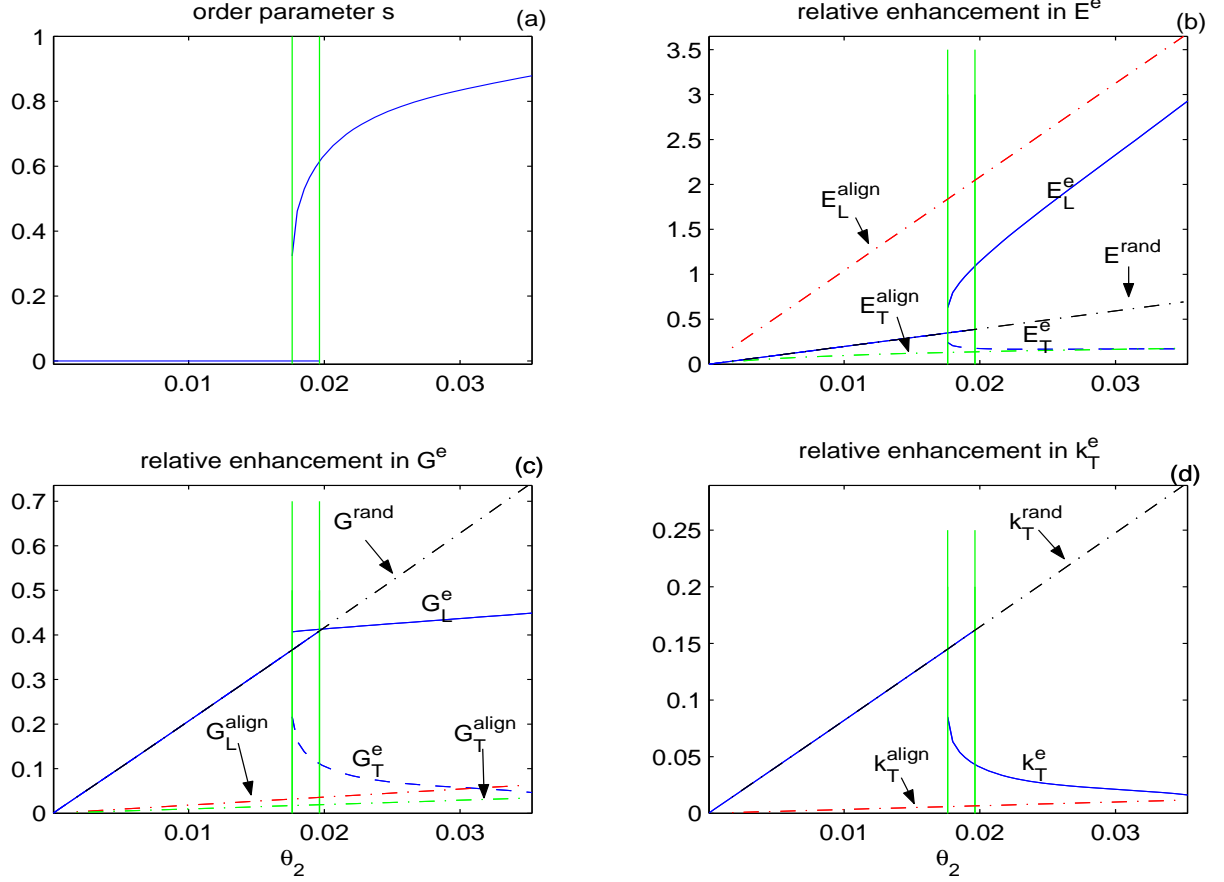


Figure 3.1: a. Order parameter s vs. volume fraction θ_2 ; b. corresponding relative enhancement of Young's moduli E^e ; c. corresponding relative enhancement of shear moduli G^e ; d. Corresponding relative enhancement of transverse bulk moduli k_T^e . The solid lines are the relative longitudinal moduli, the dashed lines are the relative transverse moduli.

where E^e and E_1 are the effective (composite) and matrix Young's modulus, respectively. For other moduli, the relative enhancements are defined similarly.

At sufficiently low volume fractions, $\theta_2 < 1.96\%$ for this specific rod-solvent dispersion, the equilibrium phase is isotropic, $f(\mathbf{m}) = \frac{1}{4\pi}$, $\mathbf{M} = \mathbf{I}/3$, and $s = 0$. For $\theta_2 > 1.76\%$, a stable, ordered (nematic) equilibrium forms due to excluded volume potential interactions; the PDF is *uniaxial*, with second moment orientation tensor $\mathbf{Q} = \mathbf{M}_2 - \frac{1}{3}\mathbf{I}$ of the form $s(\mathbf{nn} - \mathbf{I}/3)$, where \mathbf{n} is the uniaxial director, and the Flory order parameter s measures the degree of anisotropy.

From the symmetries derived earlier, C^e is isotropic for isotropic PDFs, and transversely isotropic for uniaxial PDFs, thus possessing 2 and 5 distinct moduli, respectively. These are simply labeled E^e and G^e in the isotropic phase, while in the nematic phase, the labels are E_L^e

along the principal axis; E_T^e transverse to the principal axis; G_L^e on the planes containing the principal axis, G_T^e on the plane transverse to the principal axis, and k_T which is obtained by applying a uniform strain to the symmetry axis, with no uniaxial extension along the principal axis. Extremal bounds due to perfect and random alignment are shown.

Fig. 3.1 conveys that for quiescent phases, *moduli inherit the hysteresis and bi-stability of the PDF*. There are discontinuous jumps in moduli at the critical volume fractions $\theta_2^* = 1.76\%$, where the nematic phase begins, and $\theta_2^{**} = 1.96\%$, where the isotropic phase becomes unstable.

YOUNG'S MODULI. Fig. 3.1.b.

Isotropic phases. E^e increases linearly with volume fraction θ_2 , since $f \equiv 1/(4\pi)$ for all θ_2 . The line is extended for $\theta_2 > 1.96\%$ to show the contrast with distinct moduli $E_{L,T}^e$ of the nematic phase.

Nematic phases.

- The *longitudinal modulus* E_L^e , with respect to the principal coincide axis of f , \mathbf{M}_4 , \mathbf{M}_2 and C^e , experiences nonlinear growth as a result of focusing of the rod ensemble along the principal axis (Figure 3.1.a).

1. The perfect alignment limit, $s = 1$, yields an *upper bound*, E_L^{align} , shown ranging between 180% to 360% for $1.76\% < \theta_2 < 3.5\%$. By comparison, the composite E_L^e ranges from 62% to 290% over the same range of volume fractions.
2. In the bi-stable range, the nematic phase has 1.8 times greater E_L at θ_2^* , increasing to 2.8 times greater E_L^e at θ_2^{**} , again a reflection of nonlinear gain.

- The *transverse Young's modulus* E_T^e , applies to any direction in the plane normal to the principal symmetry axis \mathbf{n}_1 , and has the following properties:

1. E_T^e lies between the random configuration and above the perfect alignment limit, by symmetry arguments, owing to the number of rods on average available to resist compression or tension in that plane.
2. E_T^e decreases with increased θ_2 , since the PDF becomes more focused, converging onto the lower bound of E_T^e set by the perfect alignment limit.

- The Young's moduli together indicate strong anisotropy, with average values

$$E_L^e \approx 3.4E_T^e, \quad E_T^e \approx 1.1E_m. \quad (3.43)$$

SHEAR MODULI. Fig.3.1.c. (We use the following notation for effective longitudinal and transverse shear moduli: $G_L^e = G_{12}^e = G_{13}^e$, $G_T^e = G_{23}^e$.)

Isotropic phases. $G^e = G_L^e = G_T^e$, which increase linearly with volume fraction θ_2 .

Nematic phases.

- *The longitudinal shear modulus G_L^e .*

1. G_L^e begins at θ_2^* at 40.7%, yet grows very slowly to 44.9% at $\theta_2 = 3.5\%$.
2. $G_L^e < G_L^{rand}$ since there are more rods in the shearing plane for the random configuration.
3. $G_L^{align} \ll G_L^e$ since the rods on average lie in the plane transverse to the symmetry axis.

- As the PDF focuses, less rods are aligned in transverse planes, thus the *transverse shear modulus* G_T^e decreases rather quickly toward G_T^{align} .

TRANSVERSE BULK MODULUS. Fig. 3.1.d.

Isotropic phases. k_T^e increases with volume fraction θ_2 .

Nematic phases. $k_T^{rand} \gg k_T^e > k_T^{align}$.

3.3.2 Effective moduli of sheared nano-rod composites

Next, we explore the effect of shear-induced orientational distributions on effective moduli, which breaks isotropic and uniaxial symmetry of the PDF at rest. By arguments given earlier, in general, C^e is monoclinic symmetric for in-plane PDF f , so there are 13 independent components. We choose the same NPNC properties of Table 3.1.

First, we fix the inclusions at an *isotropic* volume fraction 1%, and retain the rod aspect ratio at 100. The orientational distributions f are obtained from kinetic theory simulations for a range of shear rates, which yield \mathbf{M}_2 , \mathbf{M}_4 and thereby C^e . All sheared PDFs are steady states.

The principal values of the second moment \mathbf{M}_2 vs. normalized shear rate (Peclet number Pe) are shown in Fig.3.2.a; recall $d_1 - d_2$ measures anisotropy, while $d_2 - d_3$ measures biaxiality

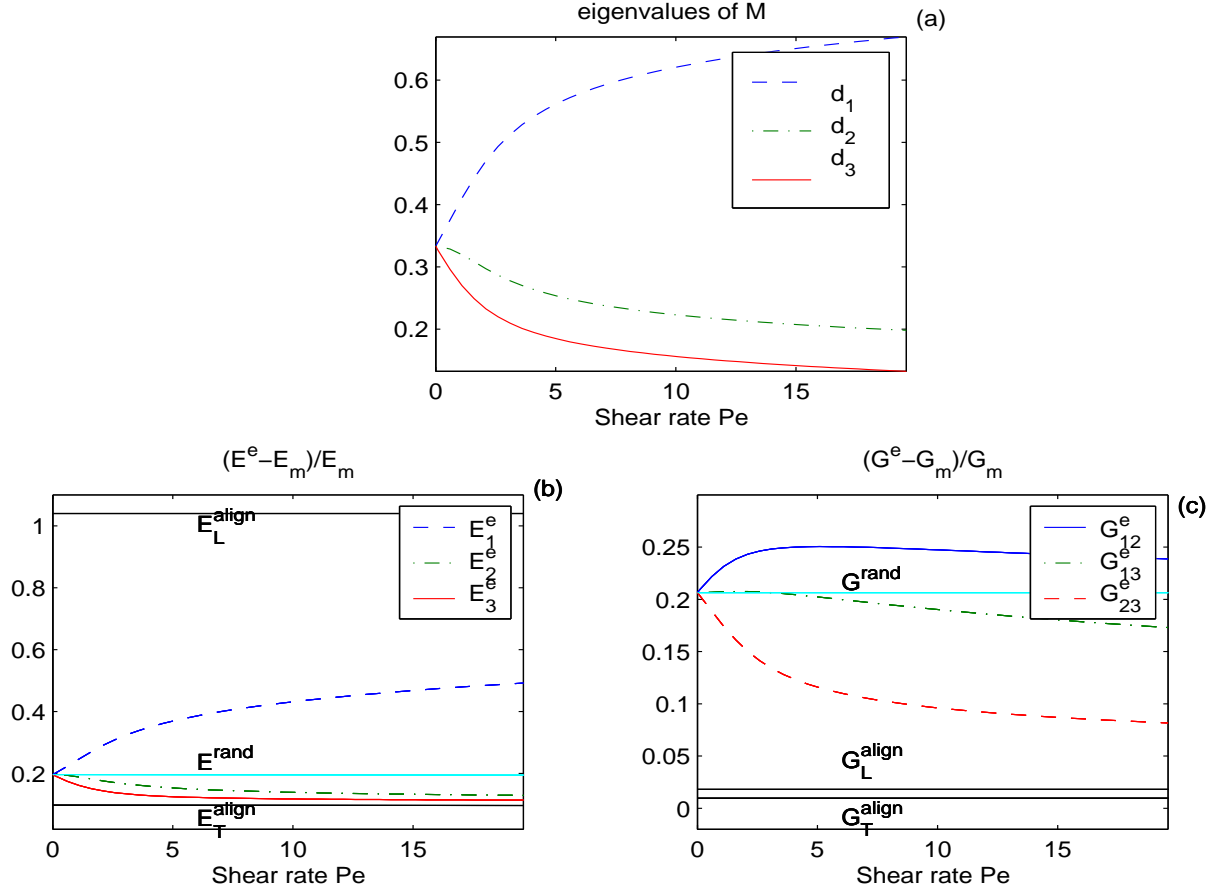


Figure 3.2: Sheared PDFs and effective moduli for 1% volume fraction nano-rods of aspect ratio 100, with particle-matrix properties of Table 3.1 (Odegard *et al.* (2003)). a. Eigenvalues ($d_1 > d_2 > d_3$) of M_2 vs. normalized shear rate (Peclet number Pe); b. corresponding relative enhancement of Young's moduli; c. corresponding relative enhancement of shear moduli.

or anisotropy in the plane transverse to the principal axis. We emphasize that $d_1 = d_2 = d_3 = 1/3$ at $Pe = 0$, so all anisotropy arises due to shear flow.

• **Young's moduli.** Fig. 3.2.b. The enhancements in the distinct Young's moduli E_i^e ($i = 1, 2, 3$) are shown with respect to the 3 orthogonal axes of \mathbf{M}_2 .

1. The largest modulus, E_1^e , associated with the principal axis \mathbf{n}_1 (\mathbf{M}_2), exhibits nonlinear gain from the shear-induced order, departing from E^{rand} at $Pe = 0$ and slowly approaching the upper bound given by E_L^{align} .
2. The transverse Young's moduli E_2^e and E_3^e fall from E^{rand} for $Pe > 0$, and converge to the lower bound provided by E_T^{align} .

• **Shear moduli.** Fig. 3.2.c.

1. $G_{12}^e > G_{13}^e > G_{23}^e$.
2. $G_{12}^e > G^{rand} \gg G_{L,T}^{align}$.
3. $G^{rand} > G_{13}^e > G_{23}^e \gg G_{L,T}^{align}$.
4. All shear moduli enhancement are between 10% and 25%, so the gain over the matrix is not dramatic.

Second, we shift to a concentrated dispersions, $\theta_2 = 2.3\%$ (corresponding to $N = 6$). For this volume fraction, shear once again induces steady PDFs (Forest *et al.* (2004a), Forest *et al.* (2004b)), called *logrolling states* (Larson and Ottinger (1991)), where the peak axis of f is along the vorticity-axis, orthogonal to the shear plane. These PDFs have symmetry with respect to the shear plane, therefore yield monoclinic C^e . (We omit intermediate θ_2 for this work, since shear induces limit cycles, rather than steady states.)

Fig. 3.3 shows the enhancements of moduli for these logrolling PDFs. Fig. 3.3.a shows $d_1 \gg d_2 \approx d_3$, so the PDF is *weakly biaxial*, and the Young's moduli effect nearly uniaxial properties: $E_1^e \gg E_2^e \approx E_3^e$, Fig. 3.3.b. The shear moduli obey $G_{12}^e > G_{13}^e \gg G_{23}^e$, with strong contrasts at higher Pe , Fig. 3.3.c.

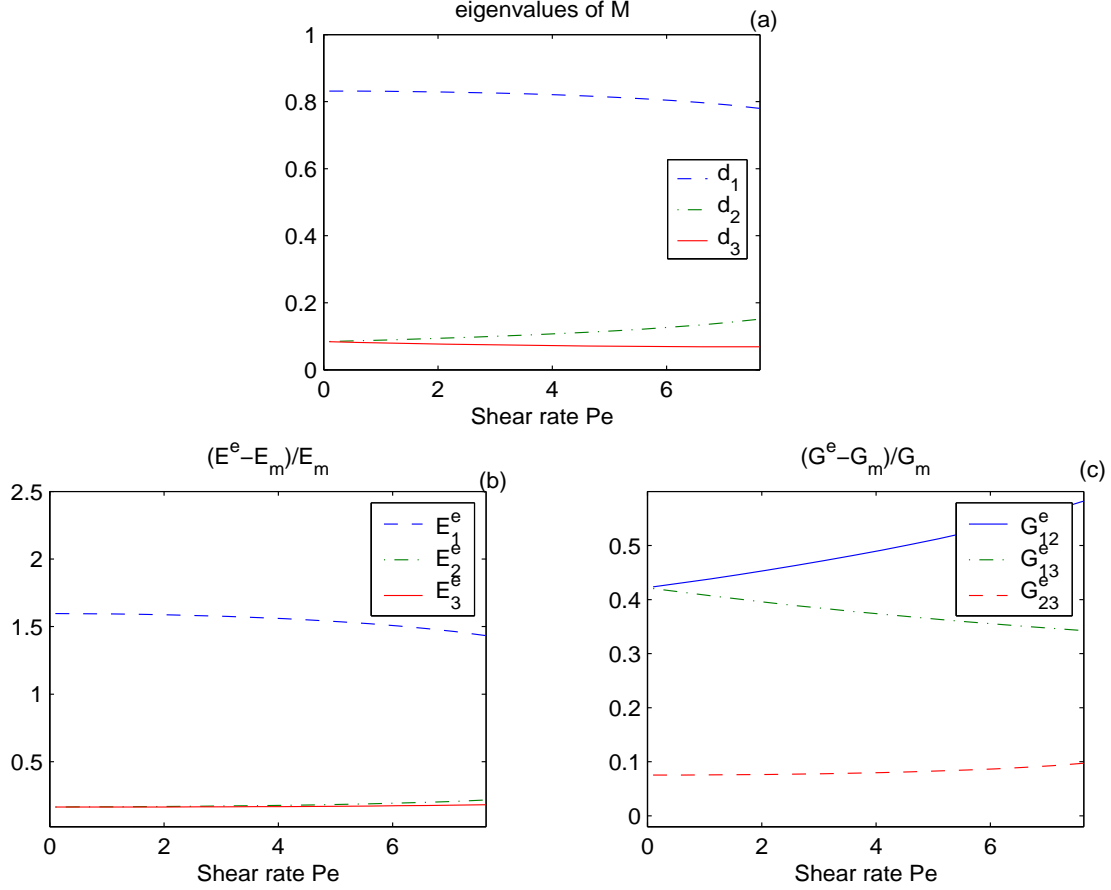


Figure 3.3: Sheared PDFs and effective moduli for 2.3% volume fraction nano-rods of aspect ratio 100, arising from vorticity-aligned (logrolling) steady states. a. eigenvalues ($d_1 > d_2 > d_3$) of \mathbf{M}_2 vs. normalized shear rate (Peclet number Pe); b. relative enhancement of Young's moduli; c. relative enhancement of shear moduli.

3.4 Conclusions

In this chapter, the micro-mechanics based Mori-Tanaka method is used to predict the effective elastic properties of NPNCs. Symmetries of the effective elasticity tensor are derived from those of the PDF: C^e is isotropic if the PDF is random; transversely isotropic if the PDF is uniaxial; monoclinic for in-plane PDFs; and maximally anisotropic if the PDF is fully biaxial (typical of sheared ensembles). C^e is thereby determined to have 2, 5, 9 or 15 independent moduli for isotropic, uniaxial, in-plane, and biaxial PDFs, respectively.

For fixed aspect ratio, we study the volume fraction dependence of the effective moduli for quiescent equilibrium distributions. The key feature is that moduli inherit not only symmetry

from the PDF, but bistability and hysteresis of the classical Onsager isotropic-nematic phase diagram. The trends of the various moduli are calculated versus volume fraction, exhibiting nonlinear gains of principal compressible (Young) moduli and corresponding drops in transverse shear moduli. Bounds are given in terms of limiting configurations of random and perfect alignment. Finally, the effects of shear rate on isotropic (low volume fraction) and nematic (high volume fraction) composites are detailed.

Chapter 4

Future Work

4.1 Percolation-dominated properties

We have developed a predictive theory for effective conductivity of nematic polymers composed with a matrix, based on volume averaging at low volume fractions. Nematic polymer nano-particles are high aspect ratio spheroids, either rods or platelets. A generically anisotropic effective conductivity tensor σ^e is explicitly derived as a function of volume fraction θ_2 of nematic polymers for both quiescent and sheared molecular ensembles. The principle values $\{\sigma_j^e\}_{j=1}^3$ of σ^e give scalar conductivities along the respective principal axes of σ^e , which clearly predict enhancements of $\sigma_{max}^e \equiv \max\{\sigma_j^e\}$ due to increases in θ_2 and due to extension or shear deformation of the quiescent molecular orientational distribution. On the other hand, experimental data indicates an even more pronounced effect on conductivity and mechanical properties due to percolation, i.e., connected paths of nano-inclusions, which extend across boundaries of a bulk sample.

Whereas the literature has a variety of treatments and predictions of percolation in rod dispersions, there is no effective procedure that we are aware of that is based explicitly on the orientational probability distribution function (PDF) of the nano-particle ensemble.

The goal of this work is to compute percolation thresholds and more detailed cluster statistics consistent with PDFs generated from the Smoluchowski equation of Doi-Hess theory for quiescent or flowing nematic polymers. The key physics of Doi-Hess theory is rotational diffusion coupled with an excluded-volume potential, with or without an extra hydrodynamic coupling. These results can then be linked with the numerical framework of others, such as Ounaies *et al.* (2003) and Lusti *et al.* (2002), to yield effective properties such as conductivity

or elasticity tensors due to volume averaging *and* percolation.

4.2 Elastic wave propagation through nano-composites

I have started to look at mechanical wave propagation in elastic (viscoelastic) nano-rod/platelet materials, which are often used in situations involving dynamic application of loads. There are no results which predict strain or stress localization in these composites, nor how macroscopic loads are distributed by these “soft composite”. A state of stress may be generated that leads to failure. It is necessary to understand the response characteristics of the material body to account properly for all important effects.

If a wave length of the characteristic response of the material is very long compare with the scale of the inhomogeneity, then the material is governed by the effective properties of the equivalent homogeneous medium. In this case the methods of structure response and wave propagation are identical to those of homogeneous materials.

Given the various forms of C by homogenization theory or percolation theory, with different symmetries, what would we predict will be key features of the propagation of waves.

BIBLIOGRAPHY

- S. G. Advani, C. L. Tucker, The use of tensors to describe and predict fiber orientation in short fiber composites, *J. Rheol.*, **31**, 751-784 (1987).
- R. Bandyopadhyay, G. Basappa, A. K. Sood, Observation of chaotic dynamics in dilute sheared aqueous solutions of CTAT, *Phys. Rev. Lett.*, **84**(9), 2022-2025 (2000).
- Y. Benveniste, A new approach to the application of Mori-Tanaka's theory in composite materials, *Mechanics of Materials*, **6**, 147-157 (1987).
- A. N. Beris, B. J. Edwards, **Thermodynamics of Flowing Systems with Internal Microstructure**, Oxford Science Publications, (1994).
- W. R. Burghardt, Molecular orientation and rheology in sheared lyotropic liquid crystalline polymers, *Macromol. Chem. Phys.*, **199**, 471-488 (1998).
- B. Chakrabarti, M. Das, C. Dasgupta, S. Ramaswamy, and A. K. Sood, Spatiotemporal rheochaos in nematic hydrodynamics, *Phys. Rev. Lett.*, **92**, 055501 (2004).
- C. V. Chaubal, L. G. Leal, A closure approximation for liquid-crystalline polymer models based on parametric density estimation, *J. Rheol.*, **42**(1), 177-201 (1998).
- T. S. Chow, Elastic moduli of filled polymers: the effect of particle shapes, *J. Appl. Phys.*, **48**, 4072-4075 (1977).
- D. H. Chung, T. H. Kwon, Invariant-based optimal fitting closure approximation for the numerical prediction of flow-induced fiber orientation, *J. Rheol.*, **46**(1), 169-194 (2001).
- J. S. Cintra Jr., C. L. Tucker, Orthotropic closure approximations for flow-induced fiber orientation, *J. Rheol.*, **39**(6), 1095-1121 (1995).
- P. Constantin, I. Kevrekidis, E. S. Titi, Asymptotic states of a Smoluchowski equation, Preprint in University of Chicago, (2004).
- P. G. de Gennes, J. Prost, **The Physics of Liquid Crystals**, Oxford University Press, (1993).
- E. J. Doedel, A. R. Champneys, T. F. Fairgrieve, Y. A. Kuznetsov, B. Sandstede, X. Wang, **AUTO97: Continuation and Bifurcation Software for Ordinary Differential Equations**, Concordia University, (1997).
- M. Doi, Rotational relaxation time of rigid rodlike macromolecules in concentrated solution, *J. Phys. (Paris)*, **36**, 607-611 (1975).
- M. Doi, Molecular dynamics and rheological properties of concentrated solutions of rodlike polymers in isotropic and liquid crystalline phases, *J. Polym. Sci., Polym. Phys. Ed.*, **19**, 229-243 (1981).
- M. Doi, S. F. Edwards, Dynamics of concentrated polymer systems III: the constitutive equation, *J Chem. Soc. Faraday Trans. II*, **74**, 1818-1832 (1978).

- M. Doi, S. F. Edwards, **The Theory of Polymer Dynamics**, Oxford University Press, (1986).
- J. D. Eshelby, The determination of the elastic field of an ellipsoidal inclusion, and related problem, Proc. of Royal Society of London, Series A, Mathematical and Physical Sciences, **241**, 376-396 (1957).
- V. Faraoni, M. Grosso, S. Crescitelli, P. L. Maffettone, The rigid-rod model for nematic polymers: an analysis of the shear flow problem, J. Rheol., **43**, 829-843 (1999).
- R. Florian, Z. Neda, Improved percolation thresholds for rods in three-dimensional boxes, technical report, cond-mat/0110067 (2001).
- R. Florian, Z. Neda, Comment on percolation thresholds in the three-dimensional stick system, technical report, cond-mat/9804326 (1998).
- M. G. Forest, H. Zhou, Q. Wang, Model study of the spinning of thermotropic liquid crystalline polymers: fiber performance predictions and bounds on throughput, Advances in Polymer Technology, **18**(4), 314-335 (1999).
- M. G. Forest, Q. Wang, H. Zhou, Homogeneous pattern selection and director instabilities of nematic liquid crystal polymers induced by elongational flows, Phys. of fluids, **12**(3), 490-498 (2000).
- M. G. Forest, Q. Wang, R. Zhou, Symmetries of the Doi kinetic theory for nematic polymers of arbitrary aspect ratio: at rest and in linear flows, Phys. Rev. E, **66**(3), 031712 (2002).
- M. G. Forest, Q. Wang, Monodomain response of finite-aspect-ratio macromolecules in shear and related linear flows, Rheol. Acta, **42**, 20-46 (2003).
- M. G. Forest, R. Zhou, Q. Wang, Full-tensor alignment criteria for sheared nematic polymers, J. Rheol., **47**(1), 105-127 (2003).
- M. G. Forest, R. Zhou, Q. Wang, Scaling behavior of kinetic orientational distributions for dilute nematic polymers in weak shear, J. Non-Newt. Fluid Mech., **116**(2-3), 183-204 (2004).
- M. G. Forest, Q. Wang, R. Zhou, The weak shear kinetic phase diagram for nematic polymers, Rheol. Acta, **43**(1), 17-37 (2004a).
- M. G. Forest, Q. Wang, R. Zhou, The flow-phase diagram of Doi theory for sheared nematic polymers, II: finite shear rates, Rheol. Acta, **44**(1), 80-93 (2004b).
- M. G. Forest, Q. Wang, R. Zhou, E. Choate, Monodomain response of arbitrary aspect ratio nematic polymers in general linear planar flows, J. Non-Newt. Fluid Mech., **118**(1), 17-31 (2004c).
- M. G. Forest, R. Zhou, Q. Wang, Chaotic boundaries of nematic polymers in mixed shear and extensional flows, Phys. Rev. Lett., **93**(8), 088301 (2004d).
- M. G. Forest, Q. Wang, H. Zhou, R. Zhou, Structure scaling properties of confined nematic polymers in plane Couette cells: the weak flow limit, J. Rheol., **48**(1), 175-192 (2004e).

- M. G. Forest, X. Zheng, R. Zhou, Q. Wang, R. Lipton, Anisotropy and dynamic ranges in effective properties of sheared nematic polymer nano-composites, *Adv. Funct. Mater.*, **15**(12), 2029-2035 (2005).
- M. G. Forest, R. Zhou, Q. Wang, Kinetic structure simulations of nematic polymers in plane Couette cells, II: in-plane structure transitions, *SIAM Multiscale Modeling and Simulations*, **4**(4), 1280-1304 (2005a).
- M. G. Forest, R. Zhou, Q. Wang, Spatial coherence, rheological chaotic dynamics, and hydrodynamic feedback of nematic polymers in confined shear, submitted to *J. Non-Newt. Fluid Mech.*, (2005b).
- M. G. Forest, R. Zhou, Q. Wang, X. Zheng, R. Lipton, Anisotropy and heterogeneity of nematic polymer nano-composite film properties, NSF Institute for Mathematics and its Applications, Minneapolis, MN, Proceeding of Workshop on Modeling of soft matter, **141**, 85-98 (2005c).
- M. G. Forest, Q. Wang, R. Zhou, Extending the magnetic/electric field-hydrodynamic analogy of homogeneous rod & platelet liquid crystals and suspensions to strongly coupled fields,, *J. Rheol.*, submitted, (2006).
- G. G. Fuller, **Optical Rheometry of Complex Fluids**, Oxford University Press, (1995).
- D. Grecov, A. D. Rey, Transient rheology of discotic mesophases, *Rheol. Acta*, **42**, 590-604 (2003).
- M. Grosso, R. Keunings, S. Crescitelli, P. L. Maffettone, Prediction of chaotic dynamics in sheared liquid crystalline polymers, *Phys. Rev. Lett.*, **86**(14), 3184-3187 (2001).
- M. Grosso, S. Crescitelli, E. Somma, J. Vermant, P. Moldenaers, P. L. Maffettone, Prediction and observation of sustained oscillations in a sheared liquid crystalline polymer, *Phys. Rev. Lett.*, **90**, 098304 (2003).
- A. Gusev, H. R. Lusti, P. J. Hine, Stiffness and thermal expansion of short fiber composites with fully aligned fibers, *Advanced Engineering Materials*, **4**(12), 927-931 (2002).
- J. C. Halpin and J. L. Kardos, The Halpin-Tsai equations: a review, *Polym. Eng. Sci.*, **16**, 344-352 (1976).
- S. Hess, Fokker-Planck-equation approach to flow alignment in liquid crystals, *Z. Naturforsch Teil*, **31A**(9), 1034-1037 (1976).
- S. Hess, Construction and test of thermostats and twirlers for molecule rotations, *Z. Naturforsch*, **58a**, 377-391 (2003).
- S. Hess, M. Kroger, Regular and chaotic orientational and rheological behaviour of liquid crystals, *J. Phys.: Condens. Matter*, **16**, s3835-s3859 (2004).
- R. Hill, Theory of mechanical properties of fiber-strengthened materials: I. elastic behavior, *J. Mech. Phys. Solids*, **12**, 199-212 (1964).
- E. J. Hinch, L. G. Leal, The effect of Brownian motion on the rheological properties of a suspension of non-spherical particles, *J. Fluid Mech.*, **52**, 683-712 (1972).

- D. A. Jack, D. E. Smith, Assessing the use of tensor closure methods with orientational distribution reconstruction functions, *J. Comp. Mater.*, **38**(21), 1851-1871 (2004).
- S. B. Kharchenko, J. F. Douglas, J. Obrzut, E. A. Grulke, and K. B. Migler, Flow-induced properties of nanotube-filled polymer materials, *Nature Materials*, **3**, 564-568 (2004).
- S. Kirkpatrick, Percolation and conduction, *Review of Modern Physics*, **45**(4), 574-588 (1973).
- J. G. Kirkwood, P. L. Auer, The visco-elastic properties of solutions of rod-like macromolecules, *J. Chem. Phys.*, **19**, 281-283 (1951).
- M. Kroger, Simple models for complex nonequilibrium fluids, *Phys. Rep.*, **390**, 453-551 (2004).
- R. G. Larson, Arrested tumbling in shearing flows of liquid crystal polymers, *Macromolecules*, **23**, 3983-3992 (1990).
- R. G. Larson, H. Ottinger, The effect of molecular elasticity on out-of-plane orientations in shearing flows of liquid crystalline polymers, *Macromolecules*, **24**, 6270-6282 (1991).
- R. G. Larson, **The Structure and Rheology of Complex Fluids**, Oxford University Press, (1999).
- N. Laws and R. McLaughlin, The effect of fiber length on the overall moduli of composite materials, *J. Mech. Phys. Solids*, **27**, 1-13 (1979).
- R. Lipton, On the behavior of elastic composites with transverse isotropic symmetry, *J. Mech. Phys. Solids*, **39**, 663-681 (1991).
- R. H. Lusti, P. J. Hine, A. A. Gusev, Direct numerical predictions for the elastic and thermoelastic properties of short fiber composites, *Composites Science and Technology*, **62**, 1927-1934 (2002).
- P. L. Maffettone, M. Grosso, M. C. Friedenberg, G. G. Fuller, Extensional flow of a two dimensional polymer liquid crystal, *Macromolecules*, **29**, 8473-8478 (1996).
- G. Marrucci, P. L. Maffettone, Description for the liquid crystalline phase of rodlike polymers at high shear rates, *Macromolecules*, **22**, 4076-4082 (1989).
- T. Maruyama, G. G. Fuller, M. Grosso, P. L. Maffettone, The dynamics of two dimensional polymer nematics, *J. Non-Newt. Fluid Mech.*, **76**, 233-247 (1998).
- G. W. Milton, **The Theory of Composites**, Cambridge University Press, (2002).
- G. M. Odegard, T. S. Gates, K. E. Wise, C. Park, E. J. Siochi, Constitutive modeling of nanotube-reinforced polymer composites, *Composites Science and Technology*, **63**, 1671-1687 (2003).
- Z. Ounaies, C. Park, K. E. Wise, E. J. Siochi, J. S. Harrison, Electrical properties of single wall carbon nanotube reinforced polyimide composites, *Composites Science and Technology*, **63**, 1637-1646 (2003).
- Y. P. Qiu, G. J. Weng, On the application of Mori-Tanaka's theory involving transversely isotropic spheroidal inclusions, *Int. J. Engng sci.*, **28**, 1121-1137 (1990).

- A. D. Rey, T. Tsuji, Recent advances in theoretical liquid crystal rheology, *Macromol. Theory Simul.*, **7**, 623-639 (1998).
- A. D. Rey, M. M. Denn, Dynamical phenomena in liquid-crystalline materials, *Annual Rev. Fluid Mech.*, **34**, 233-266 (2002).
- G. R. Rienacker, S. Hess, Orientational dynamics of nematic liquid crystals under shear flow, *Physica A*, **267**, 294-321 (1999).
- G. Rienacker, M. Kroger, S. Hess, Chaotic orientational behavior of a nematic liquid crystal subjected to a steady shear flow, *Phys. Rev. E*, **66**, 040702 (2002).
- H. See, M. Doi, R. G. Larson, The effect of steady flow fields on the isotropic-nematic phase transition of rigid rod-like polymers, *J. Chem. Phys.*, **92**(1), 792-800 (1990).
- G. Sgalari, G. L. Leal, J. J. Feng, The shear flow behavior of LCPs based on a generalized Doi model with distortional elasticity, *J. Non-Newt. Fluid Mech.*, **102**, 361-382 (2002).
- VK. S. Shante and S. Kirkpatrick, An introduction to percolation theory, *Advances in Physics*, **20**, 325-357 (1971).
- D. Stauffer, A. Aharony, **Introduction to Percolation Theory**, Taylor and Francis Ltd, (1994).
- J. A. Stratton, **Electromagnetic Theory**, McGraw-Hill Company, (1941).
- Z. J. Tan, G. C. Berry, Studies on the texture of nematic solutions of rodlike polymers. 3. Rheo-optical and rheological behavior in shear, *J. Rheol.*, **47**, 73-104 (2003).
- P. S. Theocaris, D. P. Sokolis, Spectral decomposition of the compliance fourth-rank tensor for orthotropic materials, *Archive of Applied Mechanics*, **70**, 289-306 (2000).
- S. Torquato, **Random Heterogeneous Materials**, Springer, (2002).
- R. A. Vaia, **Polymer Nanocomposites**, Oxford University Press, (2002).
- B. L. Van Horn, H. H. Winter, Dynamics of shear aligning of nematic liquid crystal monodomains, *Rheol. Acta*, **39**, 294-300 (2000).
- B. L. Van Horn, D. M. Boudreau, H. H. Winter, Shear response of monodomains of nematic liquid crystals: TIF model comparisons and effect of pre-tilt, *Rheol. Acta*, **42**(6), 585-589 (2003).
- L. J. Walpole, On the overall elastic moduli of composite materials, *J. Mech. Phys. Solids*, **17**, 235-251 (1969).
- T. T. Wu, The effect of inclusion shape on the elastic moduli of a two-phase material, *Int. J. Solids Structures*, **2**, 1-8 (1966).
- C. D. Wu and R. L. McCullough, **Constitutive Relationships for Heterogeneous Materials**, Applied Science Publishers, (1977).
- L. Yao, X. Zheng, M. G. Forest, Q. Wang, R. Zhou, A model for defect dynamics in sheared nematic polymers, University of North Carolina Program in Applied Mathematics Preprint, (2006).

- X. Zheng, M. G. Forest, R. Zhou, Q. Wang, Likelihood & expected-time statistics of monodomain attractors in sheared discotic and rod-like nematic polymers, *Rheol. Acta*, **44**(3), 219-234 (2005).
- X. Zheng, M. G. Forest, R. Lipton, R. Zhou, Q. Wang, Exact scaling laws for electrical conductivity properties of nematic polymer nano-composite monodomain, *Adv. Funct. Mater.*, **15**(4), 627-638 (2005).
- H. Zhou, M. G. Forest, X. Zheng, Q. Wang, R. Lipton, Extension-enhanced conductivity of liquid crystalline polymer nano-composites, *Macromolecular Symposia*, **288**(1), 81-90 (2005).
- R. Zhou, M. G. Forest, Q. Wang, Kinetic structure simulations of nematic polymers in plane Couette cells, I: the algorithm and benchmarks, *SIAM Multiscale Modeling and Simulations*, **3**(4), 853-870 (2005).